

INFORMATION TO USERS

This manuscript has been reproduced from the microfilm master. UMI films the text directly from the original or copy submitted. Thus, some thesis and dissertation copies are in typewriter face, while others may be from any type of computer printer.

The quality of this reproduction is dependent upon the quality of the copy submitted. Broken or indistinct print, colored or poor quality illustrations and photographs, print bleedthrough, substandard margins, and improper alignment can adversely affect reproduction.

In the unlikely event that the author did not send UMI a complete manuscript and there are missing pages, these will be noted. Also, if unauthorized copyright material had to be removed, a note will indicate the deletion.

Oversize materials (e.g., maps, drawings, charts) are reproduced by sectioning the original, beginning at the upper left-hand corner and continuing from left to right in equal sections with small overlaps.

**ProQuest Information and Learning
300 North Zeeb Road, Ann Arbor, MI 48106-1346 USA
800-521-0600**

UMI[®]

SQUID-Detected NMR and MRI in Microtesla Magnetic Fields

by

Robert Francis McDermott

B.A. (Harvard University) 1993

M.A. (University of California, Berkeley) 1998

A dissertation submitted in partial satisfaction of the

requirements for the degree of

Doctor of Philosophy

in

Physics

in the

GRADUATE DIVISION

of the

UNIVERSITY OF CALIFORNIA, BERKELEY

Committee in charge:

Professor John Clarke, Chair

Professor Erwin L. Hahn

Professor Alexander Pines

Fall 2002

UMI Number: 3082316



UMI Microform 3082316

Copyright 2003 by ProQuest Information and Learning Company.

All rights reserved. This microform edition is protected against
unauthorized copying under Title 17, United States Code.

ProQuest Information and Learning Company
300 North Zeeb Road
P.O. Box 1346
Ann Arbor, MI 48106-1346

SQUID-Detected NMR and MRI in Microtesla Magnetic Fields

Copyright 2002

by

Robert Francis McDermott

Abstract

SQUID-Detected NMR and MRI in Microtesla Magnetic Fields

by

Robert Francis McDermott

Doctor of Philosophy in Physics

University of California, Berkeley

Professor John Clarke, Chair

A low transition temperature dc Superconducting QUantum Interference Device (low- T_c dc SQUID) was used to perform liquid-state nuclear magnetic resonance (NMR) and magnetic resonance imaging (MRI) experiments in magnetic fields from microtesla to tens of microtesla, corresponding to proton Larmor frequencies from tens of Hz to kHz. The spins were polarized in a magnetic field of the order of millitesla. Upon turnoff of the polarizing field, precession was induced in the much weaker measurement field. Because the SQUID magnetometer was operated with an untuned, superconducting, input circuit, the integrated intensity of the NMR lines was independent of the strength of the measurement field. On the other hand, the NMR linewidth scaled linearly with the measurement field strength. Narrowing of the NMR signal bandwidth through reduction of the strength of the measurement field led to an enhancement of both spectral resolution and signal-to-noise ratio (SNR).

A novel cryogenic insert was constructed to allow SQUID measurement of NMR signals from room temperature samples with high filling factor. From samples with volume of a few milliliters and thermal polarization of order 10^{-8} , SNR of a few tens were

achieved in a single shot. Heteronuclear scalar couplings were resolved in ^1H - ^{31}P and ^1H - ^{13}C systems. Furthermore, the frequency-independent sensitivity of the untuned SQUID magnetometer allowed simultaneous detection of NMR signals from nuclei with different magnetogyric ratios.

A system based on a low- T_c SQUID gradiometer was used to acquire MRIs from distilled water and mineral oil phantoms in microtesla fields. The bandwidth-narrowing technique was exploited to enhance spatial resolution for a fixed strength of the encoding gradients. With magnetic field gradients of the order of tens of microtesla per meter, images with spatial resolution of a millimeter were achieved.

The techniques described in this thesis could readily be adapted for use with multichannel SQUID systems designed for biomagnetic measurements at low frequency, and represent a first step toward the development of low cost, portable NMR and MRI scanners based on untuned SQUID magnetometers.

Table of Contents

Table of Contents	iii
Acknowledgements	vii
Chapter 1 Introduction	1
Chapter 2 The dc SQUID	4
2.A SQUID basics	5
2.B Practical SQUID Design	7
2.C SQUID Readout	9
2.D Flux Transformers and Gradiometers	12
2.E Tuned vs. Untuned Magnetometers	16
Chapter 3 Nuclear Magnetic Resonance	23
3.A NMR Basics	24
3.B Relaxation in NMR	28
3.C Inhomogeneous Broadening	33
3.D Spin Echoes	33
3.E Interactions in Liquid-State NMR	36
3.E.1 Chemical Shift	36
3.E.2 J-coupling	37
3.F Non-resonant Spin Manipulation	40

Chapter 4	Magnetic Resonance Imaging	43
4.A	Introduction	43
4.B	Projection Reconstruction	44
4.C	Fourier Imaging	46
4.D	T_1 Contrast Imaging	50
4.E	Practical High Field MRI	52
Chapter 5	Liquid-State NMR and Scalar Couplings in Microtesla Magnetic Fields	56
5.A	Introduction	56
5.B	Experimental Apparatus	58
5.B.1	Cryogenic Insert	58
5.B.2	SQUID Gradiometer and Readout	60
5.B.3	Static Field and Excitation Coils	62
5.C	Conventional Pulsed NMR	64
5.D	Concept of Microtesla Field NMR	66
5.E	Microtesla Field NMR: Experimental	68
5.F	Multinuclear Studies	74
5.G	Scalar Couplings	75
Chapter 6	SQUID-Detected MRI in Microtesla Fields	80
6.A	Introduction	80
6.B	Concept of Microtesla Field MRI	83

6.C	Experimental Apparatus: Magnetic Field and Gradient Coils	88
6.D	Experimental Apparatus: SQUID Sensors	95
6.E	SQUID NMR in Unshielded Environment	98
6.E.1	Effect of Static Magnetic Fields Gradients and Zeeman Field Drift on Evolution of Nuclear Spins	98
6.E.1.a	Static Magnetic Field Gradients	98
6.E.1.b	Zeeman Field Drift	99
6.E.2	SQUID System in Unshielded Environment	101
6.E.2.a	60 Hz Fields and Harmonics	101
6.E.2.b	Radiofrequency Suppression of V_Φ	102
6.E.2.c	Broadband Noise from the Environment	107
6.F	Choice of Measurement Field	109
6.F.1	Inhomogeneous Line Broadening and Dependence on Measurement Field Strength	109
6.F.2	Environmental Interference	110
6.F.3	Image Distortion Due to Concomitant Gradients	112
6.G	NMR Experiments	113
6.H	MRI Experiments	116
6.I	Magnetic Field Noise of the System	119
6.I.1	Distant Sources of Environmental Noise and Interference	122
6.I.2	Local Sources of Magnetic Field Noise: Thermal Noise of the Cryostat	128

6.J	Ongoing Work	132
Chapter 7	Conclusion	136

Acknowledgements

First, I am deeply grateful to Professor John Clarke for his encouragement and guidance over the past six years. It has been a great privilege and a pleasure to work in his group. I am indebted to Professor Alexander Pines, our collaborator in the Department of Chemistry, for his enthusiasm and continued support of SQUID-detected NMR and MRI.

I was very fortunate to overlap for several years in the Clarke group with Dr. Michael Mück. Much of what I learned about SQUID electronics and practical SQUID systems I learned from him. None of the work described below would have been possible without the high-quality Nb-AlO_x-Nb SQUIDs which Michael provided.

My first exposure to SQUID NMR and MRI came from work on a high-T_c system under Dr. Klaus Schlenga and Dr. Ricardo de Souza. I thank these talented researchers for introducing me to the fundamentals of NMR spectroscopy and MRI.

The work on the low-T_c SQUID system for NMR spectroscopy of liquids, as well as the early work on the SQUID MRI system, was performed jointly with Dr. Andreas Trabesinger. I am grateful for his dedication and friendship.

From my very earliest efforts to measure NQR signals from ¹⁴N, I benefited greatly from numerous discussions with Professor Erwin Hahn. He is the force behind ongoing attempts to use a SQUID to detect the Barnett effect in nuclear spins.

The construction of The Cube – the centerpiece of the SQUID MRI system – would not have been possible without the architectural input and expert carpentry of Dr.

Darin Kinion. Thanks to his efforts, the City of Berkeley is one step closer to becoming a Magnetic Field-Free Zone.

In the fall of 2001, I was joined on the SQUID MRI project by SeungKyun Lee. I am grateful for his hard work and considerable experimental skill. This year has been both highly enjoyable and highly productive, even if it seemed at times that we were merely, in Seung's words, "adding craziness to existing craziness".

I am grateful to Nathan Kelso and Dr. Bennie ten Haken for recent contributions to the SQUID MRI project. Bennie has been instrumental in implementing many of the latest improvements to the system.

I acknowledge the encouragement and support of Dr. Jiri Vrba and Dr. Alistair Fife of CTF, Inc. Their loan of a low-noise superinsulated cryostat has speeded progress on the SQUID MRI system considerably.

I thank Dr. Hugh Seton of the University of Aberdeen for extensive detailed discussions regarding his innovative design for a low-noise fiberglass dewar.

The cryogenic insert described in Chapter 5 was made by Tom Lawhead of the glass shop in the Chemistry Department. This intricate piece of glasswork was essential to the liquid-state spectroscopy work.

I acknowledge numerous helpful discussions about analog electronics and flyfishing with John Davis and the staff of the Physics Department Electronics Shop. I am grateful to George Weber and Tom Pedersen and the highly skilled staff of the Physics Department Machine Shop. I thank Barbara Salisbury for her help throughout my graduate career.

I have truly enjoyed spending time both inside and outside the lab with many fellow Clarke group members, among whom I wish to mention especially Konstantin Kouznetzov, Achim Kittel, Byungdu Oh, Sherry Cho, Tim Shaw, Marc-Oliver André, Yann Chemla, Roy Therrien, Jo Chen, Jan Kycia, Yi Zhang, Juha Hassel, Tae-Kyu Lee, Dale van Harlingen, and Britton Plourde.

I gratefully acknowledge the funding provided by the Director, Office of Energy Research, Office of Basic Energy Sciences, Materials Sciences Division of the U.S. Department of Energy under Contract No. DE-AC03-76SF00098.

Finally, I thank my family and Megan for their love and support.

Chapter 1. Introduction

In the conventional NMR experiment, the magnetic field serves a dual purpose. First, in the high temperature limit, the polarization of the nuclear spins scales linearly with the strength of the magnetic field. In addition, the resonant frequency of the nuclei is directly proportional to the magnetic field strength. In the case of NMR detection with a Faraday coil, therefore, the precessing magnetization of the sample induces a voltage in the receiver which scales as B^2 . This quadratic dependence of the NMR signal strength on magnetic field continues to fuel the drive to higher fields (of the order of tesla to tens of tesla) in commercial NMR and MRI scanners.

At the same time, there is considerable interest in the development of NMR and MRI systems which operate at low magnetic field strength. In comparison to conventional NMR scanners based on superconducting magnets, low field systems based on simple electromagnets (or which make use of the magnetic field of the Earth, $B_{\text{Earth}} \sim 50 \mu\text{T}$) offer the advantages of drastically reduced cost and complexity, and increased mobility and openness. Moreover, in an MRI experiment, reduction in measurement field strength can eliminate artifacts due to magnetic susceptibility variations, and yield

improved spin-lattice relaxation time contrast. The overwhelming obstacle to the development of practical low field NMR spectrometers or MRI scanners is the intrinsically low sensitivity of the low field experiment.

An appealing alternative to conventional Faraday detection of the NMR signal in low field is detection of the NMR signal with a dc SQUID. When operated with an untuned, superconducting input circuit, the SQUID magnetometer is sensitive to magnetic flux, rather than the rate of change of magnetic flux. Therefore, in the case of SQUID detection, the NMR signal strength is independent of the measurement field for a fixed sample magnetization. Moreover, the sensitivity of the SQUID is unsurpassed at low frequencies: high quality low- T_c SQUID magnetometers are capable of resolving 1 fT (10^{-15} T) in a unit bandwidth.

In this thesis, I describe a series of NMR and MRI experiments involving detection with a low- T_c dc SQUID in magnetic fields from microtesla to tens of microtesla, corresponding to proton Larmor frequencies from tens of Hz to kHz. At these field strengths, it is possible to achieve NMR linewidths of the order of 1 Hz even in grossly inhomogeneous magnetic fields. Narrowing of the NMR signal bandwidth through reduction of the measurement field strength leads to an enhancement in both spectral resolution and (in the case of detection with an untuned SQUID magnetometer) signal-to-noise ratio (SNR). In the context of MRI, the bandwidth-narrowing technique yields an enhancement in spatial resolution for a fixed strength of the encoding gradients.

This thesis is organized as follows. In Chapter 2, I give a brief introduction to SQUIDs and SQUID systems. In Chapters 3 and 4, I give an overview of the basic principles of pulsed NMR spectroscopy and MRI, respectively. In Chapter 5, I describe a

low- T_c SQUID system for NMR spectroscopy of liquids, and demonstrate a SQUID NMR based “bond detector”, capable of accurately measuring heteronuclear scalar couplings in microtesla magnetic fields. Finally, in Chapter 6, I describe a system for SQUID-detected MRI in microtesla fields, present preliminary spectra and images obtained with this system, and report on progress toward a SQUID-based system for human-scale MRI.

The techniques of SQUID-detected NMR are very different from those of conventional high field NMR. While there are definite advantages to SQUID detection, there are many limitations, and many more technical issues which must be adequately addressed in order for the approach to have a chance of success. It is unlikely that SQUIDs will revolutionize the field of magnetic resonance. On the other hand, there are a number of interesting niche applications for SQUID-detected NMR which might be realized in the near future, especially in the area of low field MRI. I hope that this thesis will be of some use to the students and researchers who try to build on the work described here.

Chapter 2. The dc SQUID

The dc Superconducting QUantum Interference Device (SQUID) is an extremely sensitive magnetic flux-to-voltage transducer [1-2]. State-of-the-art devices operated at 4.2 K can resolve one millionth of a magnetic flux quantum, $\Phi_0 = h/2e \sim 2.07 \times 10^{-15} \text{ T m}^2$, in a 1 Hz bandwidth. Moreover, the intrinsic sensitivity of the SQUID is independent of frequency over an extremely broad range, extending from dc to tens of GHz. SQUID magnetometers designed for maximum sensitivity at low frequencies are used to measure the minute magnetic fields generated by electrical currents in the human brain [3]. In the radiofrequency range, an amplifier based on the dc SQUID has a noise temperature which is an order of magnitude lower than the best semiconductor amplifiers available, and has found application in the search for dark matter [4]. Finally, the high sensitivity and frequency-independent response of the SQUID have enabled a novel class of nuclear magnetic resonance (NMR) and magnetic resonance imaging (MRI) experiments in microtesla fields [5]; these are the subject of this thesis.

In this chapter I give a brief introduction to SQUIDs and SQUID systems. I begin with an overview of the principles of dc SQUID operation. I briefly discuss the design and fabrication of practical low- T_c devices. Next I describe the flux-locked loop, and introduce the concept of the flux transformer and the SQUID gradiometer. I finish the chapter with a short discussion of the relative merits of tuned and untuned input circuits for applications of the SQUID to magnetic resonance experiments.

A. *SQUID Basics*

The dc SQUID consists of a superconducting loop of inductance L interrupted at two points by resistively shunted Josephson junctions [6-9], each with critical current I_c , self-capacitance C , and shunt resistance R (Figure 2.1A) [2]. The I-V curve of the SQUID is shown in Figure 2.1B for two values of external flux applied to the SQUID loop. For $\Phi_{\text{ext}} = n\Phi_0$, bias current divides equally across the two arms of the SQUID, and a nonzero voltage appears across the device at a current equal to twice the critical current of the individual junctions. For finite values of flux bias, however, circulating currents are generated in the loop of the SQUID which cause the device to switch to the voltage state at a lower applied current. The critical current of the device is maximally suppressed at a flux bias of $(n + \frac{1}{2})\Phi_0$. When the SQUID is biased with a dc current slightly above $2I_c$, the voltage across the SQUID becomes a quasi-sinusoidal function of the flux Φ applied to the SQUID loop, with period equal to the flux quantum Φ_0 : the dc SQUID is a flux-to-voltage transducer (Figure 2.1C). When the device is biased with a static flux of $(n \pm \frac{1}{4})\Phi_0$, a small applied flux change $\Delta\Phi$ results in a change in voltage across the SQUID of

$$\Delta V = V_{\Phi} \Delta \Phi \sim \pi V_{p-p} \Delta \Phi, \quad (2.1)$$

where $V_{\Phi} \equiv dV/d\Phi$ is the slope of the transfer curve at the operating point, and V_{p-p} is the peak-to-peak voltage modulation of the device.

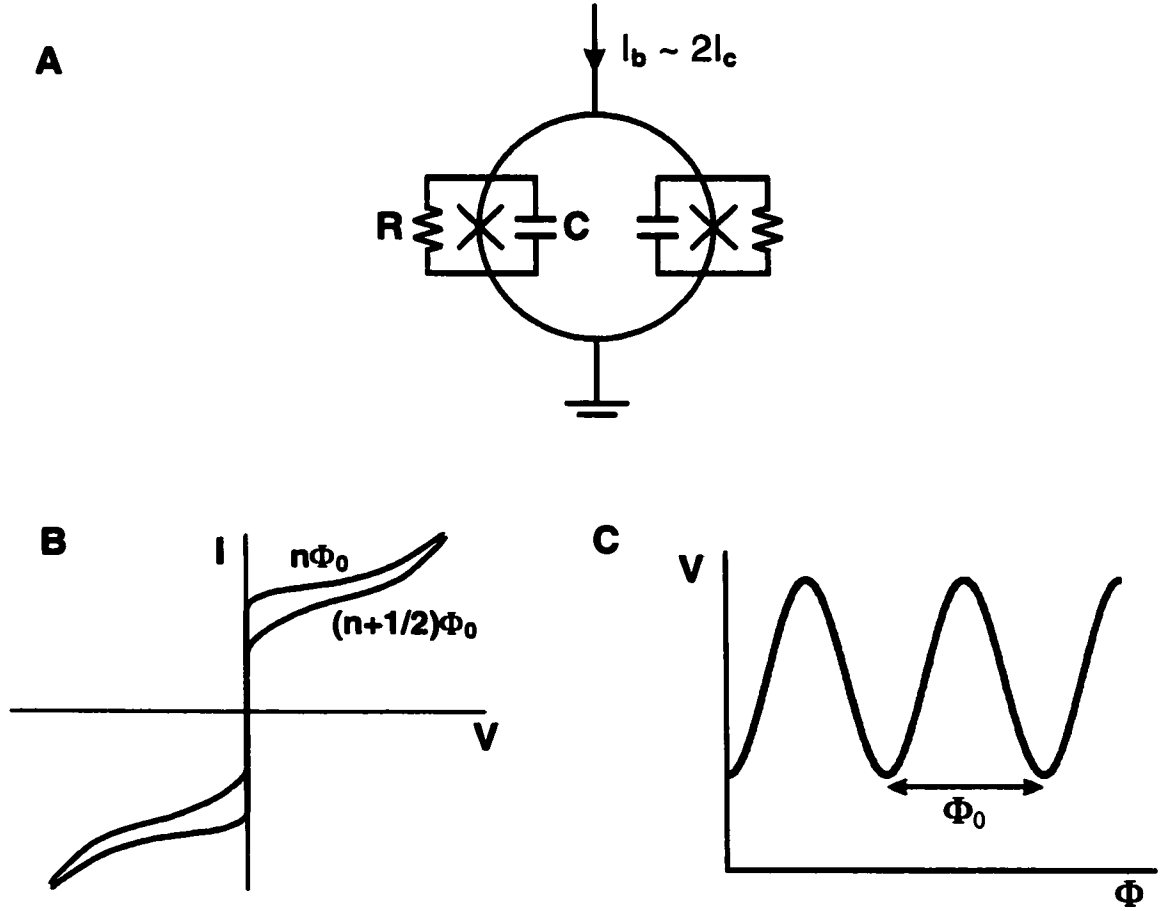


Figure 2.1. The dc SQUID. (A) Schematic of the dc SQUID. The superconducting loop with inductance L is interrupted at two points by Josephson junctions, each with critical current I_c , self-capacitance C , and shunt resistance R . (B) The I - V characteristic of the dc SQUID, shown for integer and half-integer values of flux bias. (C) V - Φ curve of the dc SQUID. The voltage across the SQUID oscillates as a function of the applied flux, with period Φ_0 .

The parameters of the SQUID are chosen with the following criteria in mind. To eliminate hysteresis in the current-voltage characteristics of the Josephson junctions, we require

$$\beta_c \equiv \frac{2\pi I_c R}{\Phi_0} RC = \omega_J RC \leq 1 \quad (2.2)$$

where ω_J is the Josephson frequency corresponding to the voltage $I_c R$ [7-8]. In addition, in order to observe any signal from the SQUID, we require that the magnetic energy $\Phi_0^2/2L$ per flux quantum greatly exceed the thermal energy $k_B T$. This condition can be expressed as

$$L \ll \frac{\Phi_0^2}{4\pi k_B T} \quad (2.3)$$

[10], which corresponds to a SQUID self-inductance $L \sim 5.9$ nH at $T = 4.2$ K.

Computer modeling has shown that the noise energy of the SQUID is minimized for a reduced inductance $\beta = 2LI_c/\Phi_0 \sim 1$ [11-13]. For $\beta = 1$ and for the noise parameter $\Gamma = 2\pi k_B T/I_c \Phi_0 = 0.05$, analysis shows that a device which is optimally current- and flux-biased will have a transfer function

$$V_\Phi \approx \frac{R}{L}, \quad (2.4)$$

and a spectral density of voltage noise

$$S_V(f) \approx 16k_B T R. \quad (2.5)$$

B. Practical SQUID Design

The vast majority of low- T_c dc SQUIDs are fabricated after a design introduced in the early 1980s by Ketchen and Jaycox [14-15]. Here the SQUID loop is formed by a

square washer patterned from a thin superconducting film deposited on an insulating substrate. The signal is coupled to the SQUID via a superconducting spiral input coil, which is deposited directly on top of the SQUID washer and separated from the washer by a thin insulating layer (Figure 2.2). In this design, the inductance of the SQUID washer is given by

$$L = 1.25\mu_0 d, \quad (2.6)$$

where d is the inner dimension of the square washer [15]. Neglecting stripline inductance, the inductance of the input coil is given by

$$L_i = n^2 L, \quad (2.7)$$

where n is the number of turns in the input coil. Flux is coupled from the input circuit to the SQUID with high efficiency:

$$M = \alpha \sqrt{LL_i} = \alpha n L, \quad (2.8)$$

where the coupling coefficient α is typically around 0.9.

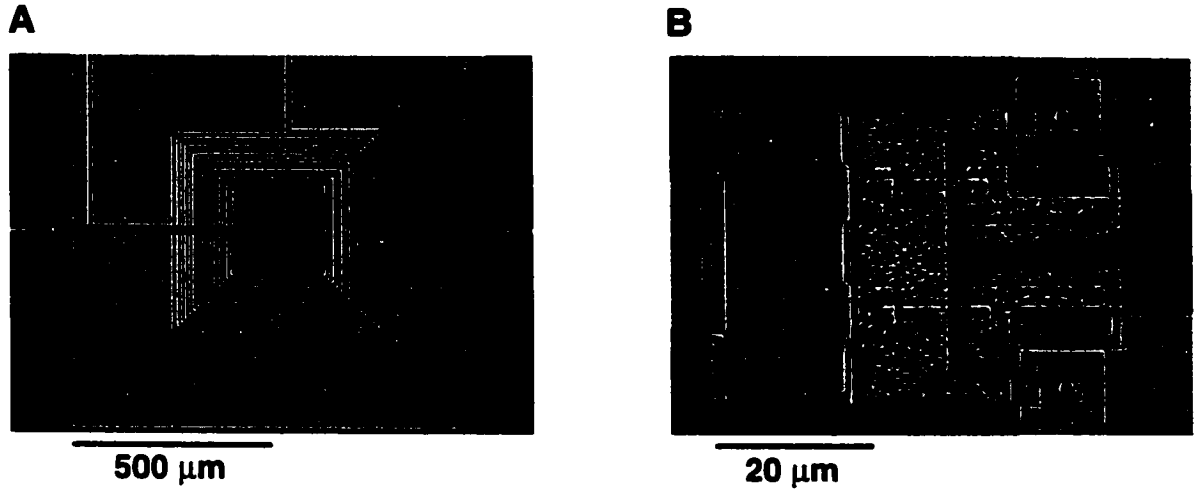


Figure 2.2. Photograph of a Nb-AlOx-Nb dc SQUID. (A) Expanded view, showing square washer and spiral input coil tightly coupled to the SQUID loop. The Josephson junctions are on the left side of the washer. (B) Closeup view of the Josephson junctions.

The SQUIDs used in the work described in this thesis were fabricated at the University of Giessen by Michael Mück using an all-liftoff Nb-AlO_x-Nb technology. The Nb and Al films and the Pd shunts were deposited by dc sputtering, and the SiO₂ insulating layer was formed by rf sputtering. All patterning was done photolithographically. For a 350 pH square-washer SQUID, typical parameters were $2I_c = 5 \mu\text{A}$, $R/2 = 10 \Omega$, and $V_{p-p} \approx 40 - 50 \mu\text{V}$.

C. SQUID Readout

To linearize its response to an applied flux, the SQUID is typically operated in a flux-locked loop (Figure 2.3) [16-17]. Here, the voltage across the SQUID is amplified, integrated, and then fed back to the SQUID as a flux applied by a feedback coil which is tightly coupled to the SQUID loop via the mutual inductance M_f . The voltage drop which appears across the feedback resistor R_f is then proportional to the externally applied flux. In this way the SQUID acts as a null detector of magnetic flux, capable of accurately tracking flux changes which are both much smaller than or much greater than a flux quantum.

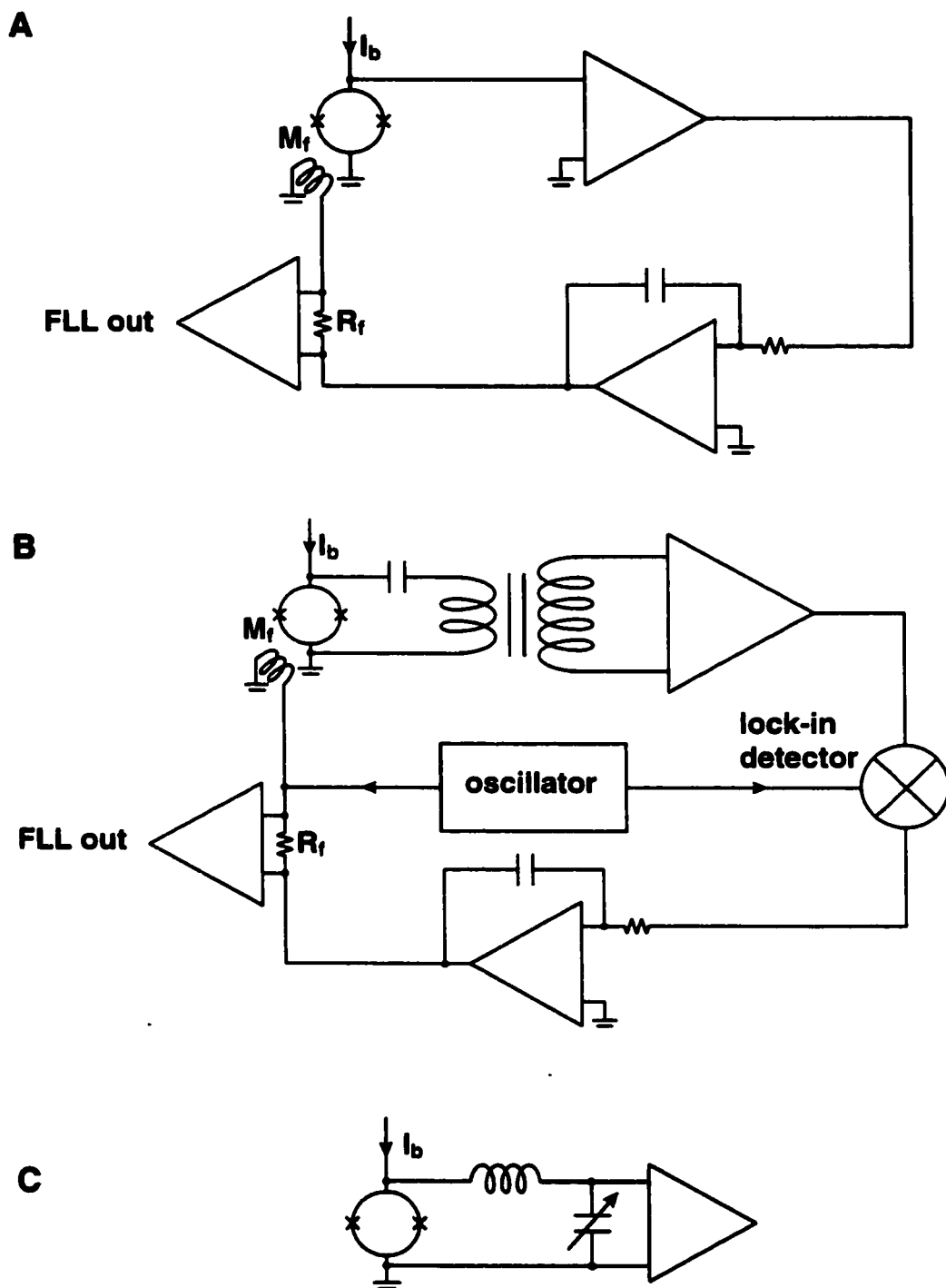


Figure 2.3. SQUID readout with a flux-locked loop. (A) Direct readout scheme. (B) SQUID readout scheme involving flux modulation. In this case the SQUID is coupled to the preamplifier either via a transformer, as shown in this panel, or (C) via a tank circuit which is tuned to the modulation frequency.

While the so-called direct readout scheme described above is conceptually simple and straightforward to implement, it is often the case that the noise of a SQUID read out in such a manner is dominated by the preamplifier, which is typically operated at room temperature. The noise of the preamplifier referred to the SQUID as a magnetic flux is as follows:

$$S_{\Phi}^{1/2}(\text{preamp}) = \frac{(e_v^2 + e_i^2 R_d^2)^{1/2}}{V_{\Phi}}, \quad (2.9)$$

where e_v and e_i are the input voltage and current noise of the preamplifier, respectively, and R_d is the dynamic impedance of the SQUID at its operating point. Typically, the contribution of preamplifier current noise can be neglected, due to the small dynamic impedance of the SQUID (of the order of tens of ohms). For a preamplifier input voltage noise of $1 \text{ nV/Hz}^{1/2}$ (above the $1/f$ knee), a transfer function of $1 \text{ mV}/\Phi_0$ is required to reduce the noise contribution of the preamplifier to $1 \mu\Phi_0/\text{Hz}^{1/2}$. Moreover, as the $1/f$ knee of most semiconductor preamplifiers extends out to tens or hundreds of Hz, the situation is considerably worse at low frequencies.

These difficulties are avoided by operating the SQUID in a flux-locked loop with flux modulation at a frequency from tens of kHz to MHz. In this scheme, the SQUID is biased with an ac flux with amplitude of approximately $\Phi_0/4$, and the signal from the SQUID is detected with a lock-in measurement at the modulation frequency. The SQUID signal is thus moved to a frequency which is far above the $1/f$ knee of the preamplifier; moreover, it is now possible to properly match the SQUID dynamic impedance to the noise impedance of the preamplifier by means of a step-up transformer [18] (which transforms R_d as the square of the turns ratio n of the transformer, to $n^2 R_d$; Figure 2.3B)

or by embedding the SQUID in a tank circuit [16] (in which case R_d is transformed as the square of the Q of the tank, to $Q^2 R_d$; Figure 2.3C). For example, for a SQUID with $R_d = 20 \Omega$ which is properly matched by a transformer with $n = 10$ to a preamplifier with $(e_v^2 + e_i^2 n^4 R_d^2)^{1/2} \sim 1 \text{ nV/Hz}^{1/2}$ at the modulation frequency, a transfer function of only $100 \mu\text{V}/\Phi_0$ is now required to reduce the preamplifier noise contribution to the level of $1 \mu\Phi_0/\text{Hz}^{1/2}$.

D. Flux Transformers and Gradiometers

To increase its sensitivity to magnetic fields, the SQUID is often operated with a superconducting flux transformer, consisting of a large-area pickup coil (with inductance L_p), which is tightly coupled to the signal source, and an input coil (with inductance L_i), which is tightly coupled to the SQUID loop (Figure 2.4A) [2]. The transformer operates on the principle of flux conservation in a superconducting loop: when a magnetic field B is applied to the pickup loop area A_p , a supercurrent flows in the transformer, coupling flux Φ_s to the SQUID via the mutual inductance $M = \alpha(L_i L)^{1/2}$ (we defer discussion of the case of a tuned flux transformer to Section 2.E). The effective area of the SQUID magnetometer is then

$$A_{\text{eff}} = \frac{\Phi_s}{B} = A_p \frac{M}{L_i + L_p} = A_p \frac{\alpha \sqrt{L_i L}}{L_i + L_p}. \quad (2.10)$$

In general, with proper matching of inductances in the input circuit, it is straightforward to obtain enhancements of field sensitivity of two orders of magnitude or more.

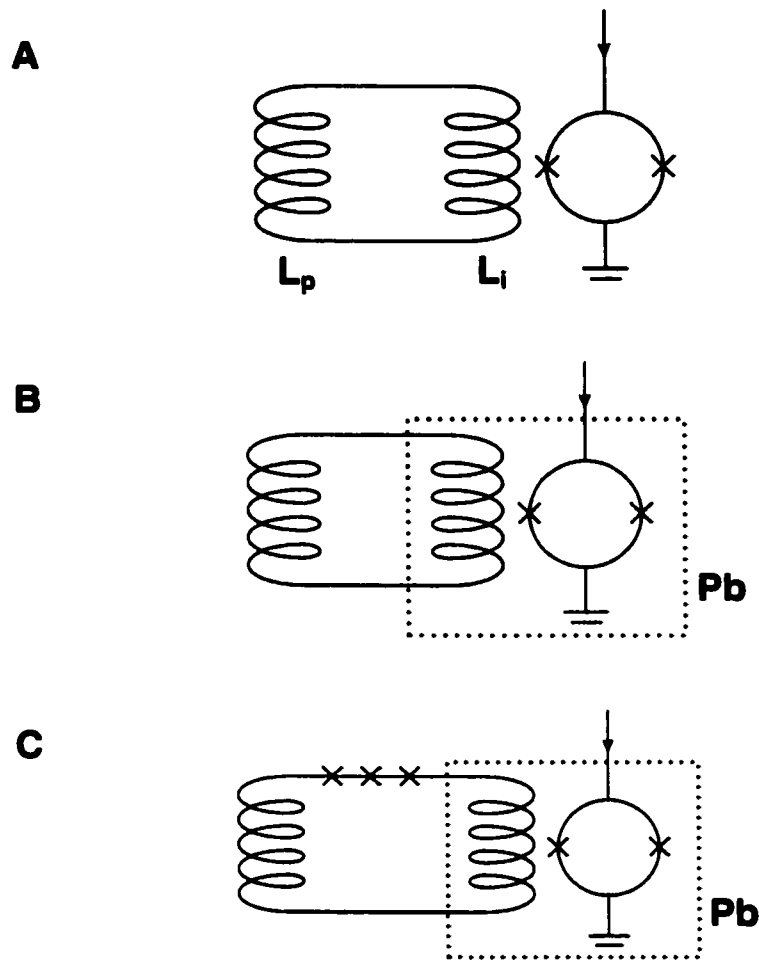


Figure 2.4. dc SQUID magnetometers. (A) dc SQUID operated with superconducting flux transformer, consisting of a pickup coil (with inductance L_p) and an input coil (with inductance L_i) which is tightly coupled to the SQUID chip. (B) As in (A), but here the SQUID chip is enclosed in a superconducting shield. (C) dc SQUID magnetometer with flux dams. The additional Josephson junctions fabricated in series with the input coil prevent excessive currents from flowing in the input circuit.

Furthermore, when the signal flux is coupled to the SQUID via a flux transformer, it is possible to shield the SQUID itself from large time-varying applied magnetic fields (such as those used to manipulate nuclear spins in an NMR experiment) by enclosing the SQUID chip in a superconducting Pb or Nb box (Figure 2.4B). These large applied fields might otherwise drive flux vortices into the junctions of the SQUID (suppressing the critical currents) or into the SQUID washer (where motion of the vortices gives rise to

flux noise in the SQUID). To shield the SQUID from flux generated by excessive currents flowing in the input coil, a series array of Josephson junctions with appropriately chosen I_c can be incorporated into the input circuit (Figure 2.4C) [19-20]. The array of junctions, known as a “flux dam”, has no effect for small signal currents; however, the input circuit opens when I_c of the flux dams is exceeded, protecting the SQUID.

In the case of a SQUID system operated with minimal magnetic shielding, it is often desirable to reduce the sensitivity of the SQUID to distant sources of interference, while maintaining high sensitivity to a nearby signal source. This is done by configuring the pickup circuit of the sensor gradiometrically [18, 21]. The first-order axial gradiometer is shown in Figure 2.5A. The counterwound pickup loops, enclosing equal areas and aligned to sense the component B_z of the magnetic field, are separated by a distance Δz , the baseline of the gradiometer. When a uniform magnetic field is applied to the gradiometer, no net flux is coupled to the flux transformer, and no currents flow in the input coil. However, when a magnetic field gradient dB_z/dz is applied, a supercurrent is induced in the flux transformer, and flux is coupled to the SQUID. For an interfering dipole source at a distance $r \gg \Delta z$, the flux coupled to the SQUID is attenuated by a factor of order $\Delta z/r$; on the other hand, a nearby signal source which is tightly coupled to only one of the pickup loops of the gradiometer is sensed with high efficiency. It is straightforward to construct higher-order gradiometers: Figure 2.5B shows a gradiometer configured to sense the component d^2B_z/dz^2 of the second-order magnetic field gradient tensor; the third-order gradiometer of Figure 2.5C rejects uniform fields as well as first- and second-order gradients, while responding to the third-order gradient d^3B_z/dz^3 .

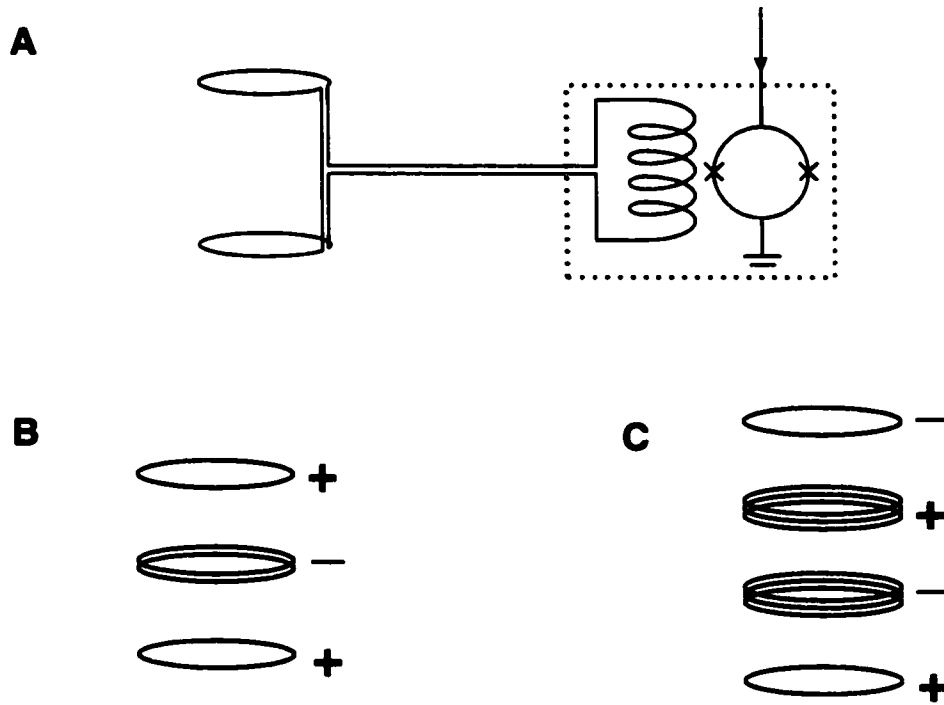


Figure 2.5. SQUID gradiometers. (A) *First-order axial gradiometer.* The device is insensitive to uniform fields but responds to the gradient dB_z/dz . (B) *Second-order gradiometric pickup loop.* The two center loops are wound in opposition to the upper and lower loops. The coil is sensitive to the component d^2B_z/dz^2 of the second-order magnetic field gradient tensor. (C) *Third-order gradiometric pickup loop.* The coil is sensitive to the gradient d^3B_z/dz^3 .

The sensitivity of a gradiometer to a nearby signal source is determined by the gradiometer sensing area A_{sense} , defined in the following manner:

$$A_{\text{sense}} = \frac{\Phi_s}{B_{\text{signal}}} = A_p \frac{M}{L_i + L_{\text{grad}}} = A_p \frac{\alpha \sqrt{L_i L}}{L_i + L_{\text{grad}}}, \quad (2.11)$$

where again Φ_s is the flux coupled to the SQUID loop, and B_{signal} is the strength of a magnetic field applied only to the sensing loop of the gradiometer; A_p is now the area of the gradiometer sensing loop (geometric area times number of turns); and L_{grad} is the total inductance of the gradiometric pickup loop.

On the other hand, the sensitivity of the gradiometer to a uniform background field B_i applied along the \hat{i} direction is determined by the effective area $(A_{\text{eff}})_i$, defined as follows:

$$(A_{\text{eff}})_i = \frac{\Phi_s}{B_i}. \quad (2.12)$$

Note that it is most convenient to express the effective area of the gradiometer as a three-component vector, as the response of the device to in-plane fields (due to slight errors in alignment) is generally comparable to the response to out-of-plane fields (due to mismatch of loop areas). The balance of the gradiometer with respect to a uniform field applied in the \hat{i} direction is determined by the ratio $(A_{\text{eff}})_i / A_{\text{sense}}$. Uniform field rejection of about 1 part in 100 is typical for an “as-made” commercial hardware gradiometer. Gradiometer balance can be improved by additional mechanical balancing (for example, by moving small superconducting paddles in the vicinity of the gradiometer pickup loops). In the majority of commercial multichannel SQUID systems for biomagnetic measurements, balance is achieved by forming appropriate linear combinations of the gradiometer signal and signals from additional SQUID reference channels. This can be done either with additional analog circuitry, or in software (see Section 6.I.1).

E. Tuned vs. Untuned Magnetometers

To this point we have considered the case where the SQUID magnetometer is operated with an untuned, superconducting input circuit (Figure 2.6A). The untuned magnetometer enables detection over a broad band, extending down to frequencies approaching 0 Hz, without a loss in sensitivity. However, in applications where signal frequencies are relatively high (above a few hundreds of kHz) and concentrated in a

relatively narrow band, it can be advantageous to tune the input circuit of the SQUID magnetometer (Figure 2.6B). In this case, an applied flux which is at the resonant frequency of the tank circuit induces a current which is amplified by the Q of the tank: there is signal gain. However, since the input circuit is no longer superconducting, the real part of the impedance in the circuit gives rise to Nyquist currents which couple a noise flux to the SQUID.

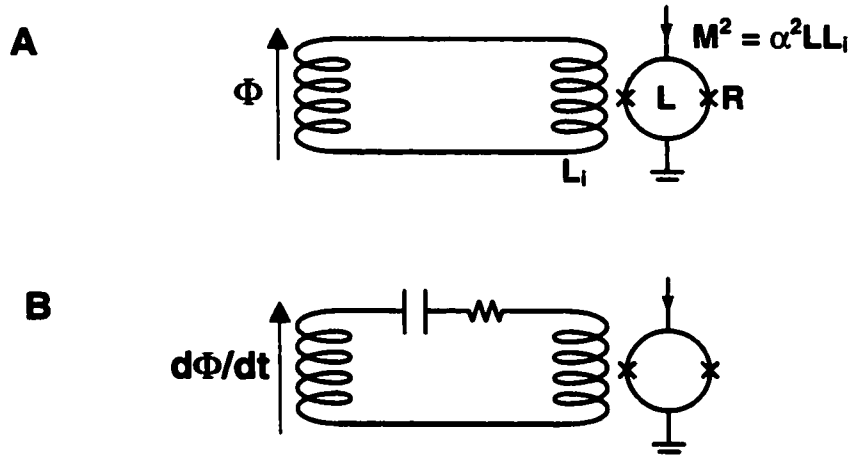


Figure 2.6. (A) Untuned magnetometer. The input circuit is superconducting, and operates on the principle of flux conservation in a superconducting loop. The current which flows in the input circuit is proportional to the flux applied to the pickup coil, independent of frequency. (B) Tuned magnetometer. The input circuit operates on the principle of Faraday induction. The voltage induced in the pickup coil is proportional to the rate of change of applied flux.

From the analysis of Clarke [22-23], we find that we can write the noise temperatures of tuned and untuned dc SQUID magnetometers as follows:

$$T_N^t(f) \approx \frac{\sqrt{S_v(f)S_I(f)}}{2k_B} \frac{\omega}{V_\Phi} \approx 7T \frac{\omega}{V_\Phi} \quad (\text{tuned}) \quad (2.13a)$$

$$T_N^u(f) \approx \frac{1}{\alpha^2} \frac{S_v(f)}{2k_B R} \frac{\omega}{V_\Phi} \approx \frac{8T}{\alpha^2} \frac{\omega}{V_\Phi} \quad (\text{untuned}), \quad (2.13b)$$

where the noise temperature of the tuned magnetometer is expressed on resonance. Here, $S_v(f)$ is the power spectral density of voltage across the SQUID; $S_I(f)$ is the power spectral density of current in the SQUID loop; and R refers to the shunt resistance of a single junction in the SQUID.

In the case of the tuned magnetometer, the overall noise temperature of the receiver has contributions from both the SQUID and the input circuit:

$$T_{\text{tot}} = T_N^t + T \quad (\text{tuned}). \quad (2.14a)$$

In the untuned case, however, the noise of the superconducting input circuit can be thought of as being compressed into a delta function at zero frequency (from the equipartition theorem, the integrated mean square noise current in the input circuit is the same in the tuned and untuned cases). Therefore, in the untuned case, the noise temperature of the receiver is simply the noise temperature of the SQUID itself:

$$T_{\text{tot}} = T_N^u \quad (\text{untuned}). \quad (2.14b)$$

For equal signal power P_0 delivered in a bandwidth B to the magnetometer pickup loops, the signal-to-noise ratios (SNR) achieved in the tuned and untuned cases are thus written as follows:

$$\text{SNR} = \frac{QP_0}{4k_B(T_N^t + T)B} \quad (\text{tuned}); \quad (2.15a)$$

$$\text{SNR} = \frac{P_0}{4k_B T_N^u B} \quad (\text{untuned}). \quad (2.15b)$$

From this analysis, then, the tuned magnetometer yields the higher SNR provided the following condition is fulfilled:

$$Q > \frac{T_N^t + T}{T_N^u} \approx \frac{1 + 7\omega/V_\Phi}{8\omega/\alpha^2 V_\Phi} \approx \frac{\alpha^2 V_\Phi}{8\omega}. \quad (2.16)$$

Choosing the typical value $\alpha^2 \sim 0.8-0.9$, and the typical transfer function $V_\Phi \sim 60 \mu\text{V}/\Phi_0 = 30 \text{ GHz}$, Clarke concludes that it is advantageous to tune if

$$fQ > 250 \text{ MHz}. \quad (2.17)$$

Therefore, at low frequencies, the untuned magnetometer is superior, as inequality (2.17) is satisfied only in the case of impractically high Q ; at frequencies of a few hundred kHz, however, the tuned magnetometer begins to win out.

The above conclusion holds when the system noise is dominated by the intrinsic noise of the receiver. However, for SQUID systems operated with only moderate magnetic shielding, system noise is often dominated by the magnetic field environment, rather than by the intrinsic noise of the sensor. In this case, the intrinsic noise of the detector is irrelevant, and for a signal concentrated in a narrow band at a fixed frequency, the tuned and untuned magnetometers perform equally well.

In the context of a SQUID-detected NMR or MRI experiment, the comparison between tuned and untuned SQUID detection is far from straightforward. In magnetic resonance experiments, one has considerable freedom in choosing the signal band, as the nuclear resonance frequency is set simply by adjusting the strength of a magnetic field. Detection of the NMR signal with a tuned magnetometer in relatively high fields of the order of 10 mT, where the proton Larmor frequency is of the order of hundreds of kHz, has the advantage that the level of magnetic field interference is relatively low at these frequencies. Moreover, due to the short skin depth (of the order of 100 μm for Cu or Al), it is straightforward to implement eddy-current shielding to eliminate any residual sources of external interference or noise. Detection with an untuned magnetometer at extremely low fields (of the order of microtesla to tens of microtesla) and therefore low

frequencies has the advantage that problems associated with inhomogeneous broadening of the NMR lines are eliminated (see Chapters 5 and 6). In addition, as the untuned magnetometer detects broadband, it is vastly more versatile than its tuned counterpart: for example, the same untuned SQUID might be used for NMR or MRI detection at frequencies of a few kHz, as well as for biomagnetic measurements at frequencies in the range of Hz to tens of Hz. The drawback to NMR detection in extremely low fields is that the level of environmental interference can be quite high at low frequencies; due to the difficulty of shielding against low-frequency magnetic fields, considerable effort is required to overcome this obstacle. These issues are discussed in greater length in Chapter 6 of this thesis.

References

1. Jaklevic R C, Lambe J, Silver A H, and Mercereau J E (1964) Quantum interference effects in Josephson tunneling *Phys. Rev. Lett.* **12** 159-160
2. Clarke J (1996) SQUID fundamentals *SQUID Sensors: Fundamentals, Fabrication, and Applications* Dordrecht: Kluwer Academic 1-62
3. Wikswo J P Jr. (1995) SQUID magnetometers for biomagnetism and nondestructive testing: important questions and initial answers *IEEE Trans. Appl. Sup.* **5** 74-120
4. Mück M, André M- O, Clarke J, Gail J, and Heiden C (1998) Radio-frequency amplifier based on a niobium dc superconducting quantum interference device with microstrip input coupling *Appl. Phys. Lett.* **72** 2885-2887
5. McDermott R, Trabesinger A H, Mück M, Hahn E L, Pines A, and Clarke J (2002) Liquid-state NMR and scalar couplings in microtesla magnetic fields *Science* **295** 2247-2249
6. Josephson B D (1962) Possible new effects in superconductive tunneling *Phys. Lett.* **1** 251-253; (1965) Supercurrents through barriers *Adv. Phys.* **14** 419-451

7. Stewart W C (1968) Current-voltage characteristics of Josephson junctions *Appl. Phys. Lett.* **12** 277-280
8. McCumber D E (1968) Effect of ac impedance on dc voltage-current characteristics of Josephson junctions *J. Appl. Phys.* **39** 3113-3118
9. Tinkham M (1996) *Introduction to Superconductivity* New York: McGraw-Hill
10. Koelle D, Kleiner R, Ludwig F, Dantsker E, and Clarke J (1999) High-transition-temperature superconducting quantum interference devices *Rev. Mod. Phys.* **71** 631-686
11. Tesche C D and Clarke J (1977) dc SQUID: noise and optimization *J. Low Temp. Phys.* **27** 301-331
12. Bruines J J P, de Waal V J, and Mooij J E (1982) Comment on “dc SQUID: noise and optimization” by Tesche and Clarke *J. Low Temp. Phys.* **46** 383-386
13. De Waal V J, Schrijner P, and Llurba R (1984) Simulation and optimization of a dc SQUID with finite capacitance *J. Low Temp. Phys.* **54** 215-232
14. Ketchen M B and Jaycox J M (1982) Ultra-low noise tunnel junction dc SQUID with a tightly coupled planar input coil *Appl. Phys. Lett.* **40** 736-738
15. Jaycox J M and Ketchen M B (1981) Planar coupling scheme for ultra low noise dc SQUIDs *IEEE Trans. Magn.* **17** 400-403
16. Clarke J, Goubau W M, and Ketchen M B (1976) *J. Low Temp. Phys.* **25** 99-144
17. Drung D (1996) Advanced SQUID readout electronics *SQUID Sensors: Fundamentals, Fabrication and Applications* Dordrecht: Kluwer Academic 63-116
18. Ketchen M B, Goubau W M, Clarke, J, and Donaldson G B (1978) Superconducting thin-film gradiometer *J. Appl. Phys.* **44** 4111-4116
19. Hilbert C, Clarke J, Sleator T, and Hahn E L (1985) Nuclear quadrupole resonance detected at 30 MHz with a dc superconducting quantum interference device *Appl. Phys. Lett.* **47** 637-639
20. Koch R H, Sun J Z, Foglietti V, and Gallagher W J (1995) Flux dam, a method to reduce extra low-frequency noise when a superconducting magnetometer is exposed to a magnetic field *Appl. Phys. Lett.* **67** 709

21. Vrba J (1996) SQUID gradiometers in real environments *SQUID Sensors: Fundamentals, Fabrication and Applications* Dordrecht: Kluwer Academic 117-178
22. Clarke J, Tesche C D, and Giffard R P (1979) Optimization of dc SQUID voltmeter and magnetometer circuits *J. Low Temp. Phys.* **37** 405-420
23. Martinis J M and Clarke J (1985) Signal and noise theory for a dc SQUID amplifier *J. Low Temp. Phys.* **61** 227-236

Chapter 3. Nuclear Magnetic Resonance

Nuclear magnetic resonance, or NMR, refers to the resonant absorption or emission of photons by atomic nuclei which are immersed in a magnetic field. The phenomenon was first observed by Rabi and coworkers in the 1930s in atomic beam experiments [1]. In 1945, Purcell at Harvard and Bloch at Stanford independently observed NMR signals from condensed matter samples [2-3]. Soon thereafter, Hahn pioneered pulse techniques for NMR spectroscopy, and his discovery of the spin echo in 1950 paved the way for many of the later developments in the field [4].

More than fifty years after its discovery, NMR has become an extraordinarily wide-ranging and versatile tool, with applications in such varied fields as condensed matter physics, molecular biology, and medicine. Because the magnetic quantum states of nuclei are extremely sensitive to the electromagnetic environment, NMR spectra yield a surprising degree of information about molecular structure and conformation.

A. NMR Basics

The basic interaction in NMR is that of the magnetic moment of a nuclear spin with an externally applied magnetic field [5-9]. For simplicity we consider the case of a spin-1/2 nucleus subjected to a uniform magnetic field $\mathbf{B} = B_0 \hat{\mathbf{k}}$ applied along the z direction (Figure 3.1). The Hamiltonian is written as

$$H = -\gamma \hbar B_0 I_z, \quad (3.1)$$

where \mathbf{I} is the spin angular momentum operator of the nucleus, and γ is its magnetogyric ratio (for the proton, $\gamma = 26.7 \times 10^7 \text{ rad T}^{-1} \text{s}^{-1}$). The eigenstates $|+\rangle$ and $|-\rangle$ correspond to nuclear spin aligned and antialigned with the magnetic field, respectively: $\langle I_z \rangle_+ = +1/2$; $\langle I_z \rangle_- = -1/2$. The energy eigenvalues are therefore

$$E = \pm \frac{\gamma \hbar B_0}{2}, \quad (3.2)$$

and the angular frequency corresponding to a transition between levels is

$$\omega_0 = \gamma B_0. \quad (3.3)$$

The frequency ω_0 is known as the Larmor frequency.

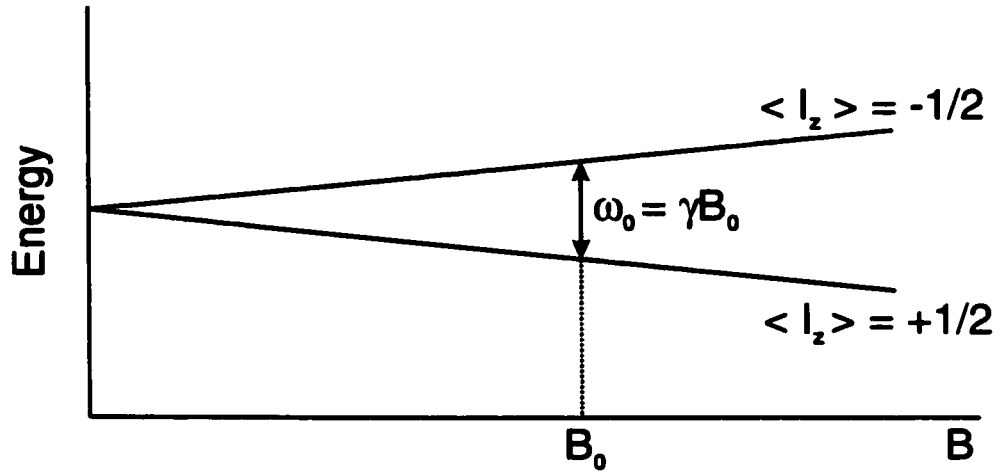


Figure 3.1. Energy level diagram for a spin-1/2 nucleus in a magnetic field.

The time evolution operator for this system is written as

$$U(t) = \exp(i\omega_0 I_z t), \quad (3.4)$$

which corresponds to a rotation about the z direction at the Larmor frequency.

To observe the resonance phenomenon, it is necessary to apply a second oscillatory field $\mathbf{B}_1(t)$ in the xy plane at a frequency ω which is close to the Larmor frequency:

$$\mathbf{B}_1(t) = B_1 (\hat{\mathbf{i}} \cos \omega t + \hat{\mathbf{j}} \sin \omega t). \quad (3.5)$$

If we transform to a frame which rotates about the z axis at the angular frequency ω , then the time dependence of \mathbf{B}_1 is removed. If we take the x-axis in the rotating frame to lie along the direction of \mathbf{B}_1 , then the effective magnetic field becomes

$$\mathbf{B}_{\text{eff}} = (B_0 - \omega/\gamma) \hat{\mathbf{k}} + B_1 \hat{\mathbf{i}}, \quad (3.6)$$

and the transformed Hamiltonian is written

$$H' = -[(\gamma\hbar B_0 - \hbar\omega)I_z + \gamma\hbar B_1 I_x] \quad (3.7)$$

(Figure 3.2). Exactly on resonance, $\omega = \omega_0$, the Hamiltonian becomes

$$H' = -\gamma\hbar B_1 I_x . \quad (3.8)$$

The time evolution operator for this Hamiltonian,

$$U'(t) = \exp(i\omega_1 I_x t), \quad (3.9)$$

corresponds to a rotation about the x direction in the rotating frame at an angular frequency

$$\omega_1 = \gamma B_1 \quad (3.10)$$

which is determined by the strength of the oscillatory magnetic field. The frequency ω_1 is known as the Rabi frequency. For $\langle I_z \rangle_{t=0} = 1/2$ and in the absence of relaxation, the expectation value of the longitudinal component of the nuclear spin evolves as

$$\langle I_z \rangle = \frac{1}{2} \cos \omega_1 t. \quad (3.11)$$

That is, the resonant field B_1 induces transitions between the nuclear magnetic sublevels.

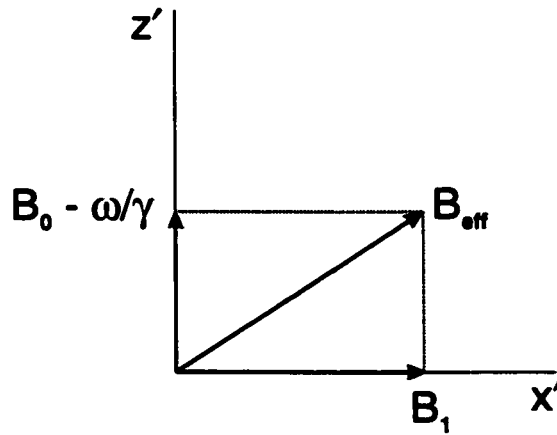


Figure 3.2 Effective magnetic field in the rotating frame.

In the simplest pulsed nuclear magnetic resonance experiment, the excitation field \mathbf{B}_1 is chosen such that its amplitude and duration τ satisfy the following condition:

$$\gamma B_1 \tau = \frac{\pi}{2}. \quad (3.12)$$

In this case, the excitation rotates the magnetic moment of the spins away from the direction of the static field into the transverse plane. Following application of the $\pi/2$ pulse, the spins evolve under the influence of Hamiltonian (3.1); the resulting precession or free induction decay (FID) can be detected, conventionally with a tank circuit which is tuned to the nuclear resonance frequency. Fourier transform of the FID yields the NMR spectrum (Figure 3.3).

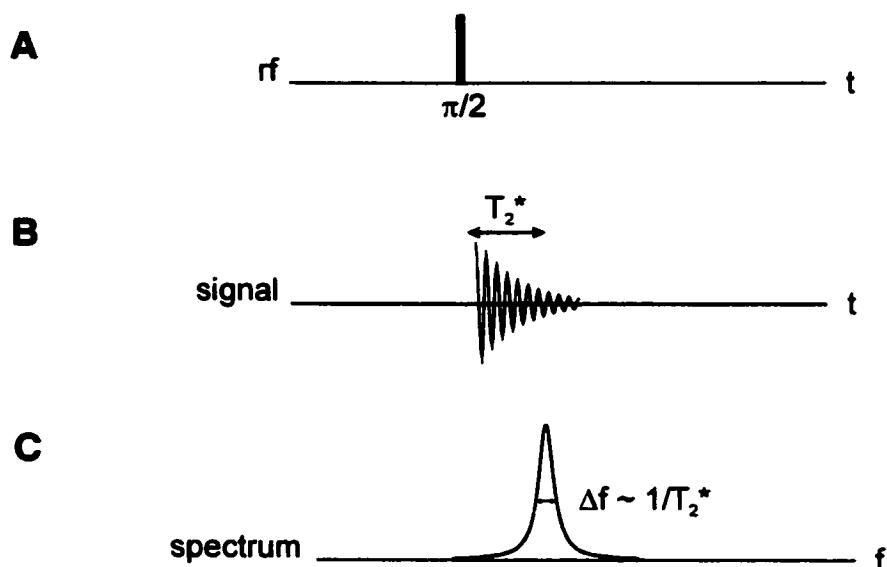


Figure 3.3. The basic pulsed NMR experiment. (A) A resonant pulse is applied which tips the sample magnetization into the transverse plane. (B) Free precession of the nuclear spins in the transverse plane produces a magnetic transient which can be detected, conventionally with a tank circuit tuned to the nuclear resonance frequency. The duration of the free induction decay (FID) is determined by the effective spin-spin relaxation time T_2^ , which is discussed in Section 3.C. (C) Fourier transform of the FID yields the NMR spectrum.*

B. Relaxation in NMR

The above simple picture of the magnetic resonance phenomenon does not take into account relaxation effects; these involve both energy exchange between spins and the lattice, as well as loss of spin phase coherence in the transverse plane. In the semiclassical picture introduced by Bloch, the time evolution of the three components of the nuclear spin magnetization \mathbf{M} is governed by the following equations:

$$\frac{dM_z}{dt} = \frac{M_0 - M_z}{T_1} + \gamma(\mathbf{M} \times \mathbf{H})_z \quad (3.13a)$$

$$\frac{dM_x}{dt} = \gamma(\mathbf{M} \times \mathbf{H})_x - \frac{M_x}{T_2} \quad (3.13b)$$

$$\frac{dM_y}{dt} = \gamma(\mathbf{M} \times \mathbf{H})_y - \frac{M_y}{T_2}. \quad (3.13c)$$

Here, M_0 is the thermal equilibrium magnetization in the static field $\mathbf{B} = B_0 \hat{\mathbf{k}}$, and T_1 and T_2 are phenomenological parameters which govern relaxation of the spin magnetization to thermal equilibrium. The spin-lattice relaxation time T_1 determines the timescale for spins to align with an external magnetic field applied in the longitudinal direction; this process involves spin-flips, and therefore exchange of energy with a thermal reservoir (the lattice). The spin-spin relaxation time T_2 is the time following excitation over which spins maintain phase coherence in the transverse plane. In the context of a pulsed NMR experiment, T_2 determines the duration of the FID (in the absence of additional broadening).

Both spin-lattice and spin-spin relaxation processes are caused by random fluctuations in the magnetic field at the location of the nucleus which are due, for example, to the dipolar fields of neighboring nuclei. These fluctuations occur on a timescale τ_c , known as the correlation time, which is a characteristic time for molecular reorientation. In the rough qualitative picture outlined in Goldman [8], the randomly fluctuating fields are viewed as a bath of phonons, capable of inducing transitions between nuclear magnetic sublevels or of destroying nuclear phase coherence. The probability of a transition between levels is proportional to the spectral density of phonons at the transition frequency. Figure 3.4 shows the spectral density of relaxation phonons as a function of frequency, plotted for three different correlation times.

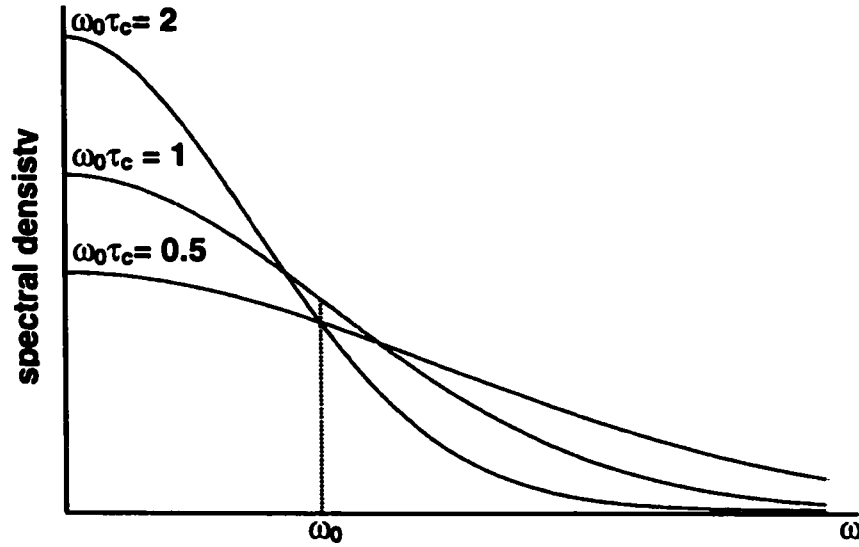


Figure 3.4. Spectral density of phonons capable of inducing nuclear relaxation, plotted for three different values of correlation time τ_c (after Goldman [8]).

The integrated power of the spectral density function is proportional to the mean square of the instantaneous field strength, and hence is independent of correlation time. On the other hand, the width of the spectral density function is given roughly by the inverse of the correlation time. Thus, for long correlation times, spectral weight is concentrated at low frequencies; as τ_c becomes shorter, spectral weight is shifted to higher frequencies, while the integrated spectral density is conserved.

Because spin-lattice relaxation involves energy exchange with the lattice and therefore transitions between the nuclear magnetic sublevels, the relaxation rate T_1 is determined by the spectral density of relaxation phonons at the Larmor frequency ω_0 . On the other hand, spin-spin relaxation processes conserve energy; the relaxation rate T_2 is therefore governed by the spectral density of relaxation phonons at zero frequency. For

this reason, T_1 and T_2 depend on correlation time as shown in Figure 3.5. The spectral density of relaxation phonons at zero frequency increases monotonically with increasing correlation time; therefore, T_2 becomes shorter and shorter as molecular motion slows and correlation times increase. However, T_1 goes through a local minimum at $\omega_0\tau_c \sim 1$, as the spectral density of relaxation phonons at the Larmor frequency is maximized for $\omega_0\tau_c \sim 1$.

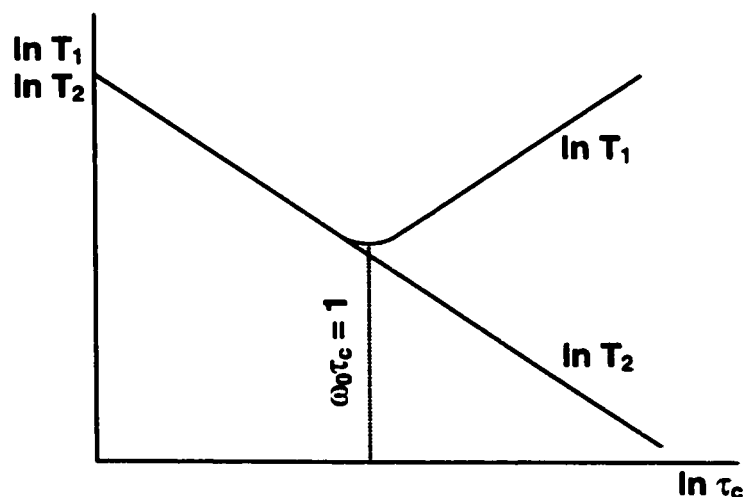


Figure 3.5. Spin-lattice (T_1) and spin-spin (T_2) relaxation times plotted as functions of correlation time τ_c .

In the extreme case of very long correlation times, $\omega_0\tau_c \gg 1$, characteristic of systems in the solid state, the spin-spin relaxation time T_2 is readily estimated from the strength of the local fields generated by neighboring nuclear dipoles, which is given by

$$B_{\text{loc}} = \frac{\mu_0\mu}{2\pi r^3}. \quad (3.14)$$

Using the typical internuclear separation $r \sim 2 \text{ \AA}$, and the proton magnetic moment $\mu_p = 1.4 \times 10^{-26} \text{ J T}^{-1}$, we find a local field strength $B_{\text{loc}} \sim 400 \text{ \mu T}$. Random orientation of the

dipolar fields with respect to an applied external field results in a broad distribution of Larmor frequencies $\Delta\omega_0 \sim \gamma B_{\text{loc}}$; as the spins evolve, the dispersion of Larmor frequencies leads to loss of phase coherence in a time which is roughly equal to the Larmor period in the dipolar field. That is,

$$T_2 \sim (\gamma B_{\text{loc}})^{-1}. \quad (3.15)$$

For a dipolar field of the order of hundreds of microtesla, we find that spin-spin relaxation times are of the order of tens of microseconds.

At the other extreme of very short correlation times, $\omega_0 \tau_c \ll 1$, characteristic of systems in the liquid state, the rapid reorientation of nuclei due to molecular motion leads to an averaging out of the dipolar fields, and hence a narrowing of the resonance line. The effect is known as motional narrowing [11]. In this case, as each nucleus evolves in the Zeeman field, it is subjected to additional local fields which fluctuate randomly with characteristic time τ_c . The accumulation of phase due to the local fields can be modeled naively as a random walk in one dimension [6]. For a random walk consisting of n steps of length τ_c , the total phase acquired by a nucleus is roughly $n^{1/2} \gamma B_{\text{loc}} \tau_c$. Phase coherence is lost in a time $n \tau_c$ for which $n^{1/2} \gamma B_{\text{loc}} \tau_c \sim 1$. Thus, we find

$$T_2 \sim (\gamma^2 B_{\text{loc}}^2 \tau_c)^{-1}. \quad (3.16)$$

Therefore, molecular motion leads to an increase in T_2 , and a corresponding decrease in the NMR linewidth, by roughly the factor $\gamma B_{\text{loc}} \tau_c$. Typical correlation times in liquids are of the order of 100 ps; for $\Delta\omega_0$ of the order of 100 kHz (typical for protons), we find T_2 to be of the order of 1 s.

C. Inhomogeneous Broadening

While the intrinsic widths of the NMR lines are of the order of 1 Hz in liquid state systems, exquisite homogeneity of the externally imposed static field is required to achieve these linewidths experimentally. Instead, variation of the strength of the Zeeman field over the volume of the sample will typically lead to a distribution of Larmor frequencies in the spin ensemble; as the spins evolve at slightly different frequencies, they lose phase coherence, resulting in a rapid decay of signal amplitude (in the time domain) and a broadening of the NMR line (in the frequency domain). In general, the NMR linewidth will have both homogeneous (intrinsic) and inhomogeneous contributions. We define an effective dephasing time T_2^* in the following manner:

$$1/T_2^* = 1/T_2 + 1/T_2', \quad (3.17)$$

where $1/T_2$ is the intrinsic spin-spin relaxation rate, while $1/T_2'$ represents additional dephasing due to field inhomogeneity. For example, in a high-field spectrometer operating at 500 MHz, homogeneity of 20 parts per billion over the sample volume leads to a dispersion of Larmor frequencies of roughly 10 Hz, corresponding to T_2^* of order 100 ms. In this case, inhomogeneous broadening renders it impossible to resolve spectral features at the level of a few Hz; moreover, inhomogeneous line broadening leads to a degradation of SNR. In a state-of-the-art high-field NMR spectrometer, field homogeneity is achieved by supplementing the superconducting magnet with a sophisticated set of shim coils.

D. Spin Echoes

Phase coherence which is lost due to field inhomogeneity can be recovered using the technique of spin echoes, which was discovered by Erwin Hahn in 1950 [4]. The spin

echo can be understood naively in the following manner. We imagine an ensemble of spins which is immersed in a strong, inhomogeneous magnetic field oriented in the z direction (Figure 3.6). At a time $t = 0$, a $\pi/2$ pulse rotates the sample magnetization into the transverse plane. The spins now begin to precess about the Zeeman field; however, due to the fact that the Zeeman field is not perfectly homogeneous, spins at different locations precess with slightly different Larmor frequencies. The dispersion of Larmor frequencies causes the net sample magnetization to diminish as the spins lose phase coherence and to “fan out” in the transverse plane. The spins are allowed to evolve in this manner for a time τ . At $t = \tau$, however, a π pulse is applied (in Figure 3.6B, the π pulse is shown to have the same phase as the initial $\pi/2$ pulse). The effect of the π pulse is to invert the phase of all the spins in the sample. During the interval from $t = \tau$ to $t = 2\tau$, as the spins continue to evolve in the inhomogeneous Zeeman field (preserving the original sense of precession), phase coherence is restored. At the time $t = 2\tau$ the echo amplitude is maximum.

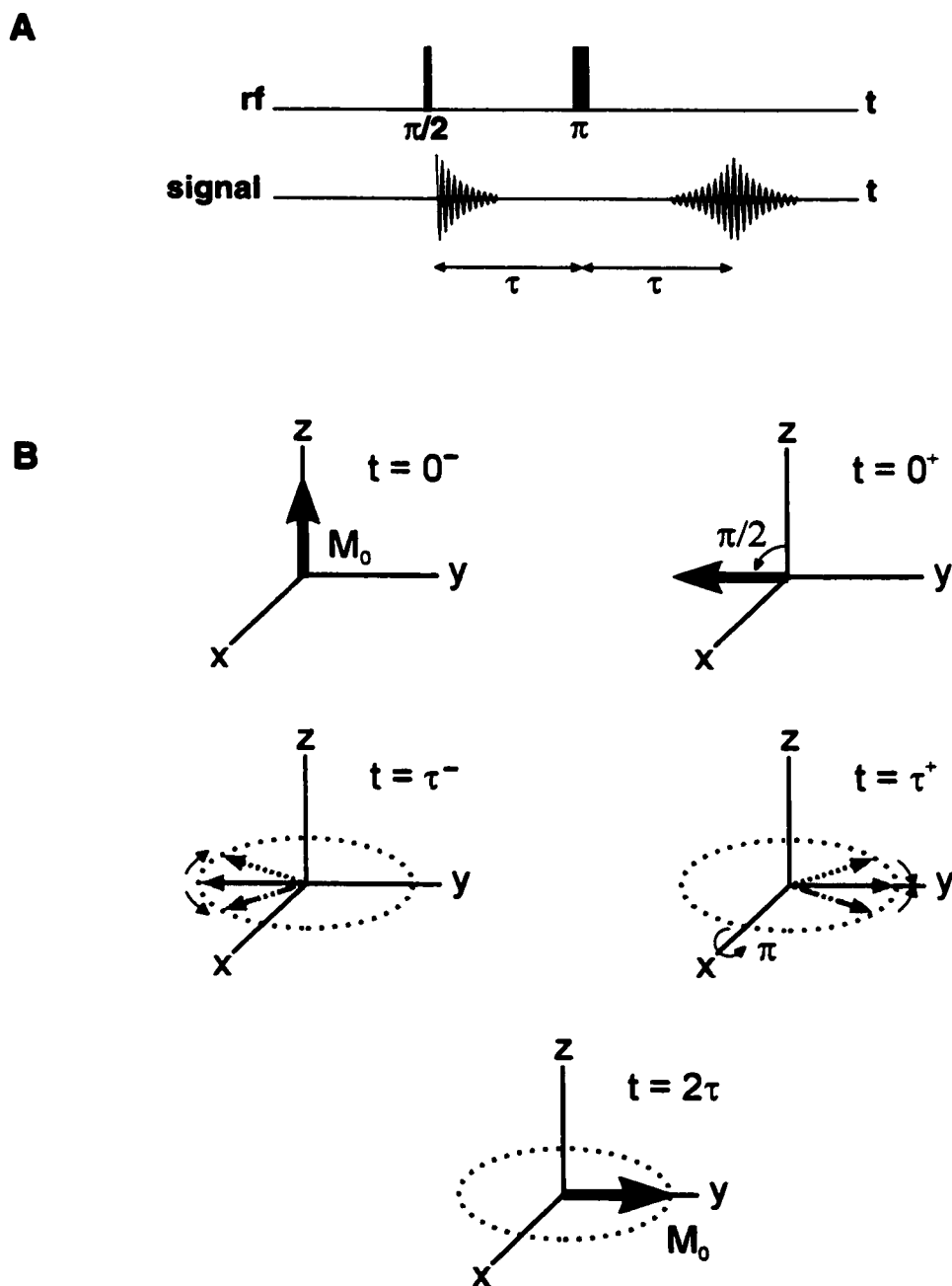


Figure 3.6. Hahn spin echo. (A) NMR pulse sequence. (B) Rotating frame cartoon. At time $t=0$, a $\pi/2$ pulse is applied which tips the spins into the transverse plane. The spins undergo free precession for a time τ ; poor homogeneity of the Zeeman field leads to a rapid loss of phase coherence. At time $t=\tau$, a π pulse is applied which inverts the phase of the nuclear spins. During the interval from τ to 2τ , phase coherence is restored.

E. Interactions in Liquid-State NMR

In liquid-state NMR spectroscopy, the isotropic parts of the chemical shift and the indirect interaction, or J-coupling, give rise to shifts and splittings, respectively, in the NMR lines. These features yield valuable information about molecular structure and conformation. The chemical shift and J Hamiltonians are discussed briefly below; for a more complete description of the interactions, including those which occur in the solid state, the reader is referred to [5-9].

1) Chemical Shift

Diamagnetic screening of an applied magnetic field by the electron cloud which surrounds the nucleus gives rise to a shift in nuclear resonance frequency [12-14]. This so-called chemical shift scales with the strength of the applied field. In the case of a liquid sample, the chemical shift Hamiltonian is written simply as

$$H_{c.s.} = -\gamma B \sigma I_z, \quad (3.18)$$

where the chemical shift σ is a small number, typically expressed in ppm. Chemical shifts increase with atomic number, due to the increasing size of the electron cloud. In the case of the proton, chemical shifts range to around 10 ppm. For the nucleus ^{129}Xe , which has a large and easily polarized electron cloud, chemical shifts range to hundreds of ppm.

The increase of chemical shift dispersion with increasing magnetic field strength has been a major impetus in the continuing drive to higher magnetic fields in commercial liquid-state spectrometers. At the low magnetic field strengths (under a few millitesla) where the majority of SQUID NMR studies are performed, chemical shift information is typically buried inside the natural width of the NMR lines; recently, however, ^{129}Xe

chemical shifts have been observed at a field of 2.5 mT with a spectrometer based on a high- T_c SQUID [15].

2) *J-coupling*

In addition to through-space dipolar coupling, which is averaged away in the liquid state, nuclei in a molecule experience an indirect coupling which is mediated by the electrons in the bonding orbitals and to which the nuclei are coupled via the hyperfine interaction [16-18]. The Hamiltonian for this so-called scalar coupling or J-coupling can be written as

$$H_J = 2\pi J \mathbf{I}_1 \cdot \mathbf{I}_2, \quad (3.19)$$

where \mathbf{I}_1 and \mathbf{I}_2 are the spins of the coupled nuclei, and the parameter J expresses the strength of the coupling.

In the so-called weak coupling limit $J \ll \Delta$, where $\Delta = |\omega_1 - \omega_2|$ is the difference in Larmor frequency of the two nuclear species (due either to a difference of chemical shift, or to a difference in magnetogyric ratio), we retain only the secular part of the J Hamiltonian, which now becomes

$$H_J = 2\pi J I_{1z} I_{2z}. \quad (3.20)$$

The effect of this reduced J Hamiltonian is to give rise to splittings in the NMR lines. This can be understood from the following simple picture. We imagine two spin-1/2 nuclei, A and B, which interact via electron-mediated scalar coupling. In the high-temperature limit, nucleus A is equally likely to find itself in a spin-up or a spin-down state. When nucleus A is spin-up, it produces a field which adds to the Zeeman field seen by nucleus B. When nucleus A is spin-down, its field subtracts from the Zeeman field

seen by nucleus B. Therefore the resonance line from nucleus B is split into a doublet centered on the resonance of the “bare” nucleus, with equal intensity in the two lines. Scalar coupling of two equivalent nuclei A to a single nucleus B splits the resonance of nucleus B into three lines centered on the resonance of the bare nucleus, with intensities in the ratio 1:2:1; the resonance of nucleus A is split into a doublet. Similarly, scalar coupling to n equivalent nuclei A splits the resonance of nucleus B into n+1 equally spaced lines; the relative intensity of the *i*th line is determined from the binomial coefficient $\binom{n}{i-1}$. Figure 3.7 shows the J-coupled stick spectra obtained in the case of sp^3 hybridized ^{13}C .

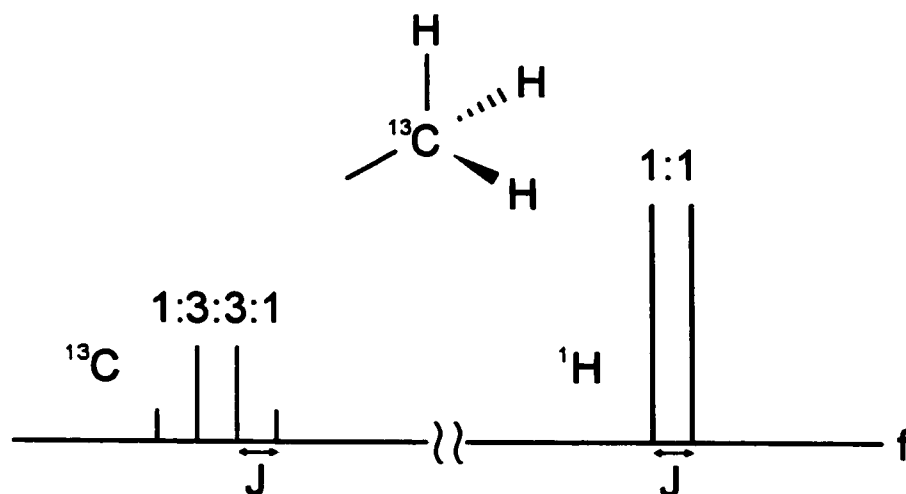


*Figure 3.7. J-coupled stick spectra obtained in sp^3 hybridized ^{13}C . Scalar coupling splits the resonance of the three equivalent protons into a doublet; the size of the splitting is simply the coupling strength *J*. Scalar coupling to the three protons splits the ^{13}C resonance (at a Larmor frequency which is roughly 0.25 times that of the proton) into four equally spaced lines, with relative intensity in the ratio 1:3:3:1.*

In contrast to the chemical shift, the J-coupling is independent of the strength of the applied magnetic field. This fact makes it possible to obtain spectroscopic

information from samples in the liquid state in extremely low magnetic fields, of the order of microtesla [19-20]. Some typical scalar coupling strengths are listed in Table 3.1.

Table 3.1. Typical ranges of heteronuclear J coupling values (from Jardetzky and Roberts [21]).

$^1\text{H} - ^2\text{H}$	$^1\text{H} - \text{C} - ^2\text{H}$	~2 Hz
$^1\text{H} - ^{13}\text{C}$	$^1\text{H} - ^{13}\text{C} (\text{sp}^3)$	110 – 130 Hz
	$^1\text{H} - \text{C} - ^{13}\text{C}$	~5 Hz
	$^1\text{H} - \text{C} = ^{13}\text{C}$	~2 Hz (ethylene)
$^1\text{H} - ^{15}\text{N}$	$^1\text{H} - ^{15}\text{N}$	61 Hz (ammonia)
	$^1\text{H} - ^{15}\text{N}$	89 – 95 Hz (peptides)
	$^1\text{H} - \text{C} - ^{15}\text{N}$	15 – 23 Hz (peptides)
$^1\text{H} - ^{17}\text{O}$	$^1\text{H} - ^{17}\text{O}$	70 Hz
	$^1\text{H} - \text{C} - ^{17}\text{O}$	8 – 10 Hz
$^1\text{H} - ^{19}\text{F}$	$^1\text{H} - \text{C} - ^{19}\text{F}$	40 – 50 Hz
	$^1\text{H} - \text{C} - \text{C} - ^{19}\text{F}$	5 – 20 Hz
$^1\text{H} - ^{31}\text{P}$	$^1\text{H} - ^{31}\text{P}$	170 – 230 Hz (trivalent ^{31}P)
		700 – 900 Hz (pentavalent ^{31}P)
	$^1\text{H} - \text{O} - ^{31}\text{P}$	15 – 25 Hz
	$^1\text{H} - \text{C} - \text{O} - ^{31}\text{P}$	2 – 20 Hz

As one moves away from the weak coupling regime $J \ll \Delta$, the simple multiplet structure of the J spectrum is lost. Nevertheless, it is possible to interpret the spectra either analytically or through numerical simulations [22]. In the extreme strong coupling regime $\Delta = 0$, however, direct detection of J couplings is impossible (this is proved, e.g. in Goldman [8]); for this reason it is not possible to observe homonuclear scalar

couplings in low field, as all nuclei of a given species appear equivalent (due to the vanishing chemical shift).

F. Non-resonant Spin Manipulation

In a conventional pulsed NMR experiment, the $\pi/2$ pulse which initiates the experiment is produced by a radiofrequency burst which is resonant with the nuclear spins. Alternatively, it is possible to induce precession by suddenly switching the direction of the Zeeman field. In 1950 Varian and Packard performed the following experiment [23]. A sample of water was polarized in a field of around 10 mT, which was oriented in a direction orthogonal to that of the magnetic field of the Earth ($B_{\text{Earth}} \sim 50 \mu\text{T}$). Nonadiabatic turnoff of the polarizing field produced an effective $\pi/2$ pulse; the researchers recorded a proton FID in the Earth's field at a frequency around 2 kHz. The condition for nonadiabatic turnoff of the polarizing field can be written as

$$\frac{dB}{dt} \gg \gamma B^2, \quad (3.21)$$

where B refers to the instantaneous strength of the magnetic field.

In this type of experiment, the sample magnetization is determined by the strength of the polarizing field, which can be orders of magnitude higher than the strength of the measurement field; moreover, the polarizing field need not be homogeneous. On the other hand, the width of the NMR line is determined by the homogeneity of the much weaker measurement field. Of course it is much easier to create a low magnetic field with high relative homogeneity than it is to create a high magnetic field with high relative homogeneity. Beyond this, however, the NMR linewidth is determined by the absolute homogeneity of the measurement field, which scales linearly with the strength of the

measurement field for a fixed relative homogeneity. For this reason it is trivial to achieve narrow NMR lines in low field.

In the case of conventional Faraday-law detection, measurement in low fields entails considerable signal loss due to the frequency-dependent sensitivity of the detector (to compensate for the loss in sensitivity, the Varian-Packard experiment was performed on a rather large sample, with volume of order 1 L). In the case of detection with an untuned SQUID magnetometer, however, the integrated intensity of the NMR signal is independent of the strength of the measurement field for a fixed sample magnetization. Measurement in low field therefore leads to an enhancement of both SNR and resolution. This point is central to the SQUID-detected NMR and MRI experiments discussed in Chapters 5 and 6.

References

1. Rabi I I, Millman S, Kusch P, and Zacharias J R (1939) *Phys. Rev.* **55** 526
2. Purcell E M, Torrey H C, and Pound R V (1946) Resonance absorption by nuclear magnetic moments in a solid *Phys. Rev.* **69** 37
3. Bloch F, Hansen W W, and Packard M (1946) Nuclear induction *Phys. Rev.* **69** 127
4. Hahn E L (1950) Spin echoes *Phys. Rev.* **80** 580-594
5. Abragam A (1961) *The Principles of Nuclear Magnetism* Oxford: Clarendon Press
6. Slichter C P (1990) *Principles of Magnetic Resonance* Berlin: Springer
7. Ernst R R, Bodenhausen G, and Wokaun A (1987) *Principles of Nuclear Magnetic Resonance in One and Two Dimensions* Oxford: Clarendon Press
8. Goldman M (1988) *Quantum Description of High-Resolution NMR in Liquids* Oxford: Clarendon Press

9. Fukushima E and Roeder S B W (1981) *Experimental Pulse NMR – a Nuts and Bolts Approach* Reading, MA: Addison-Wesley
10. Redfield A G (1957) On the theory of relaxation processes *IBM J.* **1** 19-31
11. Bloembergen N, Purcell E M, and Pound R V (1948) Relaxation effects in nuclear magnetic resonance absorption *Phys. Rev.* **73** 679-712
12. Proctor W G and Yu F C (1950) The dependence of a nuclear magnetic resonance frequency upon chemical compound *Phys. Rev.* **77** 717
13. Dickinson W C (1950) Dependence of the F^{19} nuclear resonance position on chemical compound *Phys. Rev.* **77** 736-737
14. Ramsey N F (1950) Magnetic shielding of nuclei in molecules *Phys. Rev.* **78** 699-703
15. Saxena S, Wong-Foy A, Moulé A, Seeley, J A, McDermott R, Clarke J, and Pines A (2001) Resolution of ^{129}Xe chemical shifts at ultralow magnetic field *J. Am. Chem. Soc.* **123** 8133-8134
16. Hahn E L and Maxwell D E (1952) Spin echo measurements of nuclear spin coupling in molecules *Phys. Rev.* **88** 1070-1084
17. Ramsey N F and Purcell E M (1952) Interactions between nuclear spins in molecules *Phys. Rev.* **85** 143-144
18. Gutowsky H S, McCall D W, and Slichter C P (1953) Nuclear magnetic resonance multiplets in liquids *J. Chem. Phys.* **21** 279-292
19. Béné G J (1980) Nuclear magnetism of liquid systems in the earth field range *Phys. Rep.* **58** 213-267
20. McDermott R, Trabesinger A H, Mück M, Hahn E L, Pines A, and Clarke J (2002) Liquid-state NMR and scalar couplings in microtesla magnetic fields *Science* **295** 2247-2249
21. Jardetzky O and Roberts G C K (1981) *NMR in Molecular Biology* New York: Academic
22. Trabesinger A H, McDermott R, Clarke J, and Pines A unpublished
23. Packard M and Varian R (1954) Free nuclear induction in the Earth's magnetic field *Phys. Rev.* **93** 941

Chapter 4. Magnetic Resonance Imaging

A. Introduction

The idea of using NMR to acquire images of objects containing nuclear spins was proposed independently by Lauterbur [1] and by Mansfield and Grannell [2] in the early 1970s. The basic notion is as follows. When a sample containing NMR-active nuclei is subjected to both a homogeneous static magnetic field and known magnetic field gradients, the Larmor frequency of spins in the sample becomes a known function of their location [3-5]. From the NMR spectrum, therefore, it is possible to extract information about the spatial distribution of nuclear spins in the sample. The simplest case is that of a one-dimensional projection. The sample is placed in a uniform field oriented in the z direction $\mathbf{B} = B_0 \hat{\mathbf{k}}$. In addition to the uniform field, a constant magnetic field gradient $G_z \equiv dB_z/dz$ is applied. The local magnetic field at a point within the sample is then given by

$$B(z) = B_0 + z G_z. \quad (4.1)$$

The local Larmor frequency $\omega(z)$ therefore becomes

$$\omega(z) = \gamma(B_0 + z G_z). \quad (4.2)$$

Since the strengths of the applied magnetic field and field gradient are known, it is possible to map directly from Larmor frequency to position along the z axis. The NMR spectrum obtained from the sample yields a projection of nuclear spin density onto the z axis (Figure 4.1).

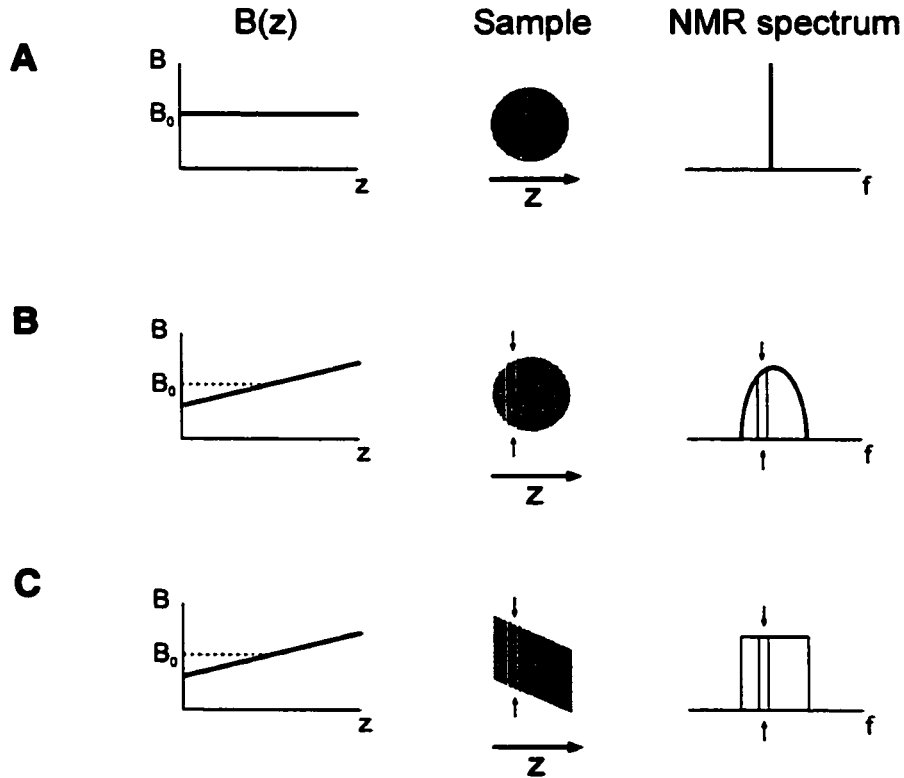


Figure 4.1. One-dimensional MRI projection with frequency encoding. (A) Circular sample placed in a uniform magnetic field. (B) Circular sample immersed in a magnetic field with constant field gradient G_z . (C) Trapezoidal sample immersed in a magnetic field with constant field gradient G_z .

B. Projection Reconstruction

Frequency encoding in a static magnetic field gradient yields a one-dimensional map of nuclear spin density projected onto the gradient direction. In order to obtain a

two- or three-dimensional image of an object, it is sufficient to acquire a number of one-dimensional projections along different directions, by rotating the direction of the applied magnetic field gradient. In the case of a two-dimensional projection, the gradient direction is swept in a plane, while in the case of a full three-dimensional image the gradient direction is varied over the unit sphere. From the collection of one-dimensional projections it is possible to reconstruct the full image of the object.

To acquire a two-dimensional cross-sectional image in the xy plane, for example, the gradient direction is swept by tuning the relative strength of the gradient fields $G_x \equiv dB_z/dx$ and $G_y \equiv dB_z/dy$, subject to the constraint of constant resultant gradient strength $G = (G_x^2 + G_y^2)^{1/2}$. The full image is obtained by varying the gradient direction $\phi = \tan^{-1}(G_x/G_y)$ over the range from 0° to 180° (Figure 4.2). Image reconstruction is performed by a technique is known as back projection [6], which developed from methods originally used for X-ray computed tomography (CT). Each one-dimensional spectrum is smeared across the plane at the appropriate angle; the intensities of the spectra are summed at each point. Filters applied to the individual spectra eliminate “starring” artifacts due to the projection algorithm.

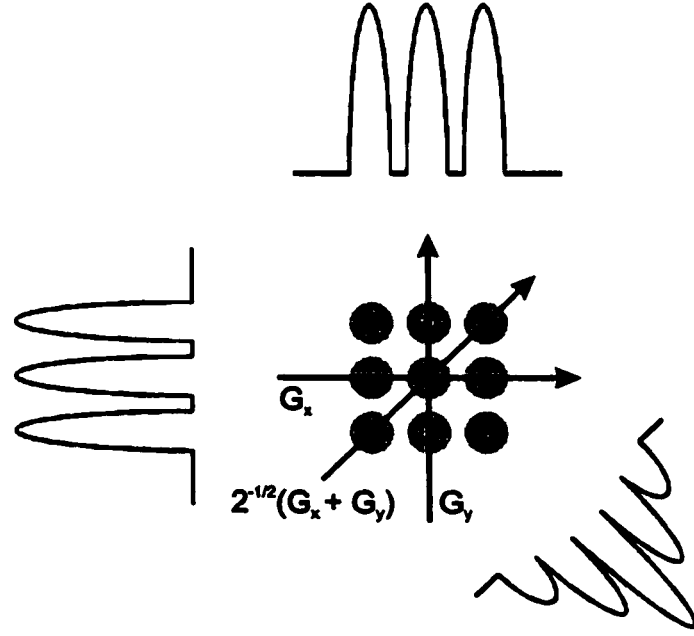


Figure 4.2. Projection reconstruction in two dimensions. The direction of the magnetic field gradient is varied in the plane, subject to the constraint of fixed gradient strength. For each gradient direction, a one-dimensional MRI projection is acquired. The individual spectra are then projected across the plane at the appropriate angles, as indicated in the figure. The intensities of the individual projections are summed at each point.

C. Fourier Imaging

Instead of using the Larmor frequency of the spins to encode the image, it is possible to encode the image in the phase of the precessing spins. For simplicity we consider the case of a two-dimensional slice of spins located in the xy plane. Following excitation of the slice, the application of gradients G_x and G_y for duration t_x and t_y , respectively (Figure 4.3), causes spins at a location $\mathbf{r} = (x, y)$ to acquire a phase which is given by

$$\theta = \gamma (G_x t_x x + G_y t_y y). \quad (4.3)$$

We can define the following wave vector:

$$\mathbf{k} \equiv (\gamma G_x t_x, \gamma G_y t_y). \quad (4.4)$$

The NMR signal detected from the sample following the turnoff of the gradient pulses is given by

$$S(\mathbf{k}) = \int \exp(-i\mathbf{k} \cdot \mathbf{r}) \rho(\mathbf{r}) d\mathbf{r} , \quad (4.5)$$

where $\rho(\mathbf{r})$ is the spin density at the point \mathbf{r} (here and in the following we neglect spin relaxation and dephasing due to spurious gradients). We see that the nuclear spin density $\rho(\mathbf{r})$ and the NMR signal amplitude $S(\mathbf{k})$ are obtained from one another via a Fourier transform. If one varies \mathbf{k} (by incrementing either the gradient strength or the duration of the gradient pulses) and acquires NMR signals at each value of \mathbf{k} , it is possible to build up a map of the sample in reciprocal space. Application of the two-dimensional Fourier transform

$$\rho(\mathbf{r}) = \frac{1}{(2\pi)^3} \int \exp(i\mathbf{k} \cdot \mathbf{r}) S(\mathbf{k}) d\mathbf{k} \quad (4.6)$$

yields the real-space map of spin density in the sample.

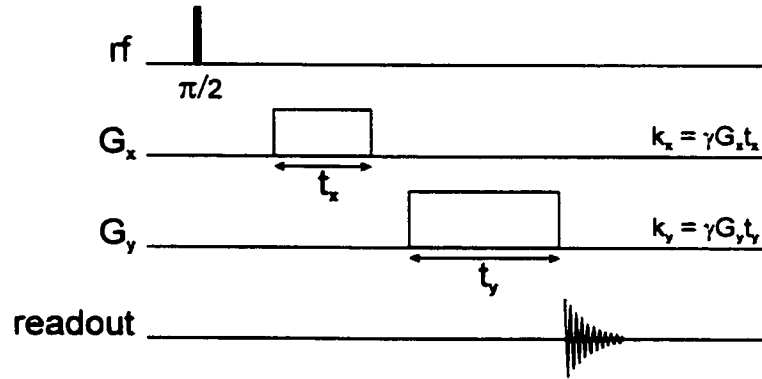


Figure 4.3. Fourier imaging in two dimensions. Application of gradients G_x and G_y for duration t_x and t_y , respectively, causes spins at location $\mathbf{r} = (x, y)$ to acquire a phase $\theta = k_x x + k_y y = \gamma G_x t_x x + \gamma G_y t_y y$. The amplitude of the NMR signal yields one point of the function $S(\mathbf{k})$, the Fourier transform of $\rho(\mathbf{r})$, the real-space spin density of the sample.

It is rather time consuming to cover reciprocal space in this point-by-point fashion. More commonly, phase encoding is performed in one dimension (say, k_x), and the signal is detected in the presence of a frequency-encoding gradient in the second dimension (say, k_y) (Figure 4.4). The time trace of the NMR signal covers a line in reciprocal space oriented in the k_y direction at constant value of k_x , determined by the strength and duration of the phase-encoding gradient. The entire two-dimensional reciprocal space is covered in a raster scan, by incrementing the value of k_x . Again, the real-space image is obtained by the usual two-dimensional Fourier transform.

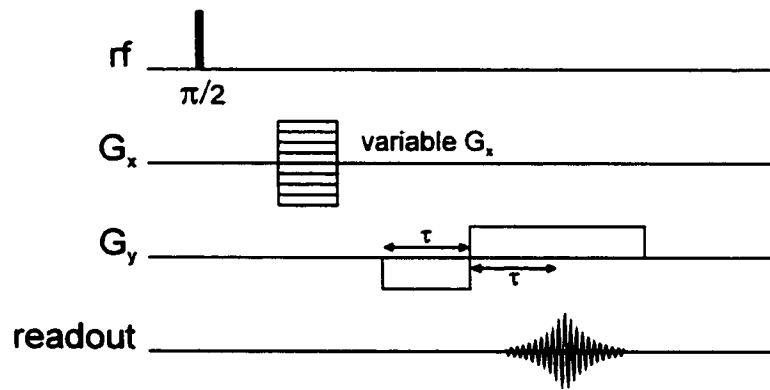


Figure 4.4. Two-dimensional Fourier imaging with both phase- and frequency-encoding gradients. In this figure, the NMR signal is formed with a gradient echo [3-5]. The time trace of the NMR signal corresponds to a line scan in reciprocal space in the direction k_y , at a value of k_x which is fixed by the strength and duration of the phase-encoding gradient G_x .

A straightforward extension of this scheme known as echo-planar imaging (EPI) allows acquisition of a full two-dimensional MRI with only a single excitation pulse [3-5]. The sequence is shown in Figure 4.5A. Following an initial pulse to offset to the maximum value of k_x , the k_x direction is scanned back through the origin with a fixed gradient strength G_x . Large amplitude gradients G_y are applied in the other direction, and are reversed at regular intervals to form gradient echoes. The effect is to scan back and

forth across reciprocal space in the k_y direction. The resulting raster scan of reciprocal space is shown in Figure 4.5B. EPI is the most commonly used sequence in clinical scanners. Examples of images obtained with EPI are shown in Figure 4.6.

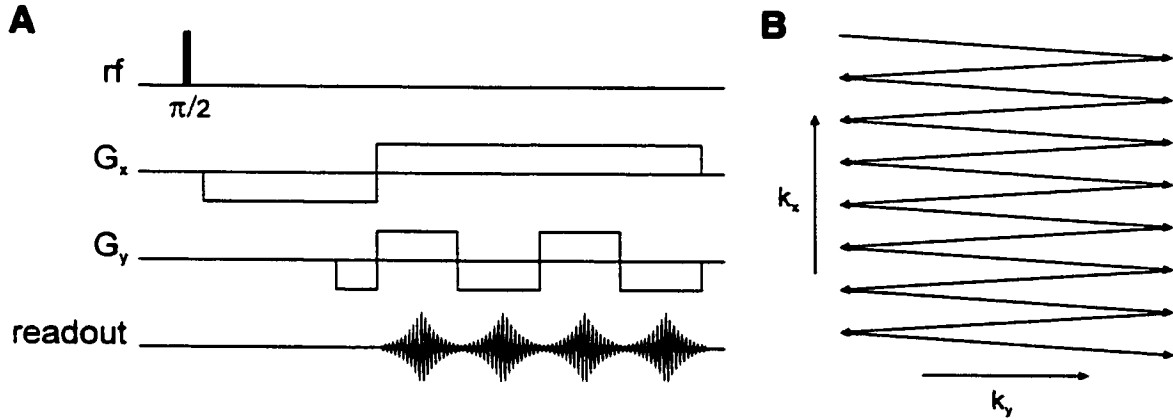


Figure 4.5. Echo-planar imaging (EPI). This scheme allows acquisition of a full two-dimensional MRI with a single excitation pulse, as described in the text. (A) NMR pulse sequence. (B) The corresponding raster scan of reciprocal space.

The numerical algorithms for Fourier image reconstruction are generally more robust and easier to implement than those for projection reconstruction. Moreover, Fourier reconstruction is very versatile, and is easily adapted to a wide variety of MRI experiments, such as those designed to image fluid flow and diffusion [7]. By and large, projection reconstruction is used only in situations where short spin-spin relaxation times make it impossible to acquire multiple echo signals following a single excitation pulse.

However, it can be shown that projection reconstruction and Fourier reconstruction yield images of roughly equal SNR per unit averaging time [8]. Furthermore, projection reconstruction has the advantage of minimal hardware and electronics requirements, as the one-dimensional scans of a projection reconstruction experiment are acquired under fixed gradient strengths (whereas Fourier reconstruction

relies on large-amplitude, pulsed magnetic field gradients). In the case of SQUID detection, projection reconstruction is perhaps the more attractive technique at first glance, as the large time-varying gradient fields needed for a Fourier reconstruction experiment can considerably complicate SQUID operation.

D. T_1 Contrast Imaging

In contrast to X-ray tomography, which yields images of the denser structures in the human body, MRI is sensitive to structures with high proton density, i.e., soft tissues and organs. Furthermore, variations in relaxation times among different types of soft tissue enable a special class of imaging experiments – so-called T_1 contrast experiments – which allow differentiation of tissue types, and thereby yield a high degree of detail and anatomical information [8]. In their most basic form, T_1 contrast experiments involve acquiring MRIs with different repetition times: for long repetition times, nearly all regions of the sample have recovered to near-full magnetization prior to application of the next $\pi/2$ pulse; for short repetition times, however, magnetization has recovered substantially only in those regions of the sample where T_1 is short, so that these regions are more heavily weighted in the image. The T_1 contrast may be due to local introduction of a relaxation agent (such as paramagnetic gadolinium) [9], or it may be the intrinsic T_1 contrast of the tissues involved. For example, spin-lattice relaxation times at 100 MHz in healthy tissue span a range from roughly 0.3 s to 1.0 s; in malignant tissue, relaxation times are significantly longer, generally in excess of 1 s [8]. T_1 weighted MRI is therefore a fast, non-invasive technique for determining whether a tumor is benign or malignant.

Very generally, relaxation times in tissue are determined by the degree to which the rotational motion of the water molecules is restricted or free. For water molecules

which are free, correlation times τ_f are of the order of 10^{-12} s, and relaxation times are similar to those for pure water. In the case where water molecules are to some degree bound, however, correlation times τ_b are in the range 10^{-9} - 10^{-8} s; for these spins, motional narrowing is incomplete and relaxation is faster. If we adopt a simple two-phase model of tissue, in which free and bound spins which exchange on a characteristic time scale $\tau_e \ll T_1$ [8], the spin-lattice relaxation rate can be expressed as

$$1/T_1 = (1/T_1)_b P_b + (1/T_1)_f (1-P_b), \quad (4.7)$$

where $(1/T_1)_b$ denotes the spin-lattice relaxation rate in the bound phase; $(1/T_1)_f$ denotes the spin-lattice relaxation rate in the free phase; and P_b is the fraction of bound water. At typical imaging frequencies, $(1/T_1)_b \gg (1/T_1)_f$; therefore, relaxation is determined by τ_b , the correlation time for spins in the bound phase.

At low field and therefore low frequency, T_1 contrast is greater between spins with different correlation times. This is due to the fact that the spectral density of relaxation phonons is more sharply dependent on correlation time at low frequency than it is at high frequency, as discussed in Section 3.B. In the context of clinical MRI, this means that (neglecting the important issue of SNR) magnetic resonance images acquired in low field will, in principle, be of higher quality than similar images acquired in high field. The enhanced T_1 contrast in the Earth's field range has been demonstrated elegantly by Planinšič *et al.* [10], and is one of the prime motivations for imaging in low magnetic field.

E. Practical high field MRI

At the writing of this thesis, the clinical standard for human MRI is 1.5 T, corresponding to a proton Larmor frequency of 64 MHz. Figure 4.6 shows typical images (coarse and fine scans) acquired from the human head using a commercial MRI scanner. A birdcage resonator (designed to produce a homogeneous B_1 field over the volume of the head) was used as both transmit and receive coil; the static magnetic field was shimmed to yield an inhomogeneously broadened NMR linewidth of 33 Hz. The SNR achieved from the head following a single $\pi/2$ pulse was of the order of 10^4 without encoding gradients applied.

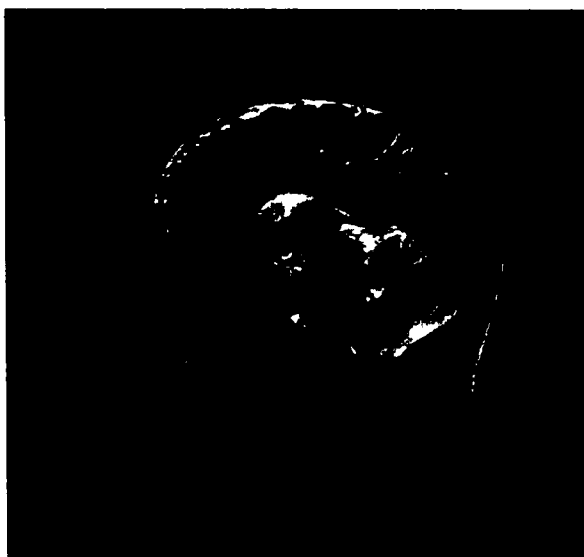
A

Figure 4.6. High-field MRIs acquired from a human head using EPI. (A) Low-resolution scan. The total acquisition time was 1.2 s. (B) High-resolution scan. The total acquisition time was 13.3 s. The details of the experiments are presented in the text. Images courtesy of Dr. Andreas H. Trabesinger, ETH.

B

The image of Figure 4.6A was acquired from a 10 mm-thick slice using an EPI sequence with echo time 2 ms, repetition time 7.3 ms, and a maximum gradient strength of 21 mT/m. A 256 x 256 matrix was used; 64% of the k-space lines were acquired, while

the rest were interpolated. The nominal resolution is $1.17 \times 1.17 \text{ mm}^2$. The total acquisition time was 1.2 s.

The image of Figure 4.6B was acquired with echo time 5.4 ms, repetition time 20 ms, and the same maximum gradient strength of 21 mT/m. In this case a 1024×1024 matrix was used, 64% of which was scanned. The nominal resolution is $0.29 \times 0.29 \text{ mm}^2$. The total acquisition time was 13.3 s.

References

1. Lauterbur P C (1973) Image formation by induced local interactions – examples employing nuclear magnetic resonance *Nature* **242** 190
2. Mansfield P and Grannell P K (1973) NMR diffraction in solids *J. Phys. C Solid State* **6** L422-L426
3. Callaghan P T (1991) *Principles of Magnetic Resonance Microscopy* Oxford: Clarendon
4. Ernst R R, Bodenhausen G, and Wokaun A (1987) *Principles of Nuclear Magnetic Resonance in One and Two Dimensions* Oxford: Clarendon
5. Cowan B (1997) *Nuclear Magnetic Resonance and Relaxation* Cambridge: Cambridge University
6. Jain A K (1989) *Fundamentals of Digital Image Processing* Englewood Cliffs: Prentice Hall
7. Han S-I (2001) *Correlation of Position and Motion by NMR: Pipe Flow, Falling Drop, and Salt Water Ice*, Ph.D. thesis, Aachen
8. Mansfield P and Morris P G (1982) *NMR Imaging in Biomedicine* New York: Academic
9. Louie A Y, Huber M M, Ahrens E T, Rothbacher U, Moats R, Jacobs R E, Fraser S E, and Meade T J (2000) In vivo visualization of gene expression using magnetic resonance imaging *Nat. Biotechnol.* **18** 321-325

10. Planinšič G, Stepišnik J, and Kos M (1994) Relaxation-time measurement and imaging in the Earth's magnetic field *J. Magn. Reson. A* **110** 170-174

Chapter 5. Liquid-State NMR and Scalar Couplings in Microtesla Magnetic Fields

A. Introduction

SQUIDs were first used in the 1980s to detect NMR signals in low magnetic field [1]. However, the majority of SQUID NMR studies have been performed on samples in the solid state, at liquid helium (LHe) temperatures. Recently, there has been increased interest in extending SQUID NMR techniques to samples in the liquid state, and in particular to systems which are biologically relevant. Kumar *et al.* [2] demonstrated NMR spectra from animal tissue measured at room temperature. Seton *et al.* [3] used SQUIDs to image room temperature samples in a field of 10 mT, and Schlenga *et al.* [4] used a SQUID magnetometer fabricated from the high transition temperature superconductor YBCO to image thermally polarized proton samples at room temperature in a field of 2 mT. Despite these early efforts, however, SQUID NMR studies of liquid samples remain extremely limited in number and in scope. The central challenge for SQUID NMR studies of liquids is that of low sensitivity. Thermal polarizations are two

orders of magnitude lower at 300 K than at 4.2 K. Moreover, in order to cool the SQUID below its superconducting transition temperature, it is necessary to thermally isolate the detector from the sample; filling factor is therefore quite low.

In the experiments described in this chapter, we employed a novel cryogenic insert which enabled us to achieve small separations between a sample maintained at room temperature and a SQUID detector operated in a liquid helium bath; the resulting high filling factor allowed us to measure NMR signals from samples in the liquid state using a low- T_c SQUID. Furthermore, we took advantage of the frequency-independent sensitivity of the untuned SQUID magnetometer to measure NMR signals from the sample in extremely low magnetic fields, of the order of 1 μ T, where the proton Larmor frequency is of the order of tens of Hz. At these fields, we achieved NMR linewidths approaching the lifetime limit even in grossly inhomogeneous measurement fields. The reduction of signal bandwidth led to an enhancement of both SNR and spectral resolution. While chemical shift information is lost in low field, scalar couplings, which are field-independent, are preserved. These scalar couplings act as signatures of specific covalent bonds. We have demonstrated a simple SQUID-based “bond detector”, which yields accurate information about heteronuclear scalar couplings in microtesla fields [5].

This chapter is organized as follows. I begin with a description of the cryogenic insert and the experimental apparatus. I describe conventional pulsed NMR experiments performed with this system; these involve resonant manipulation of spins in a relatively high field on the order of a few millitesla. Next I outline the concept of bandwidth narrowing through reduction of the strength of the measurement field, and demonstrate how, in the case of SQUID detection, this leads to an enhancement of both SNR and

spectral resolution. I then describe NMR experiments involving non-resonant spin manipulation with switched static fields, and signal detection in microtesla fields. Finally, I present the experimental results.

B. Experimental Apparatus

1) Cryogenic Insert

A diagram of the cryogenic insert is shown in Figure 5.1. The inner compartment of the insert, into which the sample was lowered, was 22 mm in diameter. This compartment was surrounded by a liquid nitrogen (LN_2) jacket with o.d. 100 mm to reduce the heat load of the insert on the LHe bath. At the 100-mm long tail section of the insert, however, the inner compartment looked out directly at the LHe bath. A single continuous vacuum jacket served to isolate the inner compartment of the insert from the LN_2 jacket (and from the LHe bath in the tail region), and to isolate the LN_2 jacket from the LHe bath; the walls of the vacuum space were silvered, with a slit running the length of the insert. The separation between the sample space and the LHe bath was 5 mm. The insert was surrounded by a number of styrofoam radiation baffles which were covered with aluminum foil; these extended laterally from the body of the insert to the neck of the LHe dewar, and served to reduce the heat load on the bath due to gaseous convection and direct radiation from the top of the dewar. To minimize the heat load due to thermal conduction of the Pyrex outer walls of the insert, the boiloff from the LHe bath was extracted from the brass top plate of the insert, so that the insert was cooled by the

evaporating helium gas. When the tail of the insert was not heated, the system consumed roughly 5 L of LHe per day.

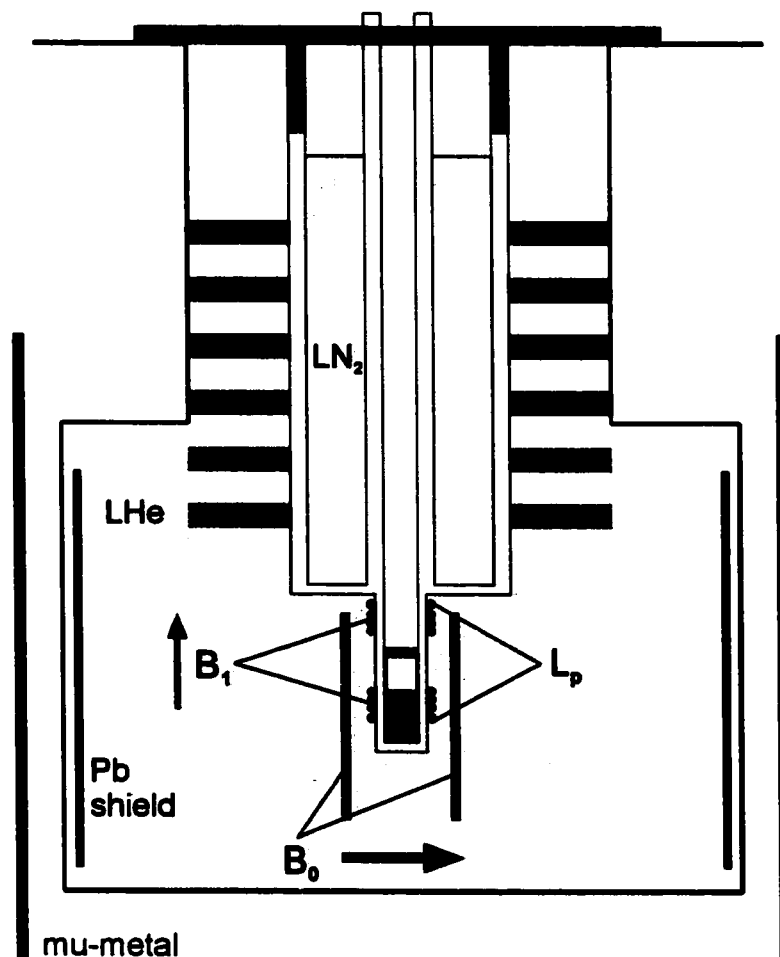


Figure 5.1. Schematic of cryogenic insert for SQUID-detected NMR spectroscopy of liquids. A cell containing the liquid sample was lowered into the tail section of the insert and was maintained at room temperature by a resistive heater. The pickup coil of the SQUID gradiometer, with inductance L_p , was wound on a G10 fiberglass form which fit snugly around the tail section of the insert. Coils to produce the static magnetic field B_0 and excitation pulses B_1 were also located in the helium bath. The belly of the dewar was lined with a superconducting Pb sheet and the dewar was surrounded by a single-layer mu-metal shield to attenuate the Earth's magnetic field and external magnetic disturbances.

A G10 fiberglass frame was suspended around the tail section of the insert using dental floss and BeCu springs. This frame supported the SQUID and SQUID pickup circuit, as well as magnetic field coils which were used to polarize and manipulate the nuclear spins.

2) SQUID Gradiometer and Readout

The dc SQUID used in our measurements was fabricated at the University of Giessen by Michael Mück using an all-liftoff Nb-AlO_x-Nb process. The SQUID parameters were as follows: $2I_c \sim 5 \mu\text{A}$, $R_n/2 \sim 10 \Omega$, and $L_s \sim 350 \text{ pH}$. The peak-to-peak modulation of the SQUID was roughly $40 \mu\text{V}$ when the SQUID was operated in a well-shielded environment. An 11-turn Nb input coil was integrated onto the SQUID washer.

The SQUID pickup circuit was configured as a first-order axial gradiometer with pickup loop diameter 38 mm and a baseline of roughly 80 mm, and was wound from 3 mil Nb wire on a G10 fiberglass form which fit around the tail of the cryogenic insert. For our NMR measurements at low frequency, we required an untuned, or superconducting, input circuit. Superconducting contacts from the Nb wire pickup coil to the on-chip integrated Nb input coil were made in the following manner.

The SQUID chip was glued to a printed circuit board, on which were patterned four Cu pads. Two of these pads were used to establish electrical contacts to the SQUID via Al bonding wire. The other two pads were coated with PbSn solder, which superconducts at 4.2 K. At one end of each of these pads, the Nb wire from the pickup coil was immersed in the solder blob. At the other end of the same solder blob, we immersed a piece of 2 mil Nb wire (roughly 5 mm in length) which had been softened by

annealing under vacuum (by passing 0.5 A rms through the wire for roughly 5 min). The free end of the annealed 2 mil Nb wire was then ultrasonically bonded to the Nb contact pad of the on-chip integrated input coil. The Nb wire – solder contacts appeared to form superconducting weak links with low critical current. These built-in “flux dams” opened when large magnetic fields were applied to manipulate the nuclear spins, preventing the flow of excessive currents in the input circuit which could drive flux into the SQUID washer or possibly damage the input coil. The pc board on which the SQUID was mounted and where the superconducting contacts were made was enclosed in a superconducting box machined from a solid piece of Pb and covered with a Pb sheet which was soldered tightly to the top of the box. The electrical leads to the SQUID and modulation coil and the twisted pair leads from the pickup coil passed through small holes which were drilled in the Pb box. In this way the SQUID chip and the stray inductance associated with the superconducting contacts in the input circuit were well-shielded from external magnetic flux.

A block diagram of the experiment is shown in Figure 5.2. The SQUID was operated in a flux-locked loop with modulation at 2 MHz; the small-signal bandwidth of the loop was around 700 kHz, and the slew rate greater than $10^6 \Phi_0/\text{s}$. During spin manipulations, the feedback loop was disabled by shorting out the capacitor across the integrator. The signal from the flux-locked loop passed through a sample-and-hold stage (to remove the arbitrary dc level at the loop output) and a set of analog filters before digitization. Signal averaging was performed in software.

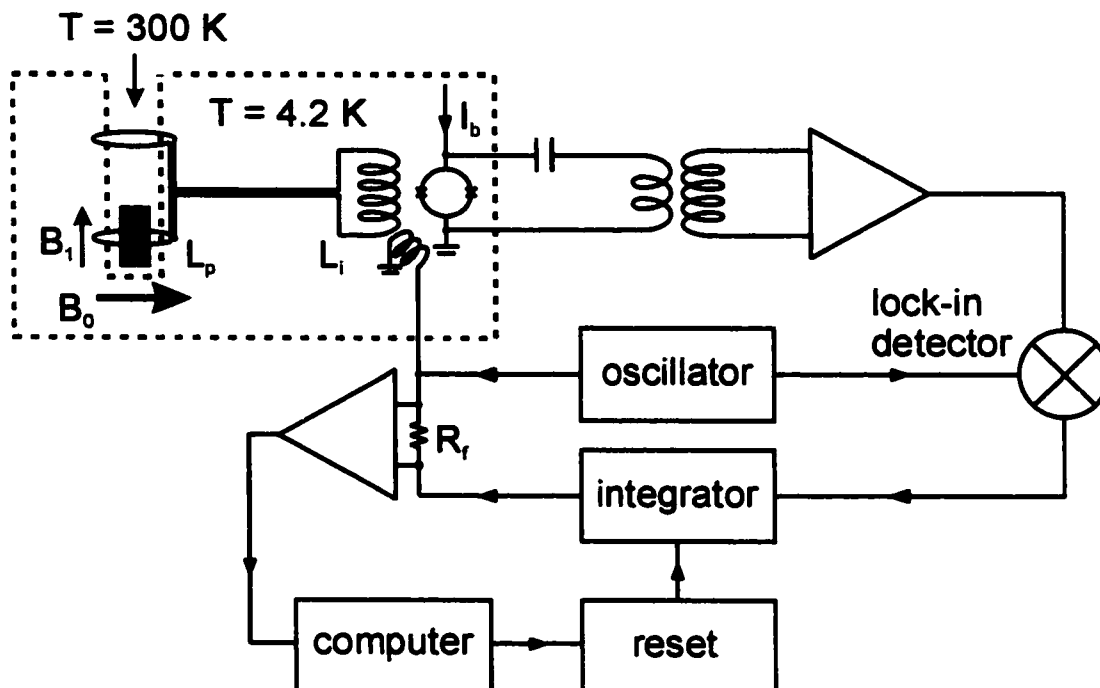


Figure 5.2. Block diagram of low- T_c SQUID spectrometer.

The belly of the LHe dewar was lined with a superconducting Pb sheet, and the dewar was surrounded by a single-layer mu-metal shield to attenuate the magnetic field of the Earth and external magnetic fluctuations. Experiments were carried out in a copper mesh Faraday cage to shield the SQUID from radiofrequency interference (see Section 6.E.2.b).

3) Static Field and Excitation Coils

In the case of an NMR experiment involving resonant spin manipulation (as described in Section 5.C), the static Zeeman field was provided by a pair of coils located in the LHe bath and oriented orthogonally to the detection direction. These coils each consisted of 67 turns of Cu-clad NbTi wire wound on a 90 mm diameter frame; the

separation of the coils was 55 mm. These coils provided roughly 1.2 mT per applied Ampere of current. Resonant pulses were provided by a pair of coils oriented along the detection direction and placed symmetrically with respect to the gradiometric pickup loops of the detector, in order to minimize the response of the SQUID to the excitation. Each coil consisted of 25 turns of insulated Nb wire wound on the 38-mm diameter frame on which the pickup coil was mounted. The excitation coils produced a field of roughly 830 μ T per applied Ampere. A photograph of the coil assembly is shown in Figure 5.3.



Figure 5.3. Magnetic field coil assembly. The coils whose windings are visible were used to provide the static Zeeman field for the NMR experiments (the diameter of the coil frame is 90 mm). The Nb wire excitation coils and the gradiometric pickup coil of the SQUID detector are wound on the cylindrical G10 fiberglass frame which surrounds the tail section of the insert, and are not visible in this photo. The Pb box at the bottom of the photograph contains the Nb-AlO_x-Nb SQUID. The entire assembly is suspended from the Pyrex cryogenic insert with dental floss and BeCu springs.

In the case of an NMR experiment involving non-resonant spin manipulation (as described in Section 5.E), the 67-turn coils located in the helium bath were used to provide a measurement field of the order of a few microtesla. The spins were

prepolarized along the detection direction in a field of a few millitesla; the polarizing field was provided by a one- or two-layer solenoid wound directly on the sample cell from Cu wire.

C. Conventional Pulsed NMR

The first NMR experiments performed with this system involved resonant manipulation of spins which were polarized in a static magnetic field. Mineral oil was chosen as the sample due to its relatively high proton density (roughly 100 Molar) and its relatively short spin-lattice relaxation time $T_1 \sim 30$ ms, which enabled rapid signal averaging. A Pyrex cell containing the sample was lowered into the tail section of the insert and heated to around 300 K using a resistive heater. A static magnetic field was applied in the horizontal direction using the 67-turn coils located in the LHe bath. Resonant pulses were produced by gating an HP 3314A function generator which was used to drive a homemade push-pull amplifier. A series capacitor was used to tune the excitation coil to the proton Larmor frequency.

Following the application of a resonant pulse, magnetic transients saturated our detector, giving a deadtime of order 1 ms. For this reason we employed a Hahn spin echo technique [6] (see Section 3.D) for our NMR measurements. Figure 5.4A shows the spin echo signal obtained from a 5 ml sample of mineral oil in a magnetic field of 1.8 mT; the trace is the average of 10,000 acquisitions. Figure 5.4B shows the NMR spectrum, obtained from the time trace by Fourier transform. The proton resonance appears at 77 kHz. The NMR line is rather broad - roughly 1 kHz - due to the fact that the Zeeman field is homogeneous to only about 10,000 ppm over the volume of the sample. Because the

signal is broadened over a relatively wide band, the SNR is rather poor; as a result, many averages are required to clearly resolve the proton resonance.

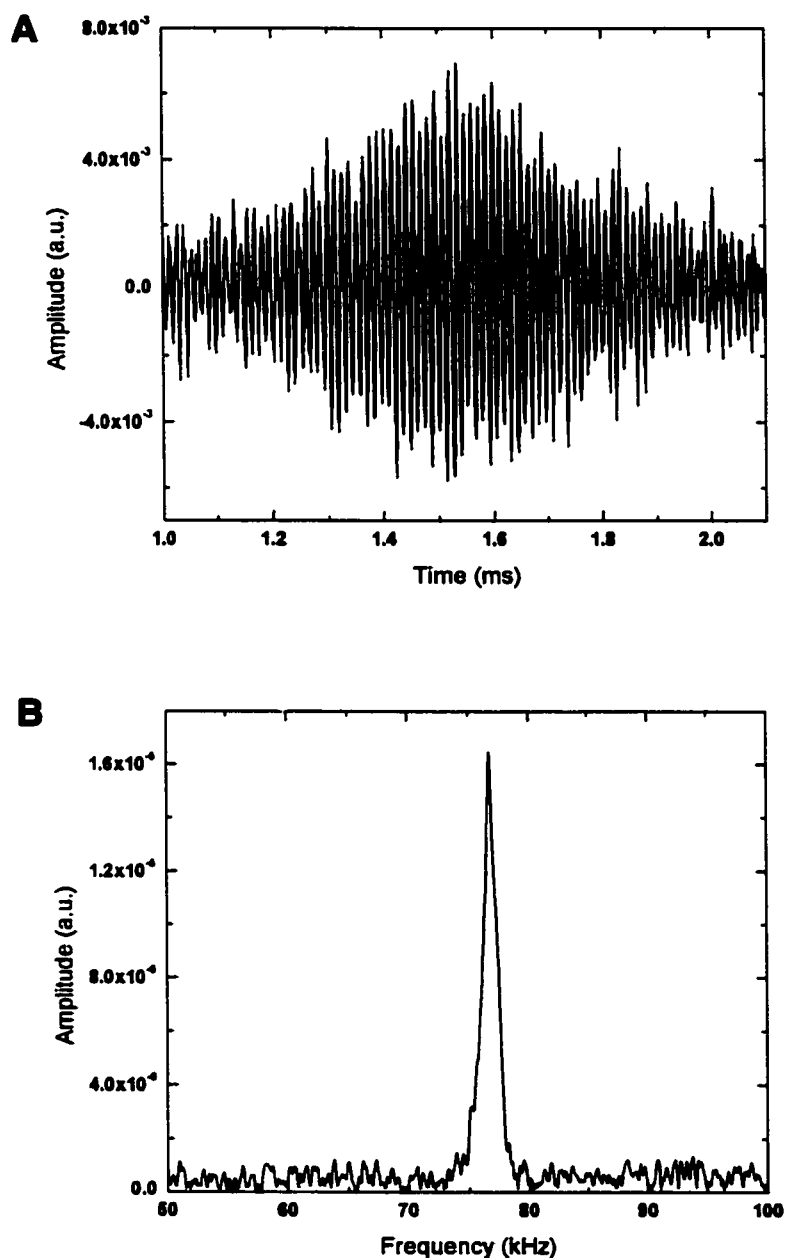


Figure 5.4. NMR signal from 5 ml of mineral oil measured in a field of 1.8 mT using a conventional Hahn spin echo sequence ($\pi/2$ - τ - π - τ -acq) involving resonant spin manipulation. The signal is the average of 10,000 transients. (A) Time trace. (B) NMR spectrum. The proton resonance appears at a frequency of 77 kHz. The NMR line is roughly 1 kHz wide, due to the fact that the static field is homogeneous to only 10,000 ppm over the volume of the sample.

D. Concept of Microtesla Field NMR

Line broadening due to field inhomogeneity is a major liability in liquid-state NMR. Spectral resolution, and therefore the information which one can extract about the interaction of nuclei with the local electromagnetic environment, is ultimately determined by the width of the NMR lines: it is necessary that the strength of the interactions exceed the dispersion of Larmor frequencies in the sample. Moreover, for a fixed sample magnetization, the SNR achieved from a single FID or spin echo signal scales inversely with the inhomogeneously broadened width of the NMR line. For these reasons, high-resolution liquid state NMR requires exquisite field homogeneity. In a conventional high-field spectrometer, homogeneity is attained by supplementing the magnet with sophisticated and costly shim coils. In a state-of-the-art high-field system, homogeneity of a few parts per billion is achieved.

An alternate approach is simply to reduce the strength of the measurement field. For a fixed relative field homogeneity, absolute homogeneity is enhanced by decreasing the strength of the measurement field. Of course, the sensitivity of a conventional NMR detector falls off rapidly as field strength is reduced. However, this is not the case for an untuned SQUID magnetometer, which is sensitive to magnetic flux, rather than the rate of change of magnetic flux. In the context of an NMR experiment, this means that, for a fixed sample magnetization, the integrated intensity of the NMR signal – the area under the NMR line – is independent of the frequency of the NMR signal. This fact makes it possible to perform the following unconventional NMR experiment.

A sample of nuclear spins is polarized in a magnetic field of the order of 1 mT. In addition to the polarizing field, a much smaller measurement field is applied in an

orthogonal direction. The polarizing field is then removed nonadiabatically, inducing precession in the much lower measurement field. In this experiment, the sample magnetization is fixed by the strength of the polarizing field. On the other hand, the width of the NMR line is determined by the absolute homogeneity of the measurement field. As the strength of the measurement field is reduced, the NMR line is compressed into a narrow band and the peak height grows, yielding an enhancement of both spectral resolution and SNR (Figure 5.5).

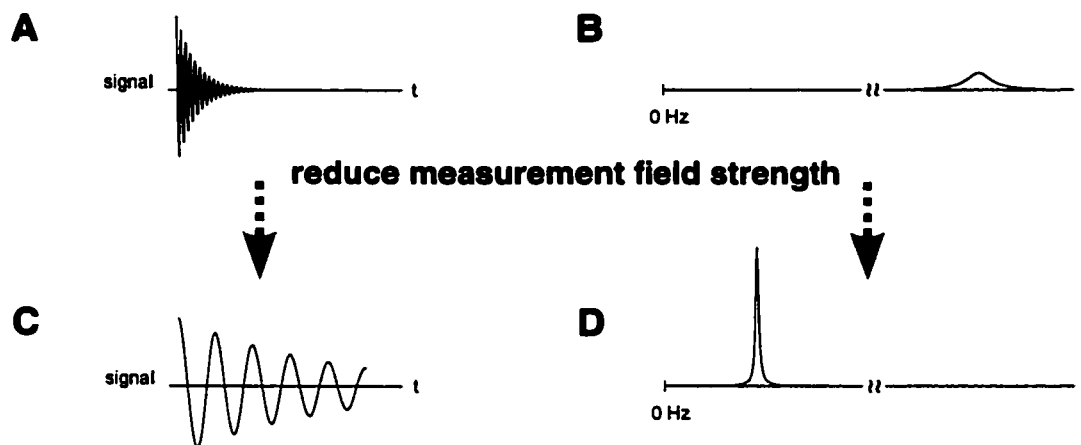


Figure 5.5. Narrowing of signal bandwidth through reduction of measurement field strength. (A) Time trace of NMR signal measured in a high inhomogeneous magnetic field. The dispersion of Larmor frequencies leads to rapid dephasing of the NMR signal. (B) The NMR spectrum corresponding to (A). (C) Time trace of NMR signal measured in a weak magnetic field with the same relative homogeneity as that in (A), using a detector whose sensitivity is independent of frequency. The NMR signal now appears at much lower frequencies. For a fixed sample magnetization, however, the amplitude of the NMR signal is unchanged. Moreover, the effective spin-spin relaxation time T_2^* is much longer, as the absolute homogeneity of the measurement field has been enhanced by reduction of the measurement field strength. (D) The NMR spectrum corresponding to (C). The integrated intensity of the NMR signal is conserved upon reduction of measurement field strength. Therefore, as the NMR signal is compressed into a narrow band, the peak height grows, leading to an enhancement of both SNR and spectral resolution.

E. Microtesla Field NMR: Experimental

In our experiments, the polarizing field was applied along the detection direction using a one- or two-layer solenoid of copper wire wound directly on the sample cell. Currents of order 1 A were used to generate fields of order 1 mT. The measurement field was supplied by the 67-turn coils located in the LHe bath. Rapid switching of the polarizing field was achieved by closing a HEXFET shunt to divert current from the

polarizing coil; a reed relay in series with the coil was then opened to prevent coupling of high frequency interference to the SQUID gradiometer via the polarizing coil. The sudden switching of the polarizing coil induced magnetic transients, apparently due to relaxation of paramagnetic impurities in the Pyrex of the cryogenic insert, which saturated the detector, giving a deadtime on the order of tens of milliseconds. Spin dephasing during this time resulted in signal loss which could be quite significant at higher measurement fields. For this reason we employed a spin echo to refocus the sample magnetization. The echo was formed by reversing the direction of the measurement field, and therefore the sense of precession of the nuclear spins.

The pulse sequence for microtesla field NMR is shown in Figure 5.6. The polarizing field of order 1 mT is applied for a time that is long compared to the spin-lattice time (T_1) of the sample. Following nonadiabatic removal of the polarizing field, the spins precess in the measurement field. As the spins precess, they lose phase coherence due to inhomogeneity of the measurement field. At a time τ following the removal of the polarizing field, the direction of the measurement field is inverted. Neglecting the effects of diffusion and in the absence of any background magnetic fields (fields generated by sources other than the current in the measurement coil), at each location in the sample, the spins see equal and opposite local magnetic fields before and following the inversion of the measurement field. Therefore the phase accumulated by each spin in the interval from $t = 0$ to $t = \tau$ is cancelled by the phase accumulated in the interval from $t = \tau$ to $t = 2\tau$. At the time $t = 2\tau$, phase coherence of the spins is restored, and the echo amplitude is maximum.

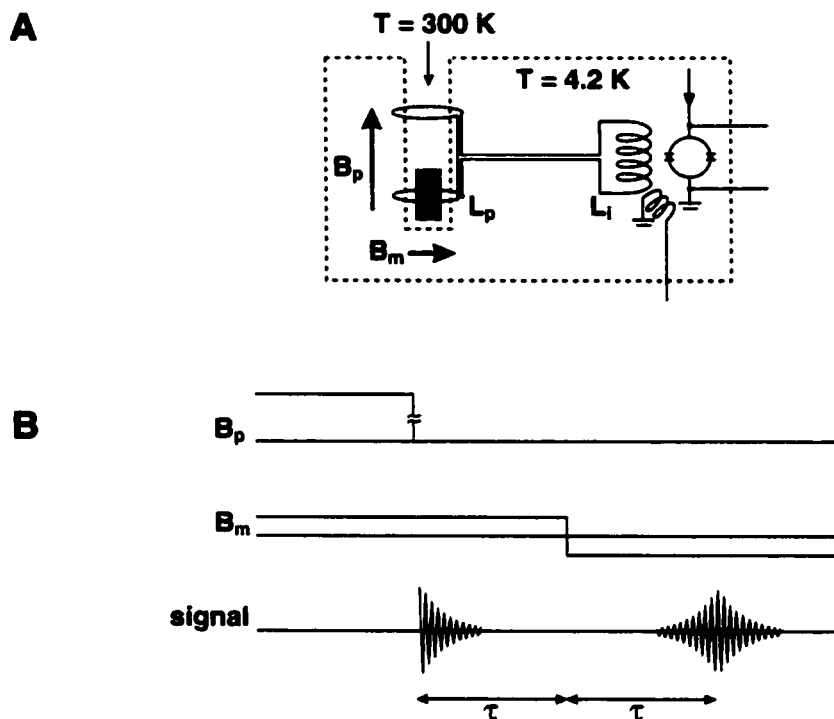


Figure 5.6. (A) Experimental configuration for microtesla field NMR. The polarizing field B_p is applied along the detection direction, using a solenoid wound directly on the sample cell. The much weaker measurement field B_m is applied in an orthogonal direction. (B) NMR pulse sequence. The spins are polarized for a time which is long compared to the spin-lattice relaxation time T_1 . Precession is initiated by nonadiabatic turnoff of the polarizing field. A spin echo is formed by reversing the direction of the measurement field, and therefore the sense of precession of the nuclear spins.

Figure 5.7 demonstrates the SNR enhancement achieved by reduction of the measurement field strength. The upper panel reproduces the proton spectrum from Figure 5.4B, acquired in a magnetic field of 1.8 mT with homogeneity of roughly 10,000 ppm. The lower panel shows the NMR signal from the same volume of mineral oil, measured in a field of 1.8 μ T using the sequence of Figure 5.6B. The sample was polarized in a field of around 2 mT; the measurement field was applied with the same magnet used to

acquire the spectrum in the upper panel. In this case, the proton resonance appears at 77 Hz. The sample magnetizations are the same in these two experiments; moreover, as the detector is untuned, the areas under the NMR lines are also the same. However, when the proton resonance was lowered from 77 kHz to 77 Hz, the NMR linewidth was compressed by a factor of 1000, and the peak height grew by the same factor. Reduction in the measurement field by a factor of 1000 therefore yielded an SNR enhancement of roughly 1000 – note that Figure 5.7A represents the average of only 10,000 transients, while Figure 5.7B was obtained from the average of 100 transients. In measurement fields of order 1 μ T, we achieved SNR of a few tens without signal averaging from samples with a volume of a few milliliters and a polarization of order 10^{-8} .

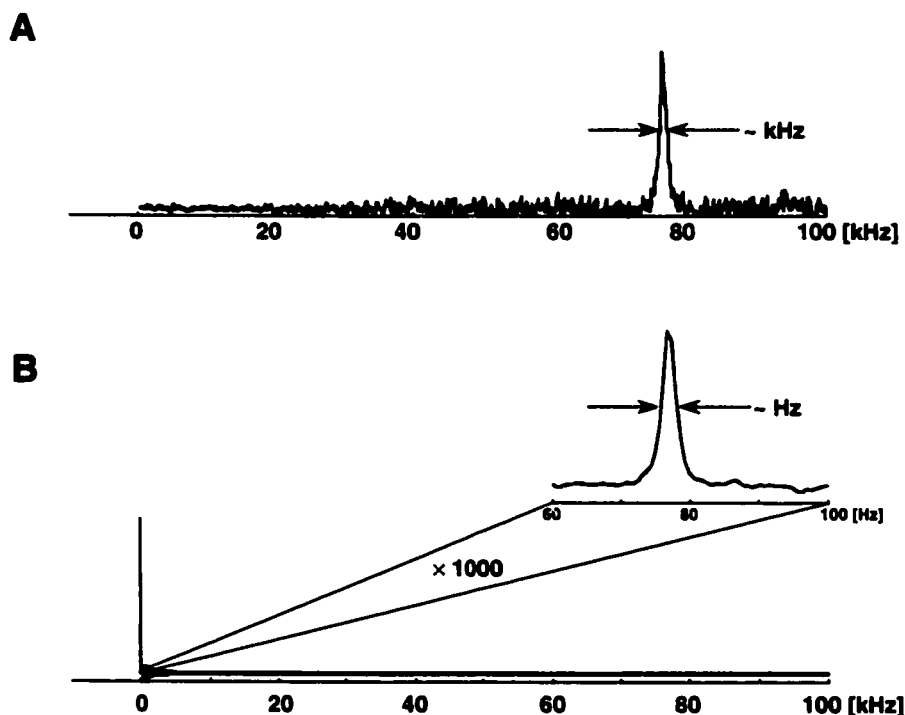


Figure 5.7. SNR enhancement through reduction of the strength of the measurement field. (A) NMR spectrum of 5 ml of mineral oil acquired in a static field of 1.8 mT using a conventional Hahn spin echo sequence ($\pi/2$ - τ - π - τ -acq) involving resonant spin manipulation. The spectrum is the average of 10,000 transients. (B) NMR sample of 5 ml of mineral oil measured in a field of 1.8 μ T using the sequence of Figure 5.6B. The sample was polarized in a field of around 2 mT; the measurement field was applied with the same magnet used in (A). The spectrum is the average of only 100 transients.

While there is no advantage in either resolution or SNR to be gained in reducing the measurement field past the point where the contribution of field inhomogeneity to the NMR linewidth becomes comparable to the natural linewidth, out of curiosity we attempted to push the proton Larmor frequency to the lowest possible value. We succeeded in measuring proton NMR signals at frequencies as low as 24 Hz (Figure 5.8). Ultimately, however, we were limited by the presence of residual magnetic fields in the

measurement region, due to imperfect screening of the Earth's field by the mu-metal shield surrounding the dewar or to flux trapped in nearby superconducting objects. If these residual fields exceeded the strength of the applied measurement field and if they were oriented along the polarization direction, then no precession would result following turnoff of the polarizing field. We could easily measure the component of the residual field along the direction of the measurement field by acquiring two proton spectra with equal and opposite currents applied to the measurement field coil. The difference in Larmor frequency corresponds to twice the projection of the residual field along the measurement field direction. Figure 5.9 shows the result of such an experiment, where we measured the projection of the residual field along the measurement field to be about 80 nT. The residual field seemed to change with each fill of the LHe cryostat, suggesting perhaps different patterns of magnetic flux trapped in the Pb shields of the system.

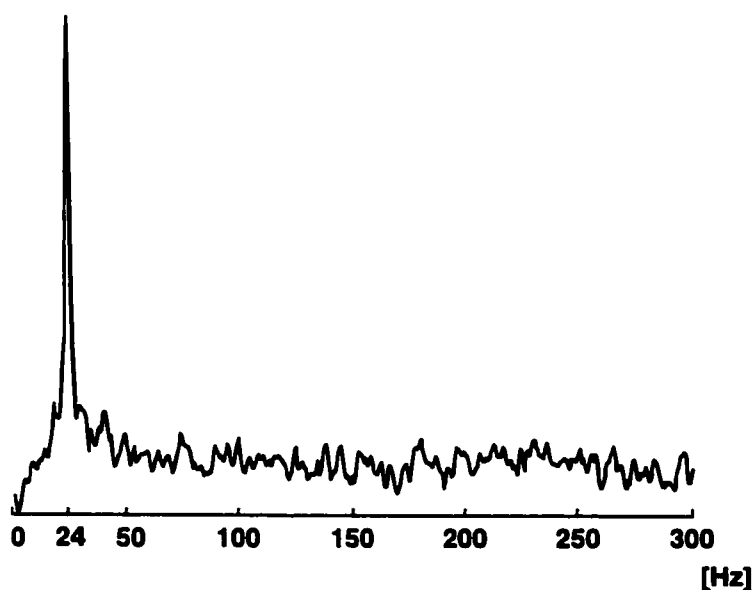


Figure 5.8. NMR signal from 5 ml of H_2O measured in a field of 570 nT. The spectrum is the average of 80 transients.

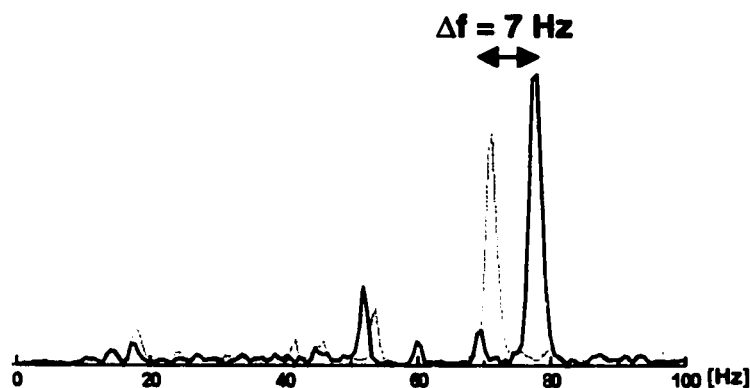


Figure 5.9. Two single shot proton spectra acquired with equal and opposite currents applied to the measurement field coil. The 7 Hz shift in Larmor frequency corresponds to a projection of the residual magnetic field along the measurement field direction of around 80 nT. The additional lines are due to environmental interference and mechanical resonances.

F. Multinuclear Studies

When the SQUID magnetometer is operated with an untuned input circuit, it detects broadband. Moreover, as the pulse sequence of Figure 5.6B involves switched static fields rather than resonant spin manipulation, excitation occurs over a broad band. Our experimental technique is therefore ideally suited to studies of systems containing nuclei with different magnetogyric ratios, resonating at different frequencies. Figure 5.10 demonstrates simultaneous SQUID detection of ^1H and ^{31}P resonances in a field of 2.6 μT .

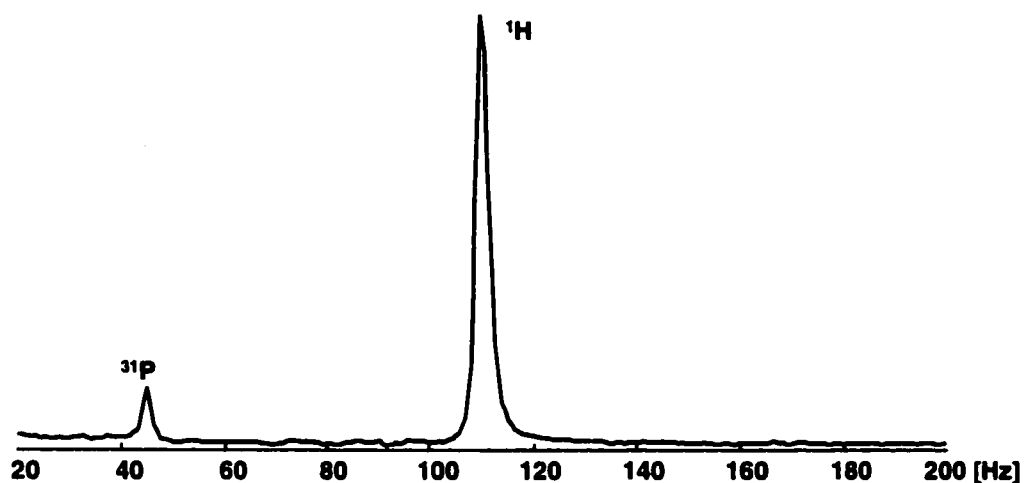


Figure 5.10. NMR spectrum of 5 ml of 85% phosphoric acid (H_3PO_4) measured in a field of $2.6 \mu\text{T}$. The spectrum is the average of 1000 transients. The magnetogyric ratios of the spin-1/2 nuclei ^1H and ^{31}P differ by a factor of 2.5. The proton resonance appears at 110 Hz; the ^{31}P resonance is clearly resolved at 44 Hz. The relative intensity of the two lines is determined by the different spin densities of the two nuclear species, as well as by the difference in thermal magnetizations brought about as a result of the difference in magnetogyric ratios.

G. Scalar couplings

While all chemical shift information is lost in low magnetic field, scalar couplings, which are field independent, are preserved. These scalar couplings act as signatures of specific covalent bonds. The enhanced resolution achieved by moving the resonance to low field makes it possible to accurately determine scalar coupling strengths, even in inhomogeneous measurement fields.

Figure 5.11A shows the NMR spectrum obtained from a mixture of methanol and phosphoric acid, measured in a field of $4.8 \mu\text{T}$. The proton spectrum consists of a sharp singlet at 205 Hz. However, when the methanol and phosphoric acid are allowed to react to form the ester trimethyl phosphate, scalar coupling to the ^{31}P nucleus causes the proton

resonance to split into a doublet, with a coupling strength $J_3[\text{P,H}] = 10.4 \pm 0.6$ Hz which is characteristic of this particular next-next-nearest neighbor interaction (Figure 5.11B). The proton doublet is easily resolved in a field of $4.8 \mu\text{T}$, despite a relative field homogeneity of roughly 10,000 ppm over the sample volume.

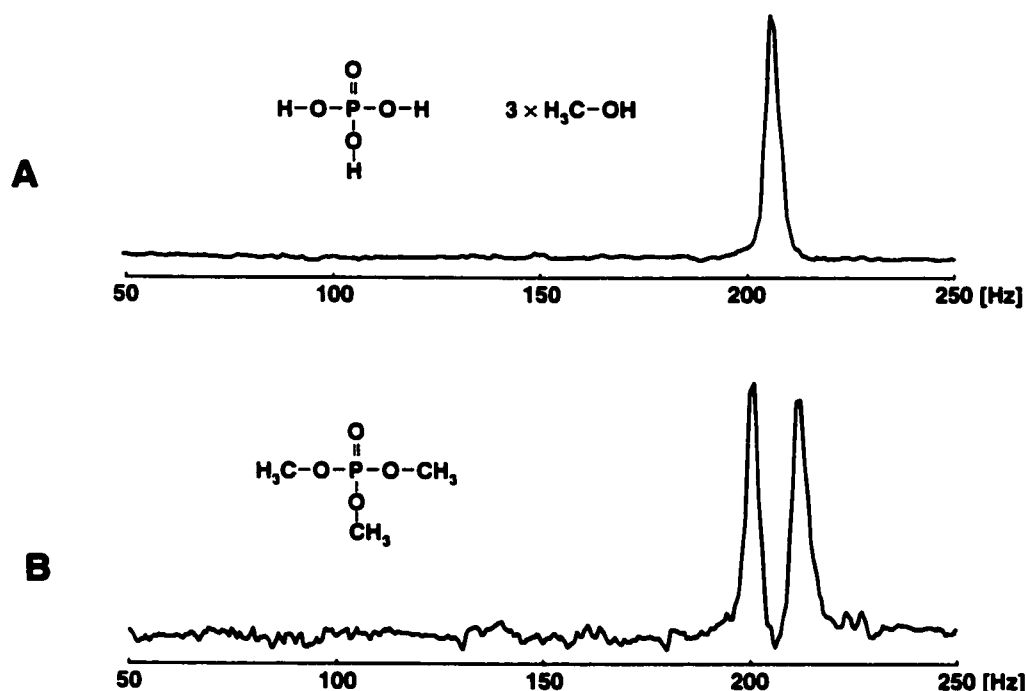


Figure 5.11. Resolution of scalar couplings in microtesla fields. (A) NMR spectrum of 5 ml of 3 parts methanol, 1 part phosphoric acid (85% in water) measured in a field of $4.8 \mu\text{T}$. The spectrum is the average of 100 transients. Rapid spin exchange with the protons in water obscures the proton-phosphorous scalar coupling in phosphoric acid, and the proton spectrum consists of a sharp singlet. (B) NMR spectrum of 3 ml of neat trimethyl phosphate (Sigma-Aldrich) measured in a field of $4.8 \mu\text{T}$. The spectrum is the average of 100 transients. Electron-mediated scalar coupling of the nine equivalent protons to the ^{31}P nucleus splits the proton resonance into a doublet, with a splitting that is determined by the coupling strength J . For this particular coupling via three covalent bonds, $J_3[\text{P,H}] = 10.4 \pm 0.6$ Hz. Scalar coupling to the nine equivalent protons splits the ^{31}P resonance into ten lines; these are below the noise level.

Because electron-mediated scalar couplings between nuclear spins act as signatures of specific covalent bonds, the techniques outlined here could form the basis of a simple low-field NMR “bond detector”, insensitive to chemical shifts, but yielding accurate information about scalar couplings. Such a detector could be applied to the study of analytes, chemical reactions, and molecular conformations. For example, the dispersion of J-values for sp^3 1H - ^{13}C bonds is approximately 10 times greater than the NMR linewidths achieved in our experiments (see Table 3.1). If the values of J-couplings are known, then pure J-spectra could allow one to assign a number of molecular groups. Considering the highly developed techniques for isotopic labeling in biomolecular NMR, the use of such a method for following a “spy nucleus” through bond formation is an appealing possibility. The proton spectrum of Figure 5.12 represents a first step in this direction. The spectrum was obtained from 5 ml of carbonyl labeled glycine (see figure inset) in D_2O in a field of 3.7 μT . The resonance of the two equivalent α -protons is split into a doublet due to scalar coupling to the ^{13}C nucleus. The coupling strength was determined from the lineshape of the doublet to be $J_2[C,H] = 5 \pm 1$ Hz.

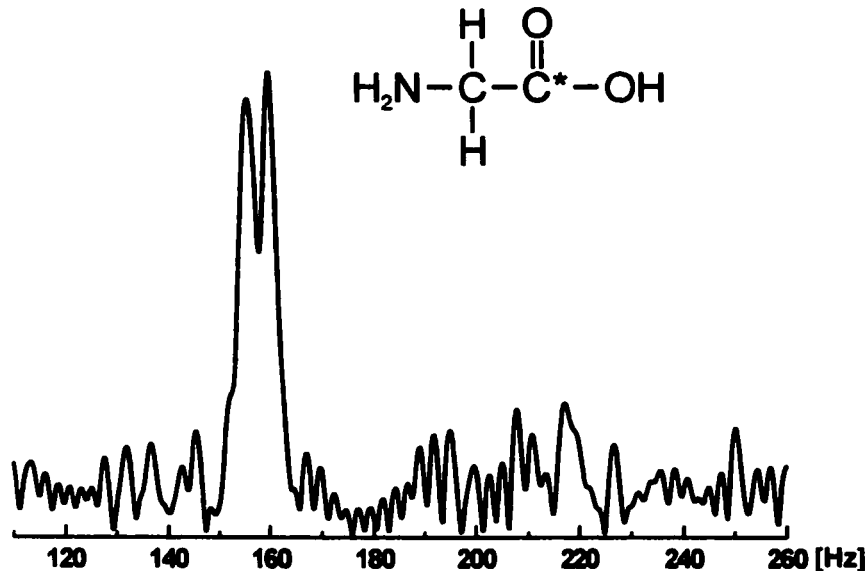


Figure 5.12. NMR spectrum of 5 ml solution of carbonyl labeled glycine in D_2O , measured in a field of $3.7 \mu\text{T}$. The spectrum is the average of 5525 transients. The resonance of the two equivalent α -protons (those bonded directly to the unlabeled carbon) is split into a doublet due to scalar coupling to the ^{13}C nucleus, with a coupling strength $J_2[\text{C},\text{H}] = 5 \pm 1 \text{ Hz}$. The line from the additional uncoupled protons is not resolved, as these spins have a relatively short T_2 , and the experiment was performed with a relatively long echo time of 167 ms.

References

1. Greenberg Ya S (1998) Application of superconducting quantum interference devices to nuclear magnetic resonance *Rev. Mod. Phys.* **70** 175-222
2. Kumar S, Thorson B D, and Avrin W F (1995) Broadband SQUID NMR with room temperature samples *J. Magn. Reson. B* **107** 252
3. Seton H C, Hutchison J M S, and Bussel D M (1997) A 4.2-K receiver coil and SQUID amplifier used to improve the SNR of low field magnetic resonance images of the human arm *Meas. Sci. Technol.* **8** 198-207

4. Schlenga K, McDermott R, Clarke J, de Souza RE, Wong-Foy A, and Pines A (1999)
Low-field magnetic resonance imaging with a high- T_c dc superconducting quantum
interference device *Appl. Phys. Lett.* **75** 3695-3697
5. McDermott R, Trabesinger A H, Mück M, Hahn E L, Pines A, and Clarke J (2002)
Liquid-state NMR and scalar couplings in microtesla magnetic fields *Science* **295**
2247-2249
6. Hahn E L (1950) Spin echoes *Phys. Rev.* **80** 580-594

Chapter 6. SQUID-Detected MRI in Microtesla Fields

A. Introduction

Since the invention of MRI in the early 1970s, MRI scanners have steadily developed towards higher magnetic field strengths. The enhanced sensitivity attainable at high field makes it possible to resolve features at ever shorter length scales, and enables fast imaging experiments with close to real-time resolution. State-of-the-art clinical scanners operate at a field strength of 1.5 T, corresponding to a proton Larmor frequency of 64 MHz; currently, there is a drive to gain approval for 4 T imagers for clinical use. A number of facilities around the world now have 7 T scanners for research purposes.

At the same time, the last three decades have seen continued effort toward the development of systems for MRI in low magnetic field. Much of this work has been motivated by considerations of cost: a commercial full-body imager operating at 1.5 T costs several million dollars, and the operation of such a machine places considerable demands on the infrastructure of the hospital or research facility. In addition, due to the size and complexity of the high-field system, it must necessarily remain fixed in one

location, and the sample or subject must be transported to the system and inserted into the confining bore of the high field magnet; in certain cases this is simply not possible. The idea of a low-cost, portable MRI scanner is extremely appealing, as is the notion of an open MRI system, which, for example, would enable acquisition of MRIs at the same time that a medical procedure is performed. Inexpensive, portable imagers would enable MRI to address a wide variety of new problems, potentially transforming it from a highly specialized clinical and research technique to a much more widespread, flexible tool for rapid patient screening and general noninvasive imaging. And any sort of portable or open MRI system would need to operate at relatively low magnetic field strengths.

Moreover, despite the serious disadvantage of reduced sensitivity, the images acquired in low field should, in principle, be of higher quality than those acquired in high magnetic field. An inevitable drawback of high-field imaging is that of susceptibility artifacts. When a heterogeneous sample is placed in a magnetic field, variations in magnetic susceptibility over the sample volume give rise to spurious magnetic field gradients. When these spurious gradients become comparable to the gradients which are used for encoding, the image is severely distorted. In medical imaging, the presence of dental fillings or jewelry is enough to destroy the MRI; abrupt changes in susceptibility at solid-liquid and solid-air interfaces inside the body, such as those which occur in sinuses, produce distortions which are more subtle, but which nevertheless place strict limits on the achievable spatial resolution. Since the strength of the spurious gradients scales linearly with the strength of the applied field, it is possible to eliminate susceptibility-induced distortions entirely by imaging in low magnetic field [1].

Finally, as discussed in Section 4.D, T_1 contrast in tissue is enhanced in low magnetic field [2-4]. Because of this, low-field images allow sharper differentiation of different organs and tissue types, and potentially contain richer information than the corresponding images acquired in high field. (In this connection it is interesting to note that, in the early days of MRI, many researchers were skeptical that high-field MRI would ever amount to a useful clinical tool, precisely because of the degradation of tissue contrast in high field).

There have been a number approaches to low-field MRI in recent years. These have generally relied on Faraday detection in a static field of order 10 mT to 100 mT, which is generated by an electromagnet [5]. The main obstacle in these studies is the low sensitivity intrinsic to the low field experiment. In a different approach, Seton *et al.* employed a tuned SQUID magnetometer for NMR detection; the SQUID provided an SNR enhancement of a factor of 2.8 – 4.5 over conventional detection in images acquired from room temperature samples in a field of 10 mT [6]. In the low-field imaging work of Macovski *et al.*, spins were prepolarized in a field of 0.3 T, while the NMR signals were detected in a much lower field of 30 mT [7-8]. Here, the homogeneity of the polarizing field was not crucial, and the prepolarization step led to an enhancement of sample magnetization by an order of magnitude. Using similar techniques, Stepišnik *et al.* acquired MRIs in the magnetic field of the Earth ($B_{\text{Earth}} \sim 50 \mu\text{T}$), in the process elegantly demonstrating the enhanced T_1 contrast attainable in low-field [2, 4]. In both the works of Macovski *et al.* and Stepišnik *et al.*, however, Faraday detection in the field of the Earth entailed substantial signal loss.

In this chapter, I describe a new approach to magnetic resonance imaging in low magnetic field. The experiments are based on the ideas which were presented in the preceding chapter: by exploiting the frequency-independent response of the untuned SQUID magnetometer, it is possible to enhance both the SNR and resolution (in this case, spatial resolution) of magnetic resonance images by reducing the strength of the measurement field to eliminate inhomogeneous broadening of the NMR lines.

The chapter is organized as follows. First I describe the concept behind SQUID-detected MRI in microtesla fields, and demonstrate how the reduction in the strength of the measurement field leads to an enhancement of SNR and spatial resolution. Then I describe the experimental setup, with particular emphasis on the details of the SQUID detector and the challenges of operating the system in an unshielded environment. Next I discuss the NMR and MRI experiments performed with this system, and present preliminary magnetic resonance images acquired in microtesla fields. In the final part of the chapter I examine the various sources which contribute to the magnetic field noise of the system, and suggest means for further reducing the system noise.

B. Concept of Microtesla Field MRI

There is an intimate connection between the inhomogeneously broadened width of the NMR line and the spatial resolution which can be achieved in an MRI experiment. We explore this connection by considering the simple case of frequency encoding in one dimension (Figure 6.1). We imagine an MRI phantom consisting of two small compartments containing nuclear spins which are separated by some distance along the z-axis. The phantom is placed in a nominally homogeneous magnetic field $\mathbf{B} = B_0 \hat{\mathbf{k}}$. If,

however, there are spurious magnetic field gradients (in particular, off-diagonal gradient components G_x and G_y), the NMR line acquired from this sample will have a width which is determined by the absolute strength of the spurious gradients. When one now applies the encoding gradient G_z in order to perform a one dimensional MRI projection along the z axis, the initial width of the NMR line determines the strength of the gradient which must be applied in order to separate out the contributions from the two spatially distinct parts of the phantom to the NMR spectrum. It can be seen that the spatial resolution Δz which is attainable in such an experiment is determined from the relation

$$\Delta z = 2\pi\Delta f/\gamma G_z, \quad (6.1)$$

where Δf is the width of the NMR line without applied gradients.

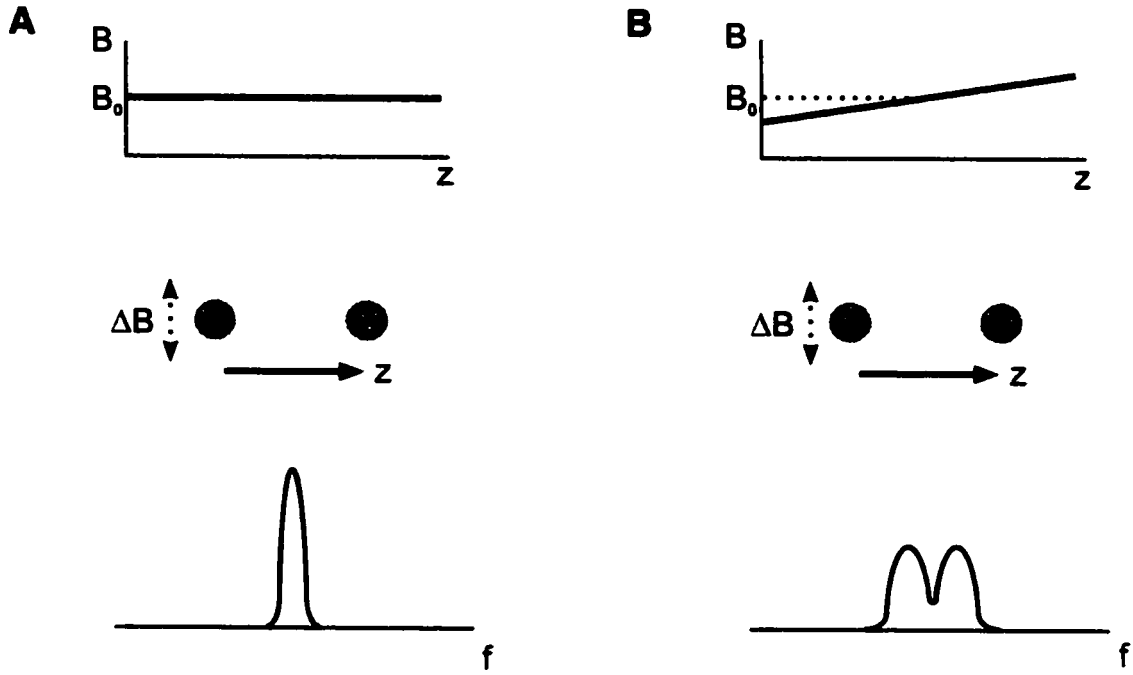


Figure 6.1. NMR linewidth and spatial resolution. (A) Sample consisting of two distinct regions of nuclear spins (indicated as grey circles in the center panel) immersed in a nominally homogeneous magnetic field. A spurious magnetic field gradient causes inhomogeneous broadening of the NMR line from the sample. (B) As in (A), but now a magnetic field gradient G_z is applied in order to perform a one-dimensional MRI projection. The broader the NMR line initially [lower panel of (A)], the stronger the magnetic field gradient which must be applied in order to separate out the contributions to the NMR spectrum from the two spatially distinct regions of the sample [lower panel of (B)]. Conversely, for a fixed magnetic field gradient strength, the narrower the initial width of NMR line, the higher the spatial resolution in the MRI experiment.

The above relation also holds in the case of phase encoding. Here, the difference in phase $\Delta\theta = \gamma G_z \tau \Delta z$ acquired by nuclear spins separated by a distance Δz due to a gradient G_z applied during an interval τ must be greater than the spurious phase difference $2\pi\Delta f\tau$ which is accumulated due to field inhomogeneities in order for it to be possible to resolve spatial features at the level of Δz .

We note that the important quantity here is the NMR linewidth, which is determined by the absolute homogeneity of the measurement field, rather than the relative homogeneity. As was discussed in the proceeding chapter, absolute field homogeneity is conveniently enhanced by reducing the strength of the measurement field. In the case of NMR detection with an untuned SQUID magnetometer, the reduction in measurement field entails no signal loss provided that the sample magnetization is fixed, for example by prepolarization in a higher field. The idea for SQUID-detected MRI in microtesla fields is then as follows (Figure 6.2). The sample of nuclear spins is polarized in field of order tens of mT, corresponding to a polarization of around 10^{-7} . However, instead of detecting the NMR signal in high field, where it is quite challenging to achieve narrow NMR lines, one measures the NMR signal in an extremely low magnetic field, where it is possible to approach the lifetime limit even for grossly inhomogeneous measurement fields. Now it is necessary to apply only modest magnetic field gradients to perform the encoding. As a result, the NMR signal is dispersed over only a narrow band. The NMR transients are therefore detected with a high SNR, and the time required to acquire the image is relatively short.

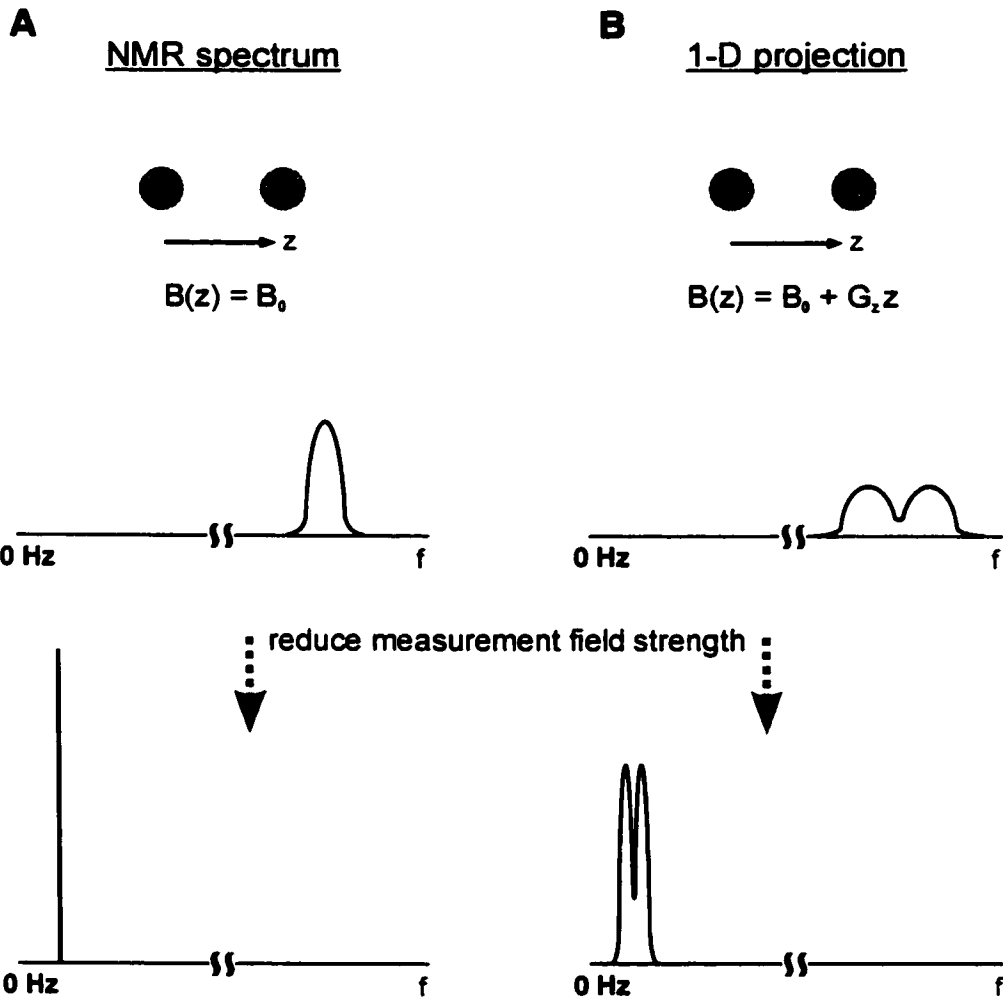


Figure 6.2. MRI in microtesla magnetic fields. (A) NMR spectra acquired from a sample consisting of two separate regions containing nuclear spins which is immersed in a magnetic field which is nominally homogeneous, but which involves spurious gradients which give rise to inhomogeneous broadening of the NMR lines. (Center panel) At high measurement field strengths, the absolute homogeneity of the field is relatively poor, and the NMR line is relatively broad. (Lower panel) As the strength of the measurement field is reduced, the absolute homogeneity of the field is enhanced, and the NMR line is narrowed. In the case of fixed sample magnetization and detection with an untuned SQUID magnetometer, the reduction of measurement field strength also leads to an enhancement of SNR. (B) As in (A), but now a magnetic field gradient G_z is applied in order to perform a one-dimensional MRI projection. (Center panel) At relatively high measurement field strengths, relatively strong gradients are needed in order to clearly resolve the two spatially distinct regions of the sample. As a result, the NMR signal is dispersed over a large band, and SNR is poor. (Lower panel) At low measurement field strengths, inhomogeneous broadening of the NMR lines is largely eliminated. As a result, only modest magnetic field gradients are needed to resolve the two spatially distinct regions of the sample. Therefore, the NMR signal remains confined to a relatively narrow band, and SNR is relatively high.

As a final remark, we note that even in the absence of homogeneous and inhomogeneous line broadening (infinite T_2 and perfect field homogeneity), MRI resolution is ultimately limited by spin diffusion which occurs during the encoding intervals. For example, over an encoding period of $\tau = 100$ ms, a proton in water will diffuse over a length $(D\tau)^{1/2} \sim 10$ μm , where $D = 2 \times 10^{-9} \text{ m}^2\text{s}^{-1}$ is the constant of self diffusion of H_2O . In this work we are concerned with imaging at the mm length scale; therefore, spin diffusion does not present a problem. Of course the effects of diffusion can be overcome by limiting the length of the encoding intervals, and increasing the strength of the applied gradients. This is the approach taken in several recent attempts at MRI microscopy, as in [9], where gradients of order 1 - 10 T/m were applied in pulses with duration of order 1 ms.

C. Experimental Apparatus: Magnetic Field and Gradient Coils

As our goal was to perform MRI experiments in extremely low magnetic field, a convenient starting point was a zero magnetic field region. In our experiments we used a set of three orthogonal cancellation coils to zero out the field of the Earth over the measurement region. These coils were wound on the six faces of a cube which measured roughly 2 m on a side. Braces which were integrated into the structure of the cube supported a coil assembly which consisted of: (1) a Helmholtz pair, used to produce a measurement field in the range of μT to tens of μT ; (2) a Maxwell pair [10], used to generate the diagonal component $G_z \equiv dB_z/dz$ of the magnetic field gradient tensor; and (3,4) two sets of saddle coils wound in the Golay geometry [10], used to generate the off-diagonal components $G_x \equiv dB_z/dx$ and $G_y \equiv dB_z/dy$ of the gradient tensor. In addition,

these braces supported a G10 fiberglass LHe dewar which housed the SQUID sensors.

All support structures and coil forms were made from wood, which in many ways was an ideal material for this experiment: wood is non-magnetic, and therefore does not give rise to magnetic field gradients which would interfere with the evolution of nuclear spins; it is non-conducting, and therefore does not generate thermal magnetic field noise or eddy currents which might degrade the balance of a SQUID gradiometer; moreover, wood is inexpensive and an excellent building material. The dimensions of the system were chosen with an eye to the eventual imaging of human subjects: an average-sized adult can fit (not too uncomfortably) into the measurement region at the center of the cube.

A schematic of the coil system is shown in Figure 6.3. Note that, following the usual convention in the magnetic resonance community, we take the z axis to lie along the measurement field direction; the x axis is chosen to coincide with the vertical direction (the detection direction). A photograph of the SQUID imaging system is shown in Figure 6.4.

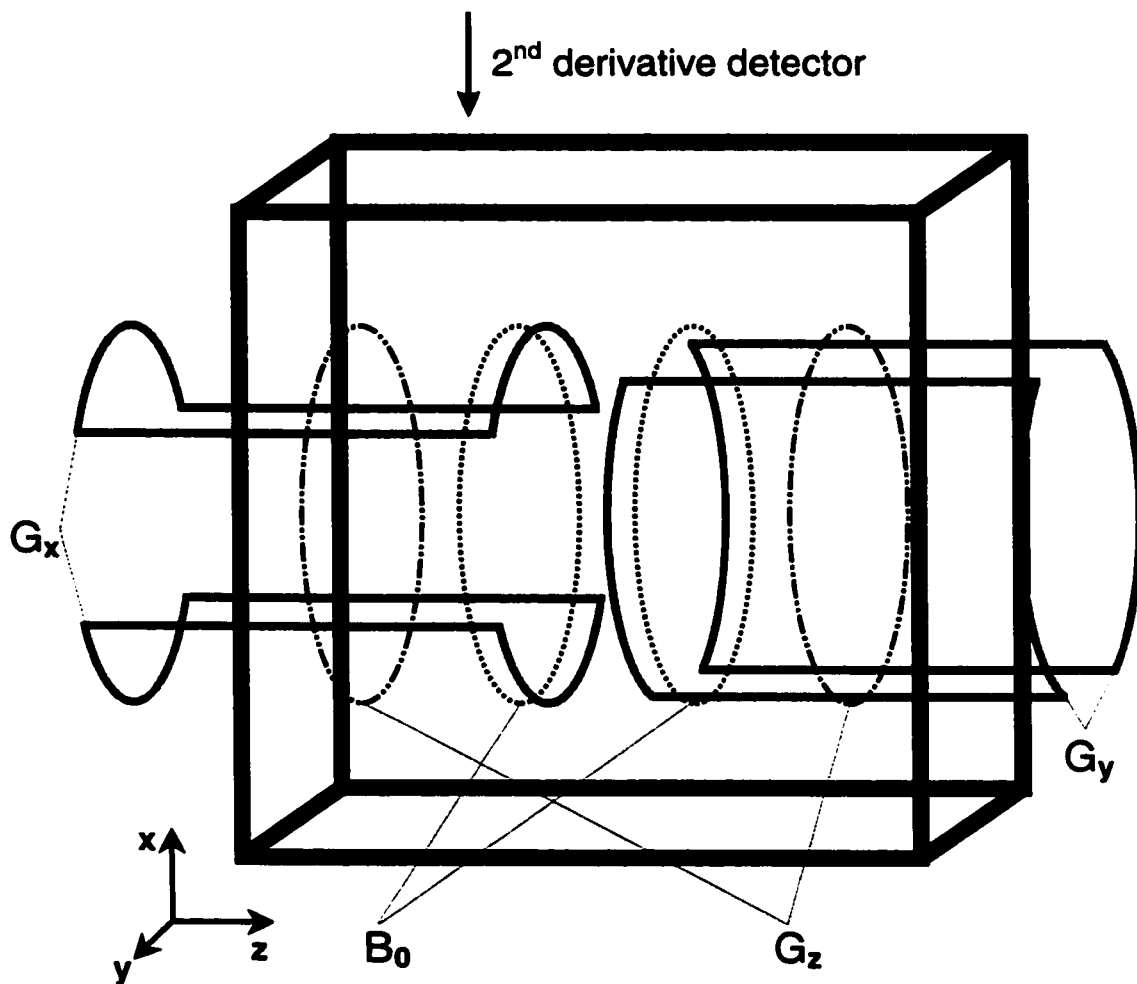


Figure 6.3. Magnetic field and magnetic field gradient coils for SQUID-detected MRI. Six 100-turn coils wound on each face of a cube, 2 m on a side, were used to cancel the magnetic field of the Earth. The measurement field B_0 was produced by a Helmholtz pair arranged in the center of the cube. The diagonal component G_z of the first-order magnetic field gradient tensor was produced by a Maxwell pair; the off-diagonal gradients G_x and G_y were produced by saddle coils wound in the Golay geometry (for each set of Golay coils, only two of the four saddle coils are shown above). The detector was a second-order axial SQUID gradiometer oriented in the vertical (x) direction, and which was housed in a LHe dewar suspended in the center of the cube.

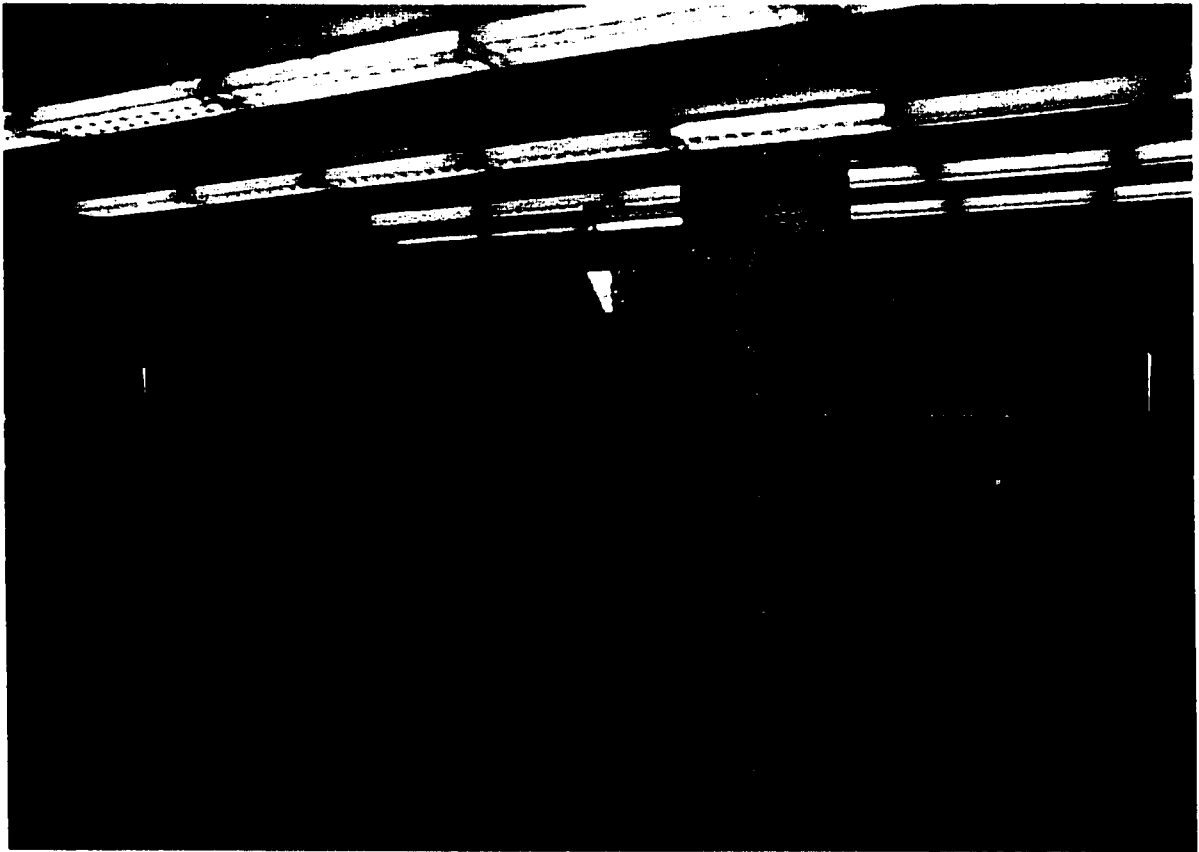


Figure 6.4. Photograph of SQUID MRI system.

Cancellation Coils

Each of the six cancellation coils consisted of 100 turns of 18 gauge copper wire wound in a groove cut along the outer edge of a wooden frame which made up one of the six faces of the cube. The coils on opposite faces of the cube were wired in series. Each pair had a resistance of roughly $30\ \Omega$, and generated a magnetic field change of around $50\ \mu\text{T}$ per applied Ampere, so that only fractions of Amperes and modest voltages were required to cancel the three components of Earth's field. Heating in the cancellation coils was negligible. (For the record, a total of about 2.7 miles of 18 gauge Cu wire – approximately 60 lbs – went into the cancellation coils).

Measurement Field and Gradient Coils

The measurement field was produced by a Helmholtz pair with radius 0.6 m arranged in the center of the cube. Each coil consisted of 20 turns of 18 gauge copper wire. The diagonal component G_z of the gradient tensor was generated by a Maxwell pair with radius 0.6 m mounted outside the measurement field coils. Each coil consisted of 20 turns of 18 gauge wire. The off-diagonal gradients G_x and G_y were generated by saddle coils wound in the Golay geometry from 20 turns of 22 gauge wire; the radius of curvature of the Golay coils was 0.6 m. All of these coils were wound in grooves which were cut along the outer edges of circular pieces of $\frac{3}{4}$ " birch plywood. Per Ampere of applied current, these coils generated: 1) $B_0 = 30 \mu\text{T}$; 2) $G_z = 50 \mu\text{T/m}$; and 3) $G_x = G_y = 50 \mu\text{T/m}$.

Polarizing Coil

In order to enhance the sample magnetization, the spins were prepolarized in a magnetic field of the order of tens of millitesla. Precession was induced either by non-adiabatic turnoff of the polarizing field (in which case the spins were polarized in a direction orthogonal to the measurement field), or by adiabatic turnoff of the polarizing field followed by resonant excitation in the much lower measurement field (in which case the spins were typically polarized along the measurement field direction). In the first instance, the polarizing field had to be switched in a time which was short compared to the Larmor period in the measurement field (see Section 3.F); in the second instance, the switching requirements were less strict: turnoff of the polarizing field needed to occur

simply in a time which was short compared to the spin-lattice relaxation time T_1 . In either case, the requirement of rapid field switching, coupled with practical limits to the level of Joule heating which could be tolerated in the magnet wire, governed the design of the polarizing coil.

Given a certain amount of space available for magnet windings, the maximum field produced by the magnet at a fixed level of Joule heating is independent of the gauge of wire used to fill the space (provided one neglects the fact that there will be larger gaps between windings if one uses larger gauge wire). On the other hand, the time it takes to switch the polarizing field will go more or less linearly as the self inductance of the coil, which scales as the square of the number of turns. Therefore, for rapid switching it is advantageous to use relatively heavy gauge wire and a relatively small number of turns.

Our polarizing magnet consisted of two poles wound from 18 gauge copper wire on G10 fiberglass frames. On each pole, the magnet windings filled a 17 mm wide channel, with a 15 mm radius for the inner windings and a 70 mm radius for the outer windings. The separation of the two magnet poles was roughly 100 mm. A total of 510 turns was used for each magnet pole. The field at the center of the coils was approximately 4 mT per applied Ampere; the total resistance of the magnet pair was approximately 6 Ω , while the inductance was roughly 100 mH. The heavy formvar insulation of the magnet wire seemed to tolerate Joule heating at a level of 100 W per magnet pole (10 A applied at a 30% duty cycle, corresponding to a polarizing field of 40 mT). To achieve higher polarizing fields, however, it would be necessary to implement water cooling of the magnet. While the homogeneity of the polarizing field was quite poor, this of course had no effect on NMR linewidth or SNR.

The condition for nonadiabatic turnoff of the polarizing field can be written as follows:

$$\frac{dB}{dt} \gg B\omega = \gamma B^2, \quad (6.2)$$

where B is the instantaneous strength of the magnetic field. For measurement fields in the microtesla range, it is trivial to meet the nonadiabatic switching condition, as the term on the right hand side of (6.2) becomes extremely small as the strength of the measurement field is reduced. Indeed, in our experiments, it was sufficient to drive the polarizing coil with a shaped voltage pulse from a Techron 7700 amplifier. At the turnoff of the pulse, the coil would discharge with an L/R time governed by the the self-inductance of the coil (again, around 100 mH) and the output impedance of the amplifier (a few tens of ohms). Driving the polarizing coil in this “controlled voltage” mode had the advantage that, following the turnoff of the polarizing field, we could open a mechanical relay in series with the polarizing coil to decouple the SQUID gradiometer from noise generated by the Techron amplifier, as well as from the thermal noise of the polarizing coil itself. With this simple switching scheme, the nonadiabatic criterion was satisfied for proton Larmor frequencies extending to around 2 kHz. As the strength of the measurement field was increased beyond this value, we began to encounter some loss in signal, due presumably to adiabatic reorientation of the sample magnetization during turnoff of the polarizing field. At higher measurement frequencies, we adopted a scheme involving adiabatic removal of the polarizing field and resonant spin excitation (see Section 6.G).

Spin Echo Coil

Resonant spin echo pulses were produced with a pair of coils oriented along the y direction. The coils each consisted of 10 turns of copper wire, wound on circular G10 fiberglass forms with radius 60 mm which were mounted rigidly to the polarizing coil forms. In the case of the NMR and MRI experiments performed in this system, resonant echoes were preferable to echoes formed by inverting the direction of the measurement field, as the latter type of echo does not refocus dephasing from external magnetic field gradients (either the gradients G_x , G_y , G_z which were used for the encoding, or spurious gradients due to nearby magnetic objects). For Larmor frequencies of the order of 1 kHz, a typical π pulse consisted of two or three cycles, and required currents of order 10 mA.

D. Experimental Apparatus: SQUID Sensors

The SQUID system which was housed in the LHe dewar in the center of the cube consisted of four channels: a single large-area sensing channel and three orthogonal magnetometer references. The pickup coil of the sensor was configured as a second-order axial gradiometer oriented along the x axis (vertical direction); the gradiometer was therefore sensitive to the component d^2B_x/dx^2 of the second-order magnetic field gradient tensor. The pickup loops of the gradiometer were wound from 3 mil Nb wire in grooves which were carefully machined in a cylindrical G10 fiberglass form. The radius of each pickup loop was roughly 15 mm, and the gradiometer baseline was 50 + 50 mm (Figure 6.5). The G10 form on which the pickup loop was wound fit snugly into the tail section of the G10 fiberglass LHe dewar. The distance from the sensing loop of the gradiometer to the sample, which was positioned directly under the tail of the LHe dewar, was

roughly 10 mm. The sensing SQUID was housed in a superconducting box machined from a solid block of Pb and located in the belly of the LHe dewar at a distance of approximately 300 mm from the sensing coil of the gradiometer. Superconducting contact from the Nb wire pickup coil to the 11-turn Nb input coil integrated on the SQUID chip was achieved using the solder blob technique described in Section 5.B. The sensing SQUID was operated in a flux-locked loop with modulation at 2 MHz.

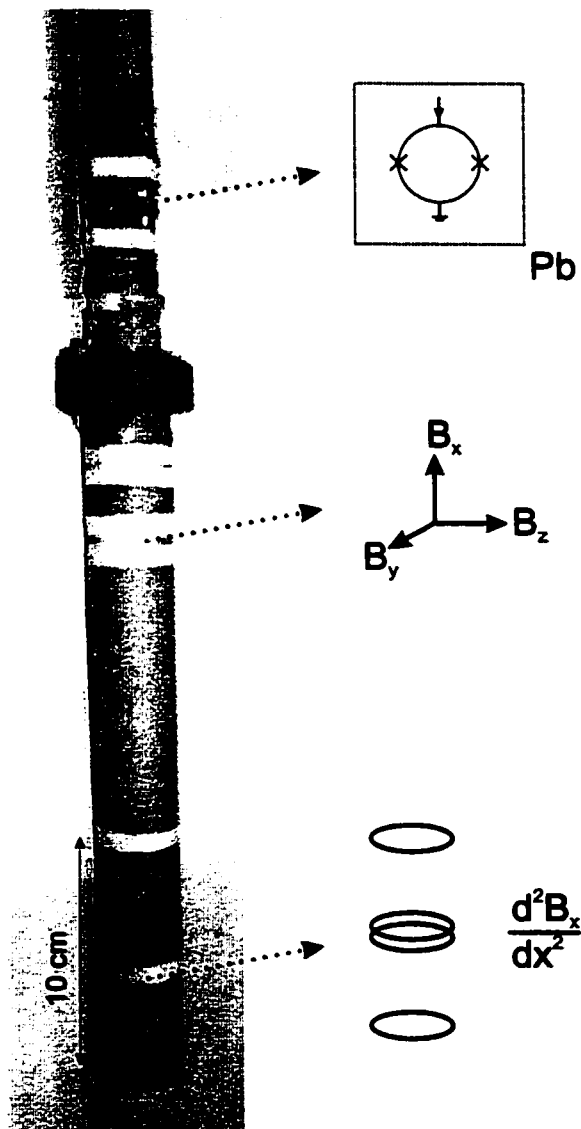


Figure 6.5. Multichannel probe for SQUID-detected MRI. The NMR detector was a second-order axial gradiometer with an overall baseline of 100 mm. The probe also incorporated a three-axis reference magnetometer; the reference SQUIDs were mounted on orthogonal faces of a G10 fiberglass cube which was positioned inside the cylindrical form on which the pickup coil of the gradiometer was wound. The SQUID of the sensing channel was housed in a superconducting Pb box, visible at the top of the photograph.

The inductance of the sensing SQUID was roughly 350 pH. This yields for the 11-turn input coil a self inductance $L_i = 40$ nH and a mutual inductance to the SQUID of $M = 3.9$ nH. For a 1 + 2 + 1 turn second-order gradiometer with pickup loop radius $r = 15$ mm, we have $L_p = 700$ nH. From relation (2.11), the above parameters yield a gradiometer sensing area A_{sense} of approximately 3.7 mm^2 . Note that the sensing area of the gradiometer could be improved substantially by proper matching of L_i and L_p . In particular, by increasing the number of turns in the input coil to around 45, so that $L_i \sim 700$ nH, the sensing area of the gradiometer could be increased to roughly 8 mm^2 . However, we found that even for a reduced sensing area of 3.7 mm^2 , our system noise was dominated by external sources of thermal noise and interference, not by the intrinsic noise of the detector. In this case, inductance mismatch does not degrade SNR, as signal and noise are attenuated equally.

To measure the balance of the gradiometer with respect to uniform fields in the three orthogonal directions, we applied known, highly uniform fields to the sensor using the cancellation coils wound on the faces of the cube, while monitoring the flux which was coupled to the sensing SQUID. The typical gradiometer balance was one part in a few hundred for both in-plane and out-of-plane fields. To achieve this level of balance, however, we did need to take care to minimize parasitic inductance associated with the Nb wire leads which ran between the gradiometer loops, and which were not twisted together.

Finally, the probe incorporated a three axis SQUID magnetometer consisting of three Nb-AlOx-Nb SQUIDs mounted on three orthogonal faces of a G10 fiberglass cube. This reference cube was mounted inside the fiberglass form on which the gradiometric

pickup coil of the sensing SQUID was wound. Each of the reference SQUIDs had an effective area of roughly 0.03 mm^2 , and was operated in a flux-locked loop with modulation at 100 kHz. Analog subtraction of the reference signals from the gradiometer signal was used to improve the balance of the gradiometer, in an attempt to further reduce the contribution of distant noise sources to the system noise. Formation of the electronic gradiometer is discussed in more detail in Section 6.I.1.

E. SQUID NMR in Unshielded Environment

Due to the large scale of the SQUID MRI system, it was not practical to enclose the experiment in a mu-metal shield. Consequently, the measurement region was subject to uncontrolled variations in magnetic field and magnetic field gradients. These variations spanned a broad range of frequencies, from dc to hundreds of MHz, and served both to disturb the desired evolution of the nuclear spins, and to degrade the performance of the SQUID detector. We consider separately the effects of these spurious fields on the spins and the SQUIDs.

1) Effect of Static Magnetic Field Gradients and Zeeman Field Drift on Evolution of Nuclear Spins

a) Static Magnetic Field Gradients

In MRI it is necessary to have exquisite control over both the strength and timing of the components G_x , G_y , and G_z of the magnetic field gradient tensor. However, in our laboratory there are substantial magnetic field gradients due to steel rebar in the floor and

walls of the building. These gradients are of the order of a few $\mu\text{T/m}$ in the center of the laboratory, and roughly an order of magnitude higher nearer the walls. In addition, nearby steel cabinets, desks, gas cylinders, etc. also generate substantial field gradients, and we made an effort to rid the area around the experiment of all such magnetic objects. These “external” magnetic field gradients were easily shimmed away by applying offset currents to the gradient coils of the imaging system, but we found that from time to time there were changes in the optimal shim settings, due perhaps to the motion of magnetic objects or to the energizing or de-energizing of magnets in nearby labs. While we needed to be aware of the possibility of changes in the magnetic gradients, and to occasionally adjust to a new gradient environment, these static “offset” magnetic field gradients represented a relatively minor nuisance.

b) Zeeman Field Drift

The most serious consequence of poor control of the magnetic field environment of the spins was drift of the proton Larmor frequency during data acquisition. NMR measurements were typically performed in magnetic fields of the order of microtesla or tens of microtesla, where the proton Larmor frequency is of the order or tens of Hz to kHz. Motion of the elevators in Birge Hall caused changes in the measurement field of around 200 nT, corresponding to a shift in Larmor frequency of 8 Hz for the proton. In the case of experiments which required signal averaging, spurious phase acquired by the spins due to this frequency shift destroyed the coherent averaging of signals acquired during the motion of the elevator.

It would have been most convenient to stabilize the measurement field by monitoring the appropriate component of the field with either a SQUID or fluxgate sensor located in the measurement region, and feeding current into the measurement coil to cancel any drift. However, the flux-locked loops which were used to read out the SQUIDs had to be disabled during the polarizing interval, and when this was done the reference for the absolute value of the magnetic field was lost (the SQUID senses only changes in magnetic field). In the case of a fluxgate reference, the relatively large fields generated during the polarizing period would have damaged the fluxgate head; this ruled out the use of such a reference in a closed-loop arrangement. It was possible to use a fluxgate reference located outside of the measurement region (just on the outside of the cancellation coils, for example) to stabilize the measurement field in an open loop arrangement: we monitored the change in field with the fluxgate, and fed a correction current which was proportional to the fluxgate output into the measurement coil. Of course, with such a cancellation scheme, it is necessary to carefully determine the correct constant of proportionality. Moreover, in the case of multiple sources of field drift, which couple differently to the fluxgate reference and to the spins in the measurement region, it is impossible to completely stabilize the measurement field. In practice, we found that we could stabilize the measurement field to about one part in ten using open loop compensation with a fluxgate magnetometer. Yet as even field drifts at the level of 10 nT were unacceptable for most experiments (as changes in Larmor frequency of fractions of 1 Hz result in accumulation of spurious phase of order 1 radian over an acquisition interval of 1 second), we generally chose to perform critical experiments late at night,

when magnetic activity in Birge Hall was minimum and we could guarantee stability of the Zeeman field by shutting down the Birge elevators.

2) SQUID System in Unshielded Environment

The effects on the SQUIDs of uncontrolled magnetic field variations were more detrimental to system performance and more difficult to mitigate. Here we consider separately the effects on the system of a) power line magnetic fields and harmonics, b) radiofrequency (rf) magnetic fields, and c) broadband noise from distant sources.

a) 60 Hz Fields and Harmonics

The 60 Hz power line magnetic fields in Birge B260 have typical amplitudes of order 100 nT, exceeding by roughly 6 orders of magnitude the strength of the magnetic fields produced in our experiments by the precessing nuclear spins. The high level of power line interference imposed strict requirements both on the slew rate of the sensing channel and on the resolution of the A/D converter used to digitize the SQUID signal. For example, for a SQUID magnetometer with effective area $A_{\text{eff}} = 4 \text{ mm}^2$, a slew rate of roughly $10^5 \Phi_0/\text{s}$ is required to follow a 60 Hz field with 100 nT amplitude. While this slew rate is readily attainable in an environment where the SQUID is well-shielded, it can be difficult to achieve when the SQUID transfer function is suppressed by high frequency interference (see Section 6.E.2.b). For this reason alone it was necessary to configure the pickup circuit of the sensor gradiometrically. We experimented with both first- and second-order axial gradiometers, and found that only the second-order configuration gave sufficient rejection of the power line magnetic fields. For a typical balance of the second-

order gradiometer of one part in a few hundred, the power line flux coupled to the SQUID of the sensing channel was of the order of one flux quantum.

While this initial stage of 60 Hz rejection was sufficient to ensure stable operation of the flux-locked loop, it was necessary to further attenuate the power line fields prior to digitization of the SQUID signal. To accomplish this we implemented a comb filter, based on the twin-T notch design [11], which covered the first ten harmonics of the 60 Hz fields and which provided an additional rejection of roughly 60 dB. Following this filter stage, the signal was digitized with 16-bit resolution. While the overall attenuation of power line fields by roughly 5 orders of magnitude boosted the NMR signal far above the bit threshold of the A/D converter, we still had to face the problem of “steering” the NMR signal around the notches at the harmonics of 60 Hz. For example, in our first experiments we tended to place the proton resonance directly at the midpoint of two power line harmonics; for imaging experiments we were restricted to a rather narrow band of around 50 Hz. Later we avoided this problem altogether by moving the proton resonance to higher frequencies of several kHz, where the power line harmonics disappeared below the system noise floor.

b) Radiofrequency Suppression of V_ϕ

The large-area pickup loop of a SQUID gradiometer acts as an efficient antenna, which couples high frequency magnetic fields to the SQUID. While the SQUID is typically read out at low frequencies, with a flux-locked loop whose small-signal bandwidth extends to hundreds of kHz or perhaps MHz, the SQUID itself responds to magnetic fields at frequencies extending up to the Josephson frequency, which is on the

order of tens of GHz for a typical device under typical operating conditions. High frequency magnetic flux has the effect of “washing out” the flux-to-voltage transfer function of the SQUID, resulting in a suppression of $V_\Phi \equiv dV/d\Phi$ and an increase in the contribution of the room temperature preamplifier to the system noise.

The effect of high frequency electromagnetic interference on the performance of rf SQUIDS was studied extensively in [12]. In the case of the dc SQUID the situation is quite similar; here we give a brief qualitative discussion. We imagine that the SQUID is optimally current biased and that we monitor the voltage across the SQUID. When the flux bias is swept at low frequency, the flux-to-voltage transfer curve of the device is traced out (Figure 6.6A). In the absence of high frequency interference, the quasistatic flux bias of the SQUID determines the sensitivity of the device to a small applied flux: for flux bias at the extrema of the transfer curve (point A in Figure 6.6), a small time-varying flux $\Delta\Phi$ results in no change in the voltage across the SQUID, while flux bias at the steepest points of the transfer curve (point B in Figure 6.6) results in a maximum voltage change $V_\Phi \Delta\Phi \approx \pi V_{p-p} \Delta\Phi$. We now imagine that the SQUID is additionally subjected to a magnetic flux with peak-to-peak amplitude $\Phi_{rf} < \Phi_0$ at a frequency that lies far outside the bandwidth of the electronics used to read out the SQUID (Figure 6.6B). The SQUID samples a range Φ_{rf} of bias points on the V - Φ curve, and it is the time-averaged voltage across the SQUID that is read out at low frequency by the room temperature electronics. For a quasistatic flux bias at the steepest points B of the transfer curve, the time averaged voltage across the SQUID is not affected by the rf irradiation. However, for flux bias at the extrema A of the V - Φ curve, the time-averaged voltage across the SQUID is reduced by the application of Φ_{rf} , as the SQUID now samples points

that are removed from these extrema. The overall effect is to “wash out” the $V-\Phi$ curve and to reduce the gain of the SQUID. In the extreme case, high frequency interference renders it impossible to detect any signal whatsoever from the SQUID. More generally, rf interference is a serious problem whenever the input voltage noise of the room temperature preamplifier $S_v^{1/2}$ referred to the SQUID (via V_Φ) becomes comparable to the dominant source of flux noise in the SQUID (either environmental flux noise, or in the case of a SQUID magnetometer operated with adequate magnetic shielding, the intrinsic noise of the SQUID itself). For example, for a preamplifier noise of $0.1 \text{ nV/Hz}^{1/2}$ (at the input of the primary of the transformer), a transfer function suppressed to the level of $10 \text{ } \mu\text{V}$ peak-to-peak results in a preamplifier noise of roughly $3 \text{ } \mu\Phi_0/\text{Hz}^{1/2}$ referred to the SQUID, already a factor of three or so above the intrinsic flux noise of a high-quality low- T_c SQUID.

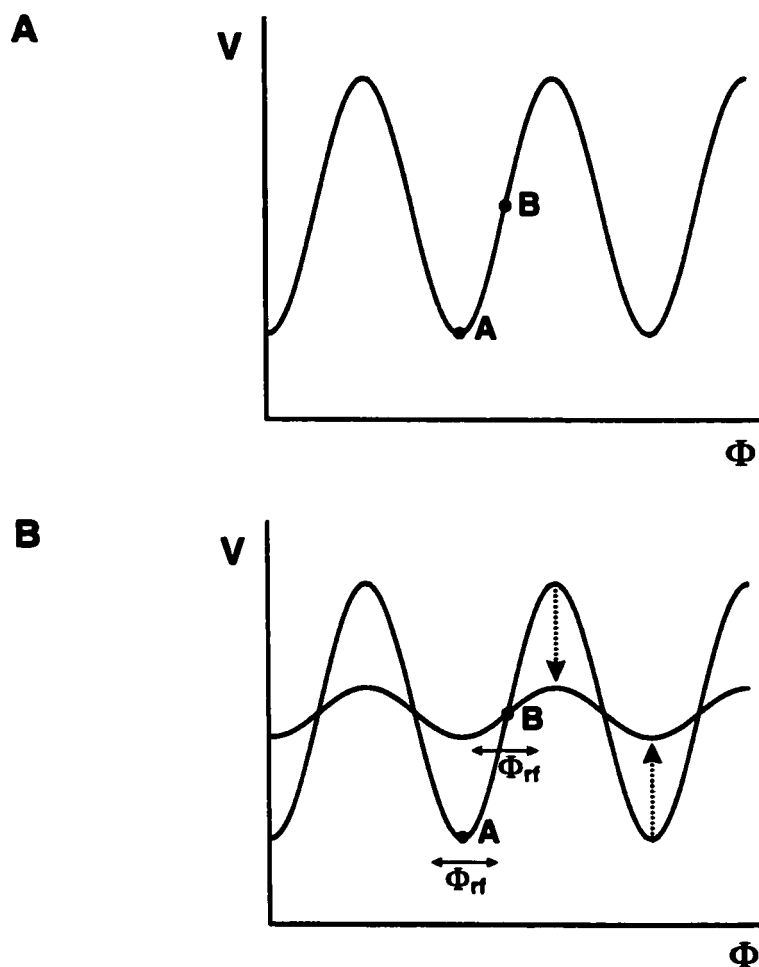


Figure 6.6. Radiofrequency suppression of V_Φ (A) SQUID flux-to-voltage transfer curve. For flux bias at point A, a small applied flux $\Delta\Phi$ produces no change in voltage across the SQUID. For flux bias at point B, the steepest point on the transfer curve, a small applied flux $\Delta\Phi$ produces the maximal voltage change $V_\Phi\Delta\Phi \sim \pi V_{p-p}\Delta\Phi$. (B) Flux-to-voltage transfer curve of a SQUID subjected to a high frequency interfering flux Φ_{rf} . For quasistatic flux bias at point B, the time-averaged voltage across the SQUID is unchanged. For quasistatic flux bias at point A, however, SQUID now samples points removed from the extremum of the V - Φ curve. As a result, the signal from the SQUID, read out at low frequency with room temperature electronics, is suppressed.

There are numerous sources of high-frequency interference in the average laboratory. Radiofrequency transmissions are a serious problem for systems operated near or above ground level. Even in a basement laboratory, computer monitors and digital test equipment generate sufficiently high levels of rf to wholly suppress the signal from

large-area ($A_{\text{eff}} \sim 1 \text{ mm}^2$) SQUID magnetometers unless adequate measures are taken either to shield the magnetometer from rf fields or to filter high frequency currents in the SQUID pickup circuit. The most reliable way to protect a SQUID magnetometer from degradation due to rf interference is to enclose the experiment in a Faraday cage, consisting of copper mesh or of copper or aluminum foil, and which provides eddy-current screening of high frequency magnetic fields.

Due to the size of the SQUID MRI system, it was impractical to surround the entire experiment in a Faraday cage (or so it seemed to us initially; see Section 6.J). On the other hand, when we attempted to operate the gradiometer entirely without rf shielding, no SQUID signal could be detected. To shield the gradiometer from interfering rf flux, we found it sufficient to surround the liquid helium dewar with several layers of aluminum foil. The foil acts as an excellent magnetic shield at radio frequencies, yet in the relevant range of Larmor frequencies, tens of Hz to a few kHz, it is essentially transparent. When the aluminum foil shield was completely sealed and well connected to the electrical ground, we found that the effect of rf interference on the noise of the system was negligible. However, the proximity of the aluminum shield to the gradiometer introduced another problem: Nyquist currents in the aluminum foil produced magnetic field noise at the level of roughly $30 \text{ fT/Hz}^{1/2}$, and proved to be the dominant contribution to the system field noise.

After a certain amount of trial and error we settled on the following arrangement: we eliminated all aluminum foil from the tail section of the dewar and restricted the amount of material in the rf shield (which was now open at the bottom, surrounding the belly and top of the dewar, with a connection to ground at the brass dewar neck) to a

single layer of aluminum foil; Nyquist noise fields generated by this reduced shield did not contribute significantly to the noise of the system. In addition, we incorporated an rf filter into the SQUID pickup circuit. This consisted of 660 pF soldered across the input coil. We used for the filter two surface mount capacitors, and connected them across the solder blobs where we made the superconducting joints from the Nb wire of the pickup coil to the annealed Nb wire which was ultrasonically bonded to the Nb contact pads of the input coil on the SQUID chip. The parallel combination of this 660 pF capacitor with the 42 nH input coil of the SQUID formed a current divider for high frequency currents induced in the pickup circuit, with a rolloff frequency of around 30 MHz. With this filter and the moderate shielding described above, the transfer function of the SQUID was suppressed to only about 20 μV p-p when the system was operated outside a Faraday cage. For a preamp noise of $0.1 \text{ nV/Hz}^{1/2}$, this corresponds to a negligible flux noise of $1.6 \mu\Phi_0/\text{Hz}^{1/2}$, or a field noise of $0.9 \text{ fT/Hz}^{1/2}$ referred to the sensing loop of the gradiometer. At both lower and higher values of the filter capacitor, the SQUID transfer function was further suppressed: at lower values presumably as the filter was less effective, and at higher values perhaps due to resonant currents which flowed in the input coil, coupling high frequency flux to the SQUID.

c) Broadband Noise from the Environment

The intrinsic flux noise of a high-quality Nb-AlOx-Nb SQUID, due to the Nyquist noise of the normal metal resistors shunting the junctions, is of the order of $1 \mu\Phi_0/\text{Hz}^{1/2}$. For a gradiometer with sensing area A_{sense} of approximately 4 mm^2 , this flux noise corresponds to an intrinsic magnetic field noise of $0.5 \text{ fT/Hz}^{1/2}$. However, unless the

pickup loops of a gradiometer are extremely well-shielded from both distant and nearby sources of magnetic field noise, it is exceedingly difficult to approach the $1 \text{ fT/Hz}^{1/2}$ noise level. It is generally the case that the noise of a SQUID system for unshielded operation at low frequencies is dominated by the magnetic field environment of the sensor, rather than by the noise of the SQUID itself or the SQUID readout electronics. For the initial experiments performed in the SQUID MRI system, the magnetic field noise referred to the sensing loop of the gradiometer was roughly $15 \text{ fT/Hz}^{1/2}$. Separate noise measurements of the gradiometer performed in a copper enclosure (which acted as an efficient magnetic shield at the relevant frequencies of a few kHz) enabled us to determine that local (i.e., within the cryostat) and distant sources contributed roughly equally to this overall field noise. As the averaging time required to perform a given NMR experiment goes inversely as the square of the SNR achievable without averaging, and as there are practical limits to the polarizations we can attain in our experiment (set by heating in the polarizing coil and by the requirement of rapid switching of the polarizing field), reduction of the magnetic field noise is the only way to achieve the substantial reduction in averaging times required for the SQUID system to ultimately compete with conventional high-field MRI scanners.

A detailed discussion of the issue of environmental noise, which is central to the success or failure of our approach to low-field MRI, is postponed to Section 6.I. Briefly, to reduce the noise contribution from distant sources, it is necessary either to improve the balance of the gradiometric detector, or to attenuate the interfering magnetic fields, for example, with an eddy current shield. Both of these approaches are described in Section 6.I.1. To reduce the noise contribution from local sources, it is necessary to carefully

redesign the cryostat to minimize the amount of normal metal in the insulation jacket.

Ongoing work in this direction is described in Section 6.I.2.

F. Choice of Measurement Field

In all of the NMR and MRI experiments performed in this system, the sample magnetization was enhanced by prepolarization in a field of the order of tens of millitesla. In the case of fixed sample magnetization and detection with an untuned SQUID magnetometer or gradiometer, the integrated intensity of the NMR signal is independent of the strength of the measurement field. This fact allowed us considerable freedom in the choice of measurement field strength for our experiments. The choice of measurement field was dictated by the following considerations: 1) inhomogeneous broadening due to spurious gradients generated by measurement field coil; 2) level of environmental interference and noise over the signal band; and 3) the strength of fields generated by gradient coils, relative to the measurement field strength (possible image distortion due to concomitant gradients). I briefly address each of these issues below.

1) Inhomogeneous Line Broadening and Dependence on Measurement Field Strength

In the case of the NMR experiments performed in this system (and in contrast to the experiments described in Chapter 5), the measurement field generated by the Helmholtz coils was quite homogeneous over the volume of a sample with dimensions on the order of a few tens of millimeters. On the other hand, due to the absence of any magnetic shielding, the measurement region was subject to static magnetic field gradients

generated by nearby magnetic objects, especially structural steel in the floor and walls of the building (see Section 6.E.1.a). As mentioned above, the strength of these “offset gradients” was of the order of $10\ \mu\text{T/m}$; these gradients were the principle source of inhomogeneous broadening in the experiments carried out in the SQUID MRI system.

Depending on the care with which we wished to adapt to a gradient environment which changed slightly over a timescale of days, we could more or less accurately shim away these external gradients by applying equal and opposite offset gradients with the Maxwell and Golay gradient coils. In general, the shim was somewhat less than perfect; in the case of an NMR sample of a few tens of milliliters of water (for which T_2 exceeds 1 s), for example, we typically achieved linewidths of around 2 Hz. For gradient fields which are independent of the source which generates the measurement field, the absolute homogeneity of the measurement field is independent of the strength of the measurement field; therefore, there is no advantage in terms of either SNR or resolution in reducing the measurement field strength. Indeed, when we acquired a back-to-back series of NMR spectra from a sample of water at different measurement field strengths (from several microtesla to several tens of microtesla), we found that the NMR linewidth was independent of measurement field.

For these reasons, inhomogeneous line broadening was in fact not a consideration in the choice of measurement field.

2) Environmental Interference

Again, due to the fact that the system was operated without magnetic shielding, the measurement region was subject to high levels of magnetic field noise and

interference from distant sources. At frequencies of a few kHz, the magnetic field noise measured with the reference magnetometers was of the order of $1 \text{ pT/Hz}^{1/2}$ (corresponding to about $10 \text{ fT/Hz}^{1/2}$ referred to the sensing loop of the gradiometer for a typical gradiometer balance); the noise level increased at lower frequencies, and approached $10 \text{ pT/Hz}^{1/2}$ (as measured with the reference magnetometers) below 100 Hz. In addition, power line interference at 60 Hz and harmonics (especially odd harmonics) far exceeded the level of the background magnetic field noise (the typical amplitude of power line magnetic fields in the laboratory was 100 nT).

Initial NMR experiments were performed at Larmor frequencies of a few hundred Hz. In the case of imaging experiments, we were forced to place the proton resonance directly between two harmonics of the power line magnetic fields, and to encode the image in a relatively narrow band of about 50 Hz. In order both to avoid the higher levels of environmental interference at low frequencies, and to allow encoding over a broader band, subsequent experiments were performed at higher frequencies of a few kHz, where the power line harmonics begin to disappear below the noise floor. At higher measurement frequencies (above 2 kHz or so), nonadiabatic turnoff of the polarizing field became impractical, and we adopted a scheme involving adiabatic turnoff of the polarizing field and resonant spin excitation (see Figure 6.7B).

Finally, we note that an additional and potentially very great advantage of operating at higher measurement frequencies of a few kHz is that eddy current shielding starts to become practical at these frequencies. This point is discussed at greater length in Section 6.J.

3) Image Distortion Due to Concomitant Gradients

From the zero-divergence and zero-curl conditions on the magnetic field in a source-free region, it is clear that it is impossible to generate a magnetic field gradient environment which contains only the gradients $G_x \equiv dB_z/dx$, $G_y \equiv dB_z/dy$, and $G_z \equiv dB_z/dz$ which are needed to encode an MRI. Whenever there is the gradient component dB_z/dy , for example, there is an equal and opposite gradient dB_z/dz . In the high-field case, the so-called concomitant gradient components can be neglected, as the small transverse fields generated by these gradients add in quadrature with the large Zeeman field, producing a negligible change in Larmor frequency. As the measurement field is reduced, however, the concomitant gradients give rise to transverse fields which become comparable to the measurement field, and image reconstruction is considerably complicated.

To avoid this problem, we required that the center proton frequency be significantly greater (by a factor of ten or so) than the width of the band used for encoding an image. For example, for an imaging band of around 150 Hz (typical for our experiments), it was sufficient to operate in a field of 36 μ T, corresponding to a proton Larmor frequency of 1.5 kHz.

Interestingly, in the extreme case of zero measurement field (i.e. a pure gradient environment), image reconstruction becomes straightforward once again. While there has been some theoretical work on zero-field reconstruction [13], this has not yet been pursued experimentally, in large part due to the high levels of environmental interference at frequencies approaching 0 Hz.

G. NMR Experiments

The procedure for performing NMR experiments in the cube was as follows. First, appropriate currents were passed through the cancellation coils to zero out the static magnetic field of the Earth over the measurement region. For this purpose, a three-axis fluxgate magnetometer placed directly under the tail of the cryostat was used to monitor the field in the measurement region. The desired measurement field, of the order of microtesla or tens of microtesla, was then applied with the 1.2 m diameter Helmholtz pair. After allowing some time for the measurement field to stabilize, we placed the sample under the tail of the cryostat and tuned the SQUID gradiometer.

As mentioned above, two different polarization and excitation schemes were employed in our experiment: at lower measurement fields (corresponding to Larmor frequencies below about 2 kHz), spin precession was initiated by nonadiabatic turnoff of the polarizing field; at higher measurement fields, the polarizing field was reduced to zero adiabatically, and a resonant $\pi/2$ pulse was used to induce precession. In both cases, we typically detected a spin echo, which was formed with a resonant π pulse. The NMR pulse sequences are shown in Figure 6.7.

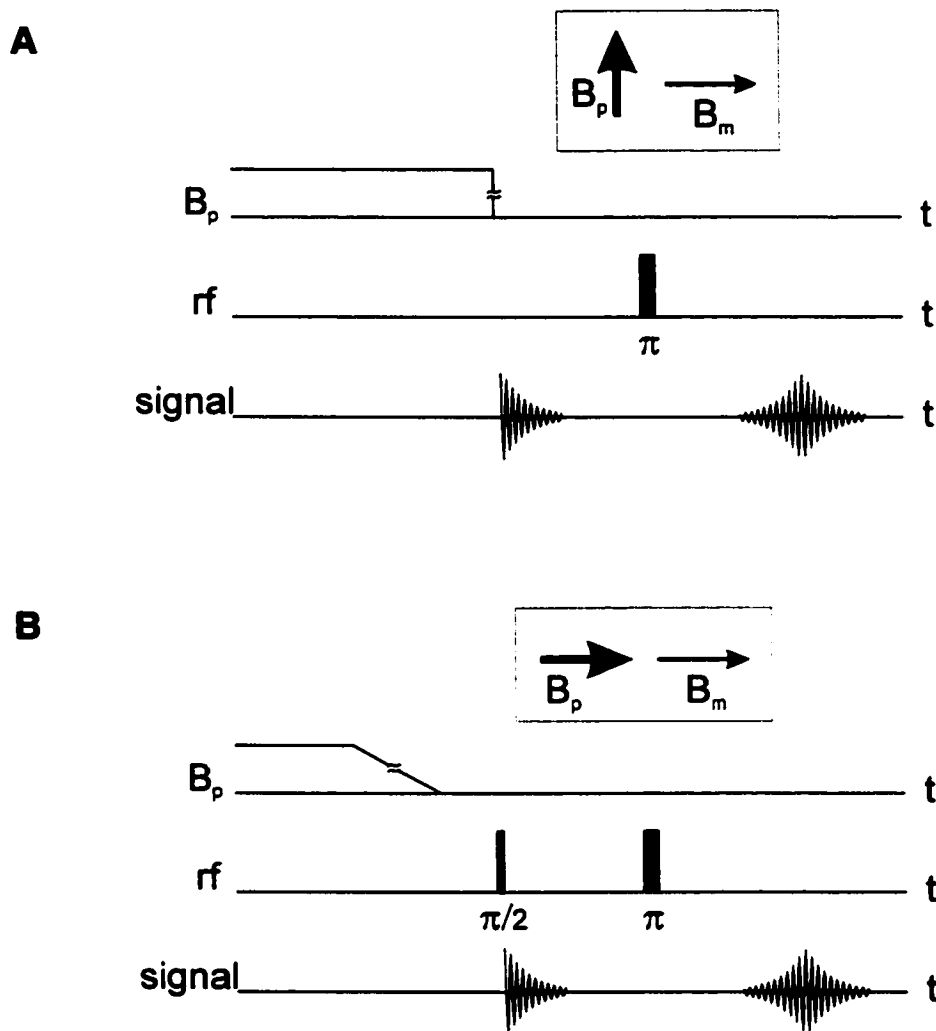


Figure 6.7. Pulse sequences used for SQUID-detected MRI. (A) In this sequence, precession is induced by the nonadiabatic turnoff of the polarizing field B_p (of the order of tens of millitesla), which is oriented in a direction orthogonal to the measurement field B_m . The measurement field is static; a spin echo is formed with a resonant π pulse. (B) In this sequence, the strength of the polarizing field B_p is reduced adiabatically to zero, and precession is induced with a resonant $\pi/2$ pulse. In this case, the polarizing field is applied along the measurement field direction, to avoid signal loss due to imperfect fulfillment of the adiabatic switching criterion. In both (A) and (B), turnoff of the polarizing field is accomplished in a time of order 10 ms; adiabaticity or nonadibaticity of the turnoff is determined by the Larmor period of the nuclear spins in the measurement field. The nonadiabatic turnoff of (A) was used for measurement fields below about 50 μT ; at higher measurement field strengths, the switching of the polarizing field was adiabatic, and only sequence (B) was used.

In our experiments, polarizing field strengths were of the order of a few tens of millitesla, and the polarizing field was applied for a time which was long compared to the spin-lattice relaxation time T_1 of the sample (we used polarizing intervals of 2-3 s for water, and of around 100 ms for mineral oil). Following turnoff of the polarizing field and application of the echo pulse, mechanical relays in series with the polarizing and echo coils were opened. This was done to isolate the SQUID gradiometer from the noise of the amplifiers used to drive the polarizing and echo coils, as well as to prevent the flow of Nyquist noise currents in these coils. The flux-locked loop was enabled shortly after transmission of the echo pulse. The output of the flux-locked loop was passed through sample-and-hold and filtering stages and then digitized; signal averaging was performed in software.

When the external gradients were properly compensated, we obtained NMR linewidths of order 1 Hz from a test sample of water. With a polarizing field of roughly 40 mT, we obtained an SNR ratio of 50 in a single shot from a sample of around 20 ml of water. Figure 6.8 shows a typical proton spectrum, measured in a field of 10.6 μ T. The proton signal appears at around 3.6 kHz; the additional peaks are due to some very high harmonics of the power line magnetic fields in the laboratory, as well as to additional environmental interference at discrete frequencies.

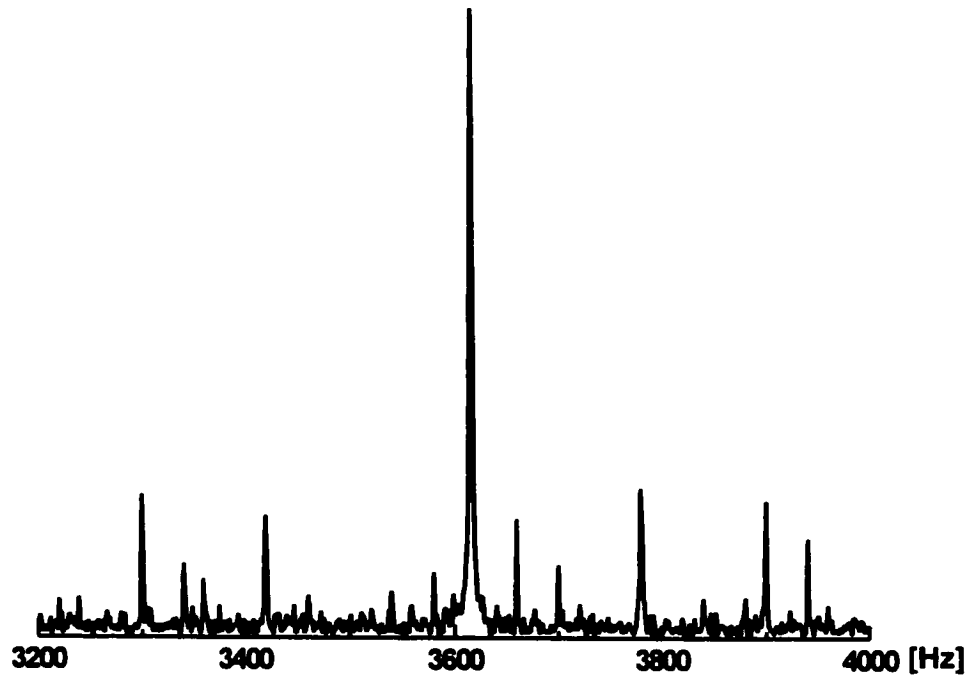


Figure 6.8. Single-shot NMR spectrum of water measured in a field of $85\ \mu\text{T}$. The spectrum was acquired with the sequence of Figure 6.7B. The effective sample volume was roughly 20 ml; external magnetic field gradients due primarily to steel rebar in the floor of the laboratory were shimmed to yield an NMR linewidth of about 1 Hz. The proton resonance appears near 3600 Hz, with an SNR of about 50. The additional lines are due to high harmonics of the 60 Hz power line magnetic fields in the laboratory, as well as to other sources of environmental interference.

H. MRI Experiments

For our imaging experiments, we chose projection reconstruction over Fourier reconstruction due to the limited hardware requirements as well as the ease with which this encoding scheme is adapted to SQUID detection. MRIs were acquired from tap water or mineral oil phantoms. The phantoms were chosen to have translational symmetry in one direction, which was arranged to coincide with the axis of the second-order gradiometer (the x axis). The lateral (y-z) dimensions of the phantom were chosen to roughly match the dimensions of the sensing loop of the gradiometer (30 mm diameter).

The gradient component G_x was nulled out using the appropriate set of Golay coils; applied gradients G_y and G_z were used to encode in the y-z plane. No attempt was made to perform slice selection, although of course the sensitivity of the SQUID gradiometer fell off rapidly as a function of the separation of the source from the sensing loop. Therefore the MRIs we obtained were two-dimensional cross sectional images of the phantoms.

The first experiments were carried out with tap water phantoms. In this case, the long T_2 (of the order of seconds) made it possible to achieve very narrow lines of 1-2 Hz in low field, and therefore to take full advantage of signal bandwidth narrowing in order to enhance SNR and resolution. However, the long T_1 necessitated polarization times of the order of seconds. Due to the long polarizing interval, overall image acquisition times were rather long, of the order of a few hours.

Subsequent imaging experiments were performed with mineral oil, which in any case is a better match to human tissue in terms of its NMR relaxation properties. Here T_2 is shorter, and we achieved (lifetime limited) proton linewidths of around 5 Hz. The broader NMR lines required us to encode over a broader band in the MRI experiments. On the other hand, the shorter T_1 of mineral oil enabled us to decrease the polarizing interval significantly, to around 100 ms, resulting in a substantial reduction in image acquisition times.

Figure 6.9 shows an MRI acquired from a mineral oil phantom in a field of 36 μ T, corresponding to a proton Larmor frequency of around 1.5 kHz. The phantom consisted of nine columns arranged on a square lattice; the diameter of each column was 6 mm, and the center-to-center separation of the columns was 8 mm. The image was acquired using

the sequence of Figure 6.7A in a gradient of $70\ \mu\text{T/m}$, which broadened the NMR signal from the phantom over a band of around 150 Hz. 48 one-dimensional projections were acquired in angular increments of 3.75° . For each projection, we averaged 128 spin echo signals. The overall acquisition time was 40 minutes. A two-dimensional image was built up from the 48 projections using the technique of filtered back projection [14]. From the image, we estimate the spatial resolution to be roughly 1 mm.

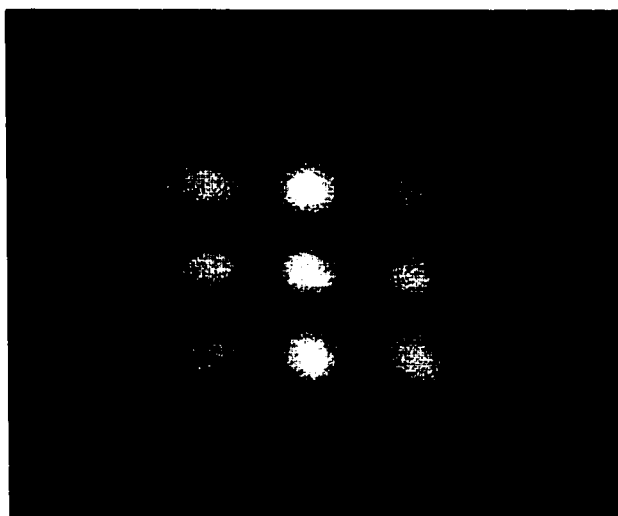


Figure 6.9. MRI of mineral oil phantom acquired in a field of $36\ \mu\text{T}$. The sample consisted of nine columns of mineral oil; the diameter of each column was 6 mm, and the center-to-center separation of the columns was 8 mm. NMR spectra were acquired in a static magnetic field gradient of $70\ \mu\text{T/m}$, which broadened the NMR signal from the phantom over a band of about 150 Hz. The gradient direction was stepped in angular increments of 3.75° ; at each gradient direction, 128 spin echo signals were averaged. The overall acquisition time was 40 minutes.

While preliminary experiments such as this demonstrated the soundness of the concept of microtesla field MRI, 40 minutes is an excessively long acquisition time by the standards of conventional high-field MRI. The acquisition times could be substantially reduced, however, by reduction of the system noise. The remainder of this

chapter is devoted to the important issue of magnetic field noise in the SQUID MRI system, and to possible means for reducing the noise.

I. Magnetic Field Noise of the System

In an NMR or MRI experiment, the averaging time required to achieve a given SNR goes inversely as the square of the SNR obtained in a single acquisition. For this reason, it is essential to minimize the noise of the detector. In the case of the SQUID MRI system, the overall field noise in the relevant frequency range was roughly $15 \text{ fT/Hz}^{1/2}$ referred to the sensing loop of the gradiometer (Figure 6.10A), more than an order of magnitude higher than the intrinsic noise of the detector (an intrinsic flux noise of $1 \mu\Phi_0/\text{Hz}^{1/2}$ corresponds to a field noise of $0.5 \text{ fT/Hz}^{1/2}$ for a gradiometer with sensing area $A_{\text{sense}} = 4 \text{ mm}^2$). This noise was due to roughly equal contributions from local (i.e., within the cryostat) sources of thermal noise, and distant sources of environmental noise and interference. This can be seen from the following set of measurements.

When the cryostat was moved to a commercial copper enclosure, which acted as an efficient magnetic shield in the relevant frequency range of a few kHz, we achieved a magnetic field noise of around $10 \text{ fT/Hz}^{1/2}$ referred to the sensing loop of the gradiometer, when the gradiometer was lowered completely into the tail section of the cryostat (Figure 6.10B). In this case, the copper enclosure essentially eliminated any noise contribution from distant environmental noise sources; $10 \text{ fT/Hz}^{1/2}$ was therefore the noise contribution of the cryostat. On the other hand, when the cryostat was moved back to the open environment of the SQUID MRI system and the gradiometer was raised up out of the tail section of the cryostat, we also measured a noise of roughly $10 \text{ fT/Hz}^{1/2}$

(Figure 6.10C). In this case, the gradiometer pickup loops were decoupled from any sources of thermal noise in the insulation jacket of the cryostat, and the measured noise was due to the contribution of distant sources (attenuated by the balance of the gradiometer). During the NMR experiments, the contributions of the local and distant noise sources added in quadrature, accounting for the overall system noise level of roughly $15 \text{ fT/Hz}^{1/2}$. As a final check, we measured the noise inside the copper enclosure with the gradiometer pickup loops raised up out of the tail section of the cryostat. In this case we achieved a noise level of around $3 \text{ fT/Hz}^{1/2}$ (Figure 6.10D), which was still above the estimated intrinsic noise of the detector, and which might have been due to residual thermal noise of the cryostat, or to magnetic impurities in the G10 fiberglass material of the form on which the gradiometer was wound.

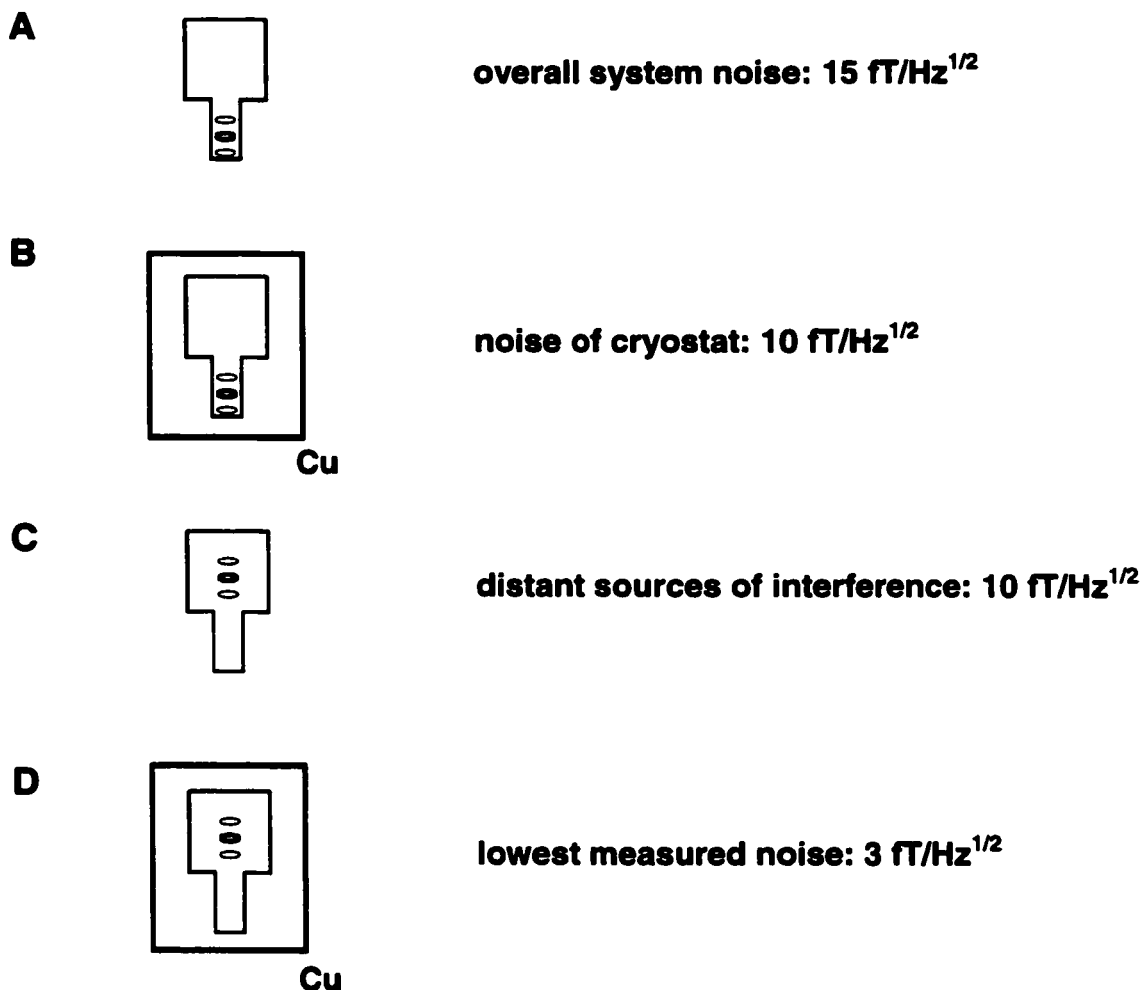


Figure 6.10. Sources of noise in the SQUID MRI system. (A) The overall system noise was measured to be about $15 \text{ fT/Hz}^{1/2}$ at frequencies of a few kHz when the gradiometer was lowered into the tail section of the cryostat and the system was operated without any eddy current shielding (this was the situation during the NMR and MRI experiments). (B) When the system was moved into a copper shielded enclosure, the noise was measured to be $10 \text{ fT/Hz}^{1/2}$: this represents the thermal noise of the cryostat. (C) When the system was operated unshielded and the gradiometer was decoupled from metallic parts in the insulation jacket of the cryostat, the noise was measured to be $10 \text{ fT/Hz}^{1/2}$: this represents the contribution of distant sources of environmental noise and interference to the overall system noise. (D) When the gradiometer was decoupled to the fullest possible extent from both local and distant sources of magnetic field noise, the gradiometer noise was measured to be roughly $3 \text{ fT/Hz}^{1/2}$, still far above the estimated intrinsic noise of the device of roughly $0.5 \text{ fT/Hz}^{1/2}$.

Below I examine in some depth the nature of the magnetic field noise generated by distant and local sources, and discuss ongoing attempts to reduce the noise.

1) Distant Sources of Environmental Noise and Interference

The magnetic field noise at the center of the SQUID MRI system, measured with the three axis reference magnetometer, was of the order of $1 \text{ pT/Hz}^{1/2}$ at frequencies of a few kHz. The spectrum of the field noise appeared to be more or less white at these frequencies. Separate noise measurements performed with the same SQUIDs, in the same probe and the same cryostat, but in the above-mentioned copper shielded enclosure, yielded field noise on the order of hundreds of $\text{fT/Hz}^{1/2}$. The discrepancy between the magnetic field noise levels measured inside and outside the copper enclosure (which to first order eliminates any magnetic field noise of nonlocal origin in the relevant range of frequencies) indicates that the field noise measured by the reference magnetometer in the center of the SQUID MRI system is dominated by distant sources of magnetic field noise and interference. (The reduced noise measured in the copper enclosure was not due to reduced rf suppression of the SQUID transfer function. Due to their small effective area $\sim 0.03 \text{ mm}^2$, the reference SQUIDs were not particularly susceptible to rf interference; moreover, these low-inductance SQUIDs had enormous transfer functions V_Φ of a few hundred $\mu\text{V}/\Phi_0$.) Given the measured balance of roughly 1 part in 100 of the second-order gradiometer, a uniform field noise of $1 \text{ pT/Hz}^{1/2}$ corresponds to $10 \text{ fT/Hz}^{1/2}$ referred to the gradiometer sensing loop, roughly equal to the field noise contributed by metallic objects in the insulation jacket of the cryostat (Section 6.I.2).

While the exact origin of the uniform field noise remains unclear, several possible candidates come to mind. Any piece of normal metal will generate thermal magnetic noise, with a spectrum which is white at low frequencies (at high frequencies the magnetic field noise will roll off, due to eddy current self-screening and a reduction in the effective mass of normal metal). As the thermal noise from a metallic object falls away with distance on a length scale which is set by the size of the object, the large pieces of structural steel in the floor and walls of the laboratory might be expected to couple magnetic field noise efficiently to the SQUID sensors, which were located at a height of roughly 1 m from the laboratory floor. On the other hand, it is possible that the spectral density of field noise of the sensor was not in fact white, but rather the result of a multitude of discrete frequencies closely spaced together, arising from the operation of test equipment in the surrounding laboratories and from activity on the power grid: it is conceivable, for instance, that abrupt changes in the current drawn from the grid generate harmonics which extend out to relatively high frequencies. The fact that the field noise seemed to be slightly lower late at night, when activity on the power grid is presumably lowest, supports this latter picture. Finally, one might be tempted to search for more exotic explanations for the observed field noise at the pT level, such as electrical activity in the ionosphere.

Regardless of the exact nature of the source or sources of the uniform field noise, the only way to reduce the contribution of distant sources to the system noise (short of implementing a magnetic or eddy current shield; see Section 6.J) is to improve the balance of the gradiometer. Following Vrba [15], we write the response of the hardware

second-order gradiometer to a local gradient source and a distant source of uniform field as follows:

$$S = G + \alpha_x B_x + \alpha_y B_y + \alpha_z B_z . \quad (6.3)$$

Here G represents the second-order gradient d^2B_x/dx^2 (the response of the gradiometer to second gradients has been normalized to unity); \mathbf{B} is the uniform magnetic field over the device; and the vector α represents the response of the gradiometer to uniform fields. The components of α are determined by the balance of the gradiometer in the three orthogonal directions (for perfect alignment of the gradiometer pickup loops and perfect matching of the pickup loop areas, $\alpha = 0$). We can neglect gradient fields produced by the distant source, as their contribution will be negligible compared to that of the uniform field.

The goal is to eliminate the response of the gradiometer to the uniform field \mathbf{B} . This can be done simply by subtracting appropriately scaled signals from three orthogonal reference magnetometers from the signal S of the hardware gradiometer. Such an electronic gradiometer is easily implemented with analog circuitry. We write the response S^{elec} of the electronic gradiometer as follows:

$$S^{\text{elec}} = G + \alpha \cdot \mathbf{B} + \beta \cdot \mathbf{B}^{\text{ref}}, \quad (6.4)$$

where the vector \mathbf{B}^{ref} represents the measured response of the three reference magnetometers, and the components of the vector β are scaling factors which are adjusted to minimize the response of the gradiometer to applied uniform fields. When β is chosen to meet the balance condition $\alpha \cdot \mathbf{B} = -\beta \cdot \mathbf{B}^{\text{ref}}$, the electronic gradiometer is insensitive to uniform magnetic fields.

We implemented such an electronic gradiometer using the three SQUID references in the multichannel probe and an analog adder circuit with adjustable gain for each channel. To balance the gradiometer we applied uniform low frequency ($f \sim 10$ Hz) fields to the gradiometer and reference SQUIDs using the three sets of cancellation coils of the SQUID MRI system. We performed a lock-in measurement, and adjusted the summing coefficients (gain potentiometers in the adding circuit) by hand to minimize the response of the electronic gradiometer to the driving field. Using this analog subtraction, we were able to improve the balance of the gradiometer by more than two orders of magnitude at low frequencies, corresponding to an overall balance against uniform fields of better than one part in 10^4 .

At high frequencies, however, the balance of the gradiometer was considerably worse. In general, when a gradiometer is operated in the vicinity of any piece of normal metal, an applied uniform magnetic field at a frequency f will generate eddy currents in the normal metal; the normal metal then becomes a local source of magnetic field and magnetic field gradients, giving rise to an out-of-phase component of the gradiometer response which significantly degrades balance at high frequencies. We can write the response of the gradiometer as

$$S^{\text{elec}}(f) = G + \alpha \cdot \mathbf{B} + \beta \cdot \mathbf{B}^{\text{ref}} + \mathbf{E}(f) \cdot d\mathbf{B}/dt, \quad (6.5)$$

where the eddy current vector \mathbf{E} describes the coupling of flux to the gradiometer due to magnetic field gradients generated by local sources of eddy currents; the components of the eddy current vector are dependent on the arrangement of normal metal objects in the vicinity of the sensors, and on their conductivity. Moreover, \mathbf{E} is a function of frequency;

therefore, the gradiometer response S^{elec} also becomes a function of the frequency of the driving field.

As we measured the balance of the electronic gradiometer in the SQUID MRI system, we found that, at driving frequencies around 100 Hz, the response of the gradiometer and the reference magnetometers was no longer in phase with the driving field: the references were as much as 10° out of phase with the driving field, while the gradiometer, which is largely insensitive to the driving field and detects primarily the eddy current field, exhibited significantly larger phase shifts. The out-of-phase response of the sensors destroyed the balance of the electronic gradiometer at these frequencies; as a result, a simple analog subtraction of the signals from the reference magnetometers did not lead to any reduction of system noise in the relevant frequency range of hundreds of Hz to a few kHz.

As a final attempt to improve gradiometer balance through analog subtraction, we incorporated an adjustable phase shift in each of the reference SQUID channels. In principle, for a driving field at fixed frequency, a set of references with adjustable gain and phase is sufficient to compensate both the intrinsic imbalance of a hardware gradiometer, as well as imbalance due to local sources of eddy currents. Indeed, we found that for well-defined driving fields (produced by the cancellation coils of the SQUID MRI system) at a fixed frequency in the range of a few hundred Hz to a few kHz, we could improve gradiometer balance by roughly two orders of magnitude by subtraction of the reference signals, with appropriate gain and phase adjustment, from the signal of the hardware gradiometer. However, the same gain and phase coefficients which give a minimum response to a nominally uniform driving field at fixed frequency did not

yield a reduction in the noise of the electronic gradiometer at that frequency. This indicates merely that the gradients associated with the driving noise fields are different from those associated with the test fields applied to balance the gradiometer. As the exact character of the driving noise field is unknown (there are most likely several if not many sources which contribute to the environmental magnetic field noise at the location of the SQUID MRI system), the search for the gain and phase coefficients of the reference channels which lead to a reduction in the environmental noise at some frequency amounts to a more or less random search in a six-dimensional phase space. Moreover, due to the fact that the eddy current vector is frequency-dependent, the amplitudes and phases of the signals from the references must be adjusted separately at every frequency in order to balance the gradiometer over a broad band; it is clearly impossible to implement such a scheme with analog circuitry.

Adaptive algorithms have been developed which enable software balancing of the gradiometer by variation of the summation coefficients (amplitude and phase) of the reference signals to give a minimum in noise power over a given band. It is possible that such algorithms could be used to minimize the contribution of distant noise sources even in the presence of large phase shifts between reference and sensing channels; and it might be that these algorithms could be used to achieve a noise reduction over a relatively broad band. However, software balancing schemes require digitization of both the sensor and reference channels; moreover, they are extremely computationally intensive, and typically they do not work in real time. For these reasons, such schemes have not to date been adopted in our experiment.

To summarize, all attempts at achieving a noise reduction through analog subtraction of reference signals failed, due to the significant out-of-phase response of the sensors caused by eddy currents in the relevant frequency range of a few hundred Hz to a few kHz. Thus, while the reference SQUIDs were without question extremely useful in characterizing the magnetic field noise environment in the center of the cube, they were not used in the NMR and MRI experiments. While it is possible that the reference SQUIDs could be used as part of a future software balancing scheme, at the present time it appears that the surest way to eliminate the noise contribution from distant sources of interference is to implement a normal metal eddy current shield. This is discussed in Section 6.J.

2) Local Sources of Magnetic Field Noise: Thermal Noise of the Cryostat

The G10 fiberglass cryostat used in these experiments was of the canonical “low-noise” variety; nonetheless, Nyquist currents in metallic parts in the insulation jacket of the cryostat gave rise to a considerable magnetic field noise of roughly $10 \text{ fT/Hz}^{1/2}$ referred to the sensing loop of the second-order gradiometer. To better understand the role of these metallic parts, with an eye to devising a means for reducing the magnetic field noise of the cryostat, it is useful to consider briefly some of the basic aspects of superinsulated cryostat design.

At a minimum, a cryostat consists of an inner vessel, which holds the liquid cryogen, and an outer vessel, which is maintained at room temperature; these are separated by a vacuum insulation jacket which eliminates heat transfer due to gaseous conduction (Figure 6.11). The dominant heat load on the inner vessel is then radiative.

Typically one minimizes radiative heat transfer by distributing multilayer insulation, or superinsulation, throughout the vacuum space of the cryostat. The superinsulation consists of many layers of mylar sheet onto which a thin film (a few tens of nanometers) of aluminum has been evaporated. To ensure that the superinsulation equilibrates at a sufficiently low temperature, the insulation jacket of the cryostat also contains a relatively massive thermal shield which is cooled to an intermediate temperature. This thermal shield might be cooled separately (for example, with a cryocooler); often it is thermally anchored to the neck of the inner vessel so that it is cooled by the gas which evaporates from the bath. For efficient cooling of the thermal shield it is desirable that it be made of a material which is a good thermal conductor: aluminum foil (maybe 5 mil thick) is often used for the thermal shield.

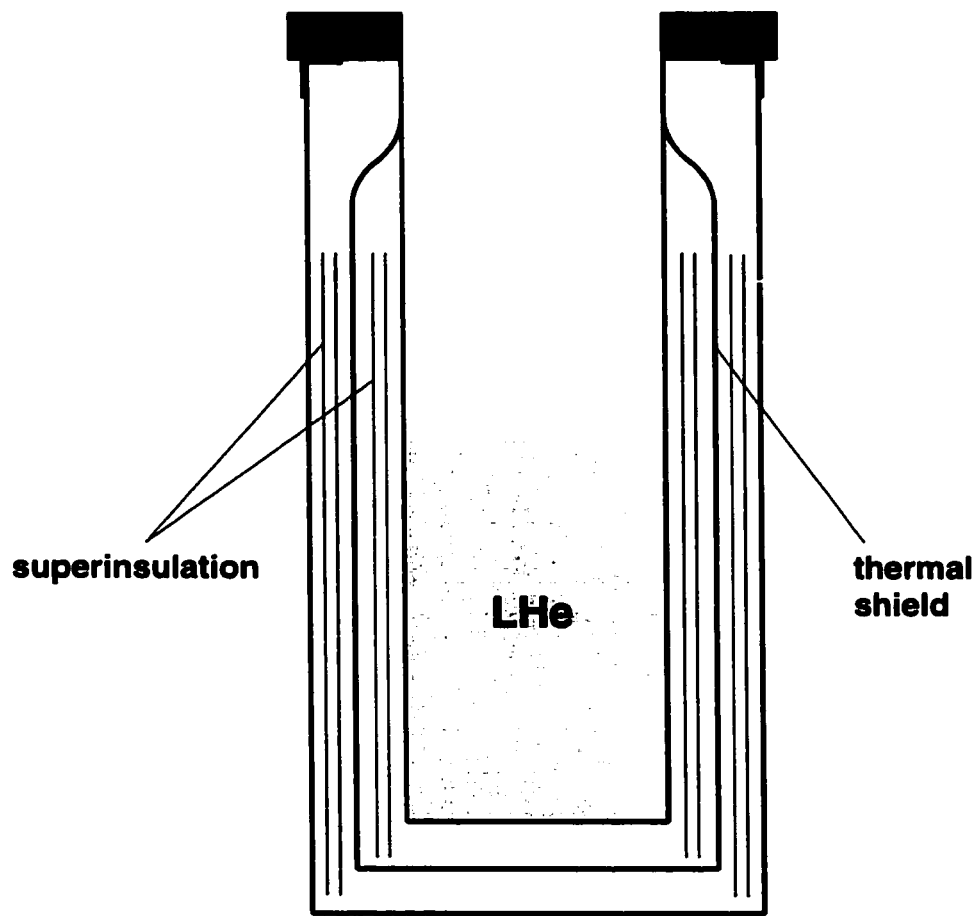


Figure 6.11. Generic superinsulated liquid helium cryostat. The insulation jacket is filled with numerous layers of aluminized mylar (superinsulation) which act as baffles to reduce the radiative heat load on the inner vessel. To ensure that the superinsulation equilibrates at a sufficiently low temperature, it is placed in thermal contact with a relatively heavy thermal shield which is cooled to a temperature of around 80 K by the evaporating helium gas. Even in a canonical “low-noise” cryostat, the normal metal of the superinsulation and the thermal shield can be significant sources of thermal magnetic field noise.

While the thermal shield and aluminized mylar greatly extend the hold time of a cryostat, they also act as local sources of thermal noise: in any closed normal conducting path, there will be Nyquist noise currents which generate magnetic field noise [16]. In a typical “low-noise” dewar, the thermal noise of the metal in the insulation jacket is minimized by restricting the size of continuous electrically conductive areas, so that noise

currents are unable to flow in large circuits. The magnetic field noise generated by the Nyquist currents therefore falls away rapidly with distance from the noise source. In the case of the multilayer insulation, the aluminized mylar might be heavily scored, that is, filled with a network of fine scratches which break up continuous conducting paths. In the case of the thermal shield, the heavy aluminum or copper foil is often replaced by “coil foil”, which consists of several layers of very thin gauge (gauge 38 or so) insulated copper wires laid side-by-side and epoxied together to form a continuous sheet. The coil foil conducts heat relatively efficiently; however, noise currents are restricted to paths which are no larger than the diameter of the individual wires.

Nevertheless, even a cryostat designed according to the low-noise principles outlined above will typically have a noise at the level of a few $\text{fT/Hz}^{1/2}$. In the case of the dewar used for the MRI experiments, the situation was even worse: the tail section of the cryostat was 200 mm long, roughly twice the baseline of the second-order gradiometer. Therefore, in addition to the sensing loop of the gradiometer, the reference loops were also tightly coupled to the metallic parts in the insulation jacket of the cryostat, leading to an increase in the noise contribution from the dewar by the factor $(1^2 + 2^2 + 1^2)^{1/2} \sim 2.4$, as noise flux coupled from local sources to the various loops of the gradiometer added incoherently.

In the hopes of reducing the cryostat noise contribution below the level of a few $\text{fT/Hz}^{1/2}$, we are currently constructing a home-made G10 fiberglass cryostat, based on the design of Seton *et al.* [17]. In this design, the normal metal thermal shield is replaced by a thermal shield which is entirely ceramic, or a composite of fiberglass and ceramic. Such a thermal shield has a relatively high thermal conductivity, but is electrically

insulating and therefore does not give rise to magnetic field noise. In addition, the aluminized mylar multilayer insulation is replaced by aluminized polyester fabric. In this case, the weave of the fabric breaks up continuous conducting paths, again preventing the flow of noise currents in large circuits. With this design, Seton *et al.* have achieved a magnetic field noise of $80 \text{ aT/Hz}^{1/2}$ [6], albeit at a relatively high frequency of 400 kHz.

J. Ongoing Work

During the weeks I have taken to write this thesis, work on the SQUID MRI system has continued intensively. We have recently obtained on loan from CTF Systems, Inc. a low-noise G10 fiberglass cryostat which can accommodate a gradiometer with pickup coil diameter up to 160 mm. We have constructed a second-order gradiometer with an overall baseline of 150 mm, and pickup loop diameter 65 mm. The 1 + 2 + 1 turn pickup coil has an inductance of roughly $1.7 \text{ } \mu\text{H}$, yielding a gradiometer sensing area $A_{\text{sense}} = 7.6 \text{ mm}^2$. In addition, in order to eliminate the contribution to the system noise from distant sources of noise and interference, we have recently constructed an eddy current shield which surrounds the SQUID MRI system. The shield consists of a single layer of 1/8" (roughly 3 mm) 5052 Al plate ($\rho = 4.8 \text{ } \mu\Omega \text{ cm}$); its dimensions are 8' x 8' x 12'. At a frequency of around 5 kHz, the shield is roughly two skin depths thick, corresponding to an attenuation of interfering fields in the relevant frequency range by an order of magnitude. Inside this eddy current shield and with the new, large-area gradiometer, we have measured the thermal noise from the CTF dewar to be around $2.5 \text{ fT/Hz}^{1/2}$ at a frequency of 5 kHz; at the moment, the system noise is dominated entirely by thermal noise from the dewar. The current noise level of $2.5 \text{ fT/Hz}^{1/2}$ is roughly a

factor of 6 lower than the noise level achieved in the measurements described above, corresponding to a potential reduction in MRI acquisition time by a factor of 36.

The larger pickup coil of the new gradiometer will allow acquisition of MRIs from larger samples, and we will soon attempt to perform some first *in vivo* imaging experiments. However, the larger area of the sensing loop entails a significant loss of sensitivity to dipole sources (and in MRI, one is concerned with dipole sources). The signal flux coupled to a pickup loop of radius r from a dipole goes as r^{-1} (this is seen easily if the problem is viewed in terms of mutual inductances). On the other hand, in the case of a system whose noise is dominated by the magnetic field environment, the noise flux coupled to the pickup loop will go as r^2 . Therefore, in more than doubling the diameter of the gradiometer sensing loop, we have decreased the sensitivity to magnetic dipoles by more than a factor of $2^3 = 8$, roughly canceling the advantage we have gained in reducing the magnetic field noise of the system. Due to these considerations, it will ultimately be desirable to replace the single large-area sensor with an array of smaller sensors, designed for maximum sensitivity to localized sources. This is in fact the current trend in high-field clinical MRI, where system noise is dominated by inductively coupled losses from the human body.

As a final remark, it should be noted that the low-field MRI techniques presented in this chapter could readily be adapted for use with existing commercial SQUID systems designed to measure weak magnetic signals generated by electrical currents in the human body. Here, the frequency-independent response of the untuned SQUID magnetometer would be exploited to detect biomagnetic signals at frequencies in the range of Hz to tens of Hz, as well as to perform MRI at proton Larmor frequencies on the order of kHz. It

would be particularly interesting to develop a SQUID system which could be used for both MRI and magnetoencephalography (MEG). In MEG, an array of low- T_c SQUID sensors (up to 300 channels in state-of-the-art systems) is used to measure weak neuromagnetic signals (of the order of tens of fT) in order to map out electrical activity in the brain; the technique is rapidly becoming more widespread in clinical use, especially for studies of epilepsy and for pre-surgical screening of brain tumors. The ability to perform MRI would greatly increase the utility of the SQUID system, creating a versatile, new tool for studies of the human brain.

References

1. Tseng C H, Wong G P, Pomeroy V R, Mair R W, Hinton D P, Hoffmann D, Stoner R E, Hersman F W, Cory D G, Walsworth R L (1998) Low-field MRI of laser polarized noble gas *Phys. Rev. Lett.* **81** 3785-3788
2. Stepišnik J, Eržen V, and Kos M (1990) NMR imaging in the Earth's magnetic field *Magn. Reson. Med.* **15** 386-391
3. Fischer H W, Rinck P A, Van Haverbeke Y and Muller R N (1990) Nuclear relaxation of human brain grey and white matter: analysis of field dependence and implications for MRI *Magn. Reson. Med.* **16** 317-334
4. Planinšič G, Stepišnik J, and Kos M (1994) Relaxation-time measurement and imaging in the Earth's magnetic field *J. Magn. Reson. Ser. A* **110** 170-174
5. do Nascimento G C, Engelsberg M, and de Souza R E (1992) Digital NMR imaging system for ultralow magnetic fields, *Meas. Sci. Technol.* **3** 370-374
6. Seton H C, Hutchison J M S, and Bussell D M (1997) A 4.2 K receiver coil and SQUID amplifier used to improve the SNR of low-field magnetic resonance images of the human arm *Meas. Sci. Technol.* **8** 198-207
7. Macovski A and Conolly S (1993) Novel approaches to low cost MRI *Magn. Reson. Med.* **30** 221-230

8. Shao W, Wang G, Fuzesy R, Hughes E W, Chronik B A, Scott G C, Conolly S M, and Macovski A (2002) Low readout field magnetic resonance imaging of hyperpolarized xenon and water in a single system *Appl. Phys. Lett.* **80** 2032-2034
9. Seeber D A, Ciobanu L, and Pennington C H (2002) Advances toward MR microscopy of single biological cells *Appl. Magn. Reson.* **22** 139-143
10. Bottomley P A (1981) A versatile magnetic-field gradient control-system for NMR imaging *J. Phys. E Sci. Instrum.* **14** 1081-1087
11. Horowitz P and Hill W (1989) *The Art of Electronics* Cambridge: Cambridge University
12. Mück M, Dechert J, Gail J, Kreutzbruck M, Schone S, Weidl R (1995) Response of radio frequency superconducting quantum interference devices to electromagnetic interference *Rev. Sci. Instrum.* **66** 4690-4693
13. Agrawal A, unpublished.
14. Jain A K (1989) *Fundamentals of Digital Image Processing* Englewood Cliffs: Prentice Hall
15. Vrba J (1996) SQUID gradiometers in real environments *SQUID Sensors: Fundamentals, Fabrication and Applications* 117-178 Dordrecht: Kluwer Academic
16. Clem J R (1987) Johnson noise from normal metal near a superconducting SQUID gradiometer circuit *IEEE T. Magn.* **23** 1093-1096
17. Seton H C, Bussell D M, and Hutchison J M S (1995) Liquified gas cryostat, UK patent application 9617175.6

Chapter 7. Conclusion

At the most basic level, the feasibility of a given NMR experiment is determined by the SNR which can be achieved in the NMR spectrometer. When one is faced with the problem of insufficient SNR, it is most natural to take steps to enhance the strength of the NMR signal, for example, by performing the experiment in a higher magnetic field. It is no accident that the tremendous advances in NMR spectroscopy and MRI which have taken place over the last decades have coincided with the development of superconducting magnets capable of generating homogeneous, stable fields in the range of tesla to tens of telsa.

In any experiment involving SQUID detection of the NMR signal, however, the approach is exactly the opposite. In this case, the signal strength is typically quite low, and one attempts to enhance SNR by reducing the noise of the system - seduced, perhaps, by the thought that the SQUID is an intrinsically low-noise detector. This approach is much more difficult, and requires a good understanding of all the potential sources of noise in a SQUID system. In the case of SQUID detection of NMR signals from room-temperature samples, it is almost inevitable that the magnetic field noise of the

environment will dominate. The central challenge is therefore to engineer the environment of the experiment for minimum magnetic field noise over the relevant frequency range.

At frequencies in the range of Hz to tens of Hz, typical for biomagnetic signals, it has proven exceedingly difficult to approach the $1 \text{ fT/Hz}^{1/2}$ level in practical SQUID systems. At another extreme, researchers have achieved magnetic field noise below $0.1 \text{ fT/Hz}^{1/2}$ at frequencies around 1 MHz with minimal shielding. In the range of frequencies from 1 kHz – 10 kHz, especially relevant for the MRI work discussed above, there has been little investigation of magnetic field noise. It will be interesting to see whether it is possible with practical SQUID systems to achieve sensitivity of the order of $1 \text{ fT/Hz}^{1/2}$ at these frequencies; the success or failure of our approach to low-field MRI will ultimately depend on this.

Considerations of SNR aside, the untuned SQUID magnetometer has characteristics which are not matched by any other detector, namely, extreme sensitivity at low frequencies, as well as the ability to detect broadband: it is these traits which must be emphasized in any sensible application of SQUIDs to NMR. At present, it appears that the interesting experiments to be done with SQUID NMR fall into two broad categories: (1) fundamental studies on the far fringes of magnetic resonance research, which exploit the unique properties of the SQUID as NMR detector; and (2) niche applications, combining SQUID detection of low-frequency biomagnetic fields and NMR spectroscopy or MRI. From this first category, of particular note are experiments to measure the Barnett effect in nuclear spins, and experiments to recover spectral information obscured by magnetic susceptibility broadening by rotating the (necessarily

weak) Zeeman field. From the second category, especially interesting is the prospect for a many-channel SQUID system designed for both MEG and MRI in microtesla magnetic fields. All of these projects are currently being pursued in Berkeley. But SQUIDs are extraordinarily versatile devices, and the field of NMR is extremely rich; this is why the experiments described above have been so enjoyable. It is entirely likely that there are other, even more interesting possibilities for SQUID NMR out there, waiting to be discovered.